1003688

NSWC/DL TECHNICAL LIBRARY
2000212095
B60
1003688

Naval Surface Warfare Center
Dahlgren Division

Technical Digest *1997 Issue*

REFERENCE COPY
TECHNICAL LIBRARY, CODE B60
DAHLGREN DIVISION
NAVAL SURFACE WARFARE CENTER
DO NOT REMOVE

NAVSWC-DD-MP-97-097

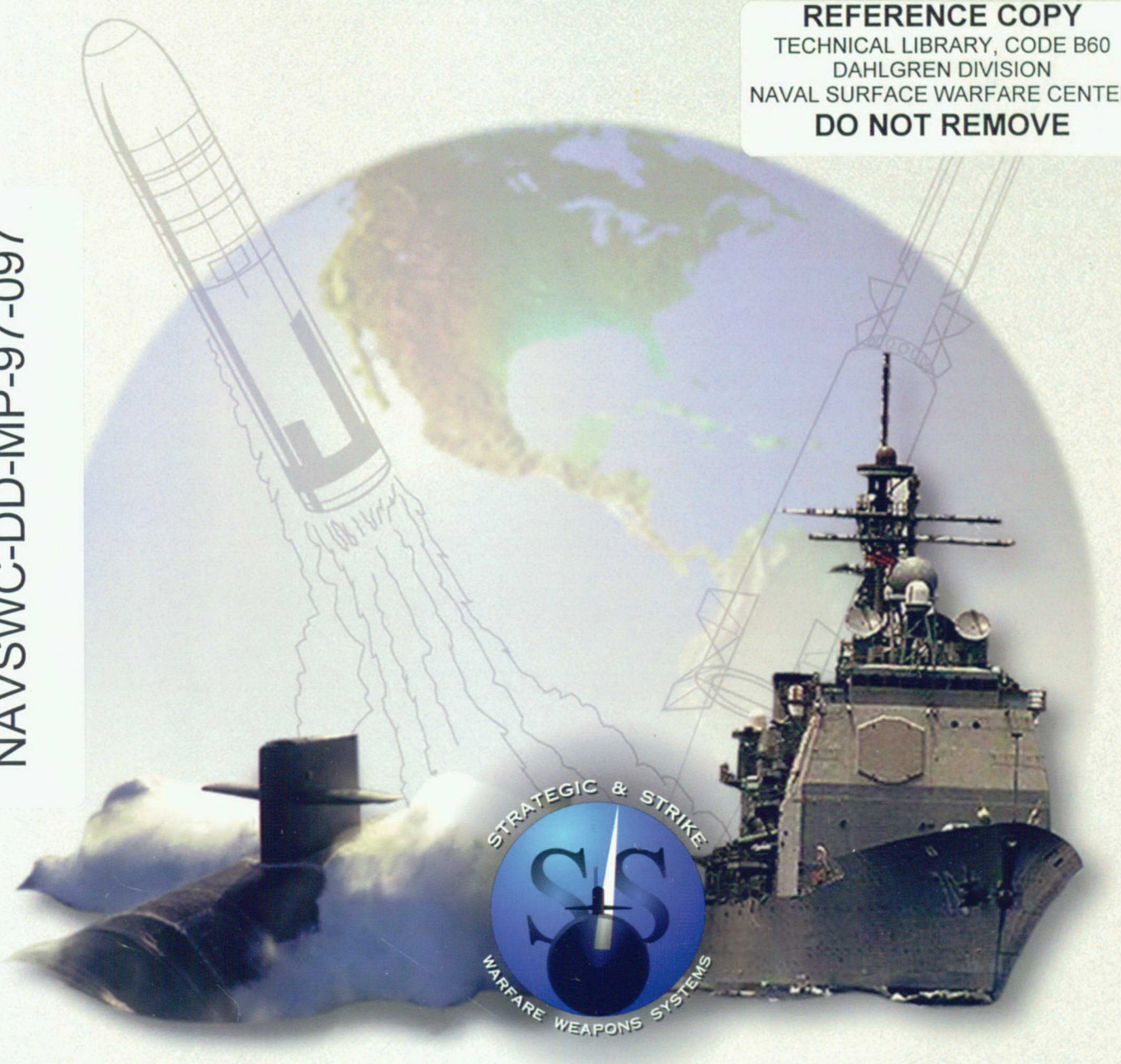

Strategic & Strike

WARFARE WEAPONS SYSTEMS

Report Documentation Page

Form Approved
OMB No. 0704-0188

Public reporting burden for the collection of information is estimated to average 1 hour per response, including the time for reviewing instructions, searching existing data sources, gathering and maintaining the data needed, and completing and reviewing the collection of information. Send comments regarding this burden estimate or any other aspect of this collection of information, including suggestions for reducing this burden, to Washington Headquarters Services, Directorate for Information Operations and Reports, 1215 Jefferson Davis Highway, Suite 1204, Arlington VA 22202-4302. Respondents should be aware that notwithstanding any other provision of law, no person shall be subject to a penalty for failing to comply with a collection of information if it does not display a currently valid OMB control number.

1. REPORT DATE **1997**	2. REPORT TYPE	3. DATES COVERED **00-00-1997 to 00-00-1997**
4. TITLE AND SUBTITLE **Technical Digest**		5a. CONTRACT NUMBER
		5b. GRANT NUMBER
		5c. PROGRAM ELEMENT NUMBER
6. AUTHOR(S)		5d. PROJECT NUMBER
		5e. TASK NUMBER
		5f. WORK UNIT NUMBER
7. PERFORMING ORGANIZATION NAME(S) AND ADDRESS(ES) **Naval Surface Warfare Center,Dahlgren Division,Dahlgren,VA,22448-5000**		8. PERFORMING ORGANIZATION REPORT NUMBER
9. SPONSORING/MONITORING AGENCY NAME(S) AND ADDRESS(ES)		10. SPONSOR/MONITOR'S ACRONYM(S)
		11. SPONSOR/MONITOR'S REPORT NUMBER(S)
12. DISTRIBUTION/AVAILABILITY STATEMENT **Approved for public release; distribution unlimited**		
13. SUPPLEMENTARY NOTES		
14. ABSTRACT		
15. SUBJECT TERMS		

16. SECURITY CLASSIFICATION OF:			17. LIMITATION OF ABSTRACT	18. NUMBER OF PAGES	19a. NAME OF RESPONSIBLE PERSON
a. REPORT **unclassified**	b. ABSTRACT **unclassified**	c. THIS PAGE **unclassified**	**Same as Report (SAR)**	**139**	

Standard Form 298 (Rev. 8-98)
Prescribed by ANSI Std Z39-18

Tomahawk

Editorial Board

Dr. Frankie G. Moore, Chairman
Mr. Kenneth C. Baile
Mr. David M. Bozicevich
Mr. Sidney H. Hankerson, Jr.
Mr. Raymond H. Hughey, Jr.
Mr. Michael J. Kuchinski
Mr. Edward C. Linsenmeyer
Mrs. M. Patrice Waits
Dr. Jon J. Yagla

Editorial Staff

Mrs. M. Patrice Waits, Managing Editor
Mr. David M. Bozicevich, Associate Editor
Mr. Clement Bryant, Graphic Designer

Trident

The *Naval Surface Warfare Center Dahlgren Division Technical Digest* presents unclassified articles, contributed primarily by Division scientists and engineers, on selected research and development programs. The Dahlgren Division, under the leadership of the Naval Surface Warfare Center, provides research, development, test and evaluation, engineering, and fleet support for surface warfare systems, surface ship combat systems, ordnance, mines, amphibious warfare systems, mine countermeasures, special warfare systems, Marine Corps weaponry systems, and strategic systems. Please address any correspondence concerning the *NSWCDD Technical Digest* to: Dahlgren Division, Naval Surface Warfare Center, Technical Digest (Code B60), 17320 Dahlgren Road, Dahlgren, VA 22448-5100. Telephone (540) 653-3200 (DSN 249-3200).

About the cover: The topic of this issue—strategic and strike warfare weapons systems—is represented on the cover by several missiles and vessels. To the left of the logo, the *Ohio*-class fleet ballistic missile submarine USS *Maine* (SSBN 741) and the Trident II D5 submarine launched ballistic missile (SLBM) schematic above it exemplify strategic warfare. To the right of the logo, the *Ticonderoga*-class Aegis guided-missile cruiser USS *Lake Erie* (CG 70) and the Standard SM-2 Block IV surface-to-air tactical missile schematic above it serve respectively as examples of a strike warfare platform and weapon.

Poseidon

NSWCDD/MP-97/97
Approved for public release;
distribution is unlimited.

Strategic
WARFARE WEAPONS SYSTEMS

Naval Surface Warfare Center
Dahlgren Division

Technical Digest

1997 Issue

Guest Editors' Introduction	R. V. Gates A. M. Morrison	3
The Reentry Systems Application Program (RSAP)	A. M. Morrison J. S. Vamos	8
Wind Tunnel Testing of Strategic Systems in NSWCDD's Tunnel #9	J. A. Hill J. F. Lafferty D. E. Marren	24
Evaluation of Reentry Systems Nosetips and Heatshields Using an Arc Heater Facility	M. J. Gillum L. P. O'Hare	36
Moving Mass Roll Control for Fixed-Trim Reentry Bodies	F. J. Regan	44
FREE—Algorithm for Solution of an SLBM Multiple Constraint Mission Problem	S. M. Davis D. L. Owen	58
Fuzzy-Logic-Based Expert System Solutions to Sequencing and Grouping Problems	P. L. Godin	66
High-Altitude Electromagnetic Pulse (HEMP)	E. R. Brown B. L. Bressler	76
Developing Software for a Distributed, Synchronous, Real-Time System	E. A. Cooper, Jr. A. L. Philpott, Jr.	90

Point Mass, Dipole, and Quadrupole Gravity Modeling for FBM Systems Support	A. E. Rufty	100
Computation of Ballistic Parameters for SLBM	K. A. Wright	110
Advanced Technology Demonstration of the Naval Tactical Missile System (NATACMS)	R. A. Frazer J. E. Bibel	120

Guest Editors' Introduction

Mr. Robert V. Gates and Dr. Alfred M. Morrison

The traditional strategic mission continues despite the end of the Cold War. The current situation relative to the DoD budget and the uncertainty that surrounds future requirements for strategic systems have created a climate replete with possibilities. This issue of the Naval Surface Warfare Center, Dahlgren Division (NSWCDD) Technical Digest focuses on strategic and strike systems and some of the technical contributions made by NSWCDD.

For the last 40 years, the term "strategic" has signified nuclear weapons carried on the platforms that comprise the triad: submarines, groundbased missiles, and bombers. Within the Navy, strategic has meant nuclear weapons on Submarine Launched Ballistic Missiles (SLBMs). National policy and weapon system development during the Cold War were motivated largely by the threat posed by the USSR. There was nearly continual development of new systems, especially land- and submarine-based missiles. They increased in range and accuracy and in the number and types of nuclear warheads they carried in order to meet the threat and to satisfy national policy needs. A by-product was the development and maintenance of a standing government-industry team that provided for the necessary research, development, production, and life-cycle support for each of these systems.

Targeting policies also changed as weapons systems became more sophisticated and as national interests evolved. U.S. nuclear policy moved from "massive retaliation" in the 1950s to the current policy of "flexible response" as weapons and their communications and control systems improved in capability. The signing of the Strategic Arms Limitation Treaty (SALT) in the early 1970s ushered in an era where arms control became a key element of national policy. The Strategic Arms Reduction Treaties (START I and II) have continued this process. These treaties and, especially, the end of the Cold War have led to some fundamental changes in the planning and infrastructure associated with strategic systems. Specifically, the number and variety of nuclear weapons allowed by the signatories of these treaties are decreasing (and may decrease beyond present treaty limits), and no new strategic weapons systems are currently under development. Targeting requirements also changed as enemy capabilities grew and diversified. The combination of a flexible response policy and a more sophisticated threat led to a need for a more responsive planning process.

STRATEGIC MISSION—A MISSION DIRECTED AGAINST ONE OR MORE OF A SELECTED SERIES OF ENEMY TARGETS WITH THE PURPOSES OF PROGRESSIVE DESTRUCTION AND DISINTEGRATION OF THE ENEMY'S WAR-MAKING CAPACITY AND HIS WILL TO MAKE WAR. TARGETS INCLUDE KEY MANUFACTURING SYSTEMS, SOURCES OF RAW MATERIAL, CRITICAL MATERIAL, STOCKPILES, POWER SYSTEMS, TRANSPORTATION SYSTEMS, COMMUNICATIONS FACILITIES AND OTHER SUCH TARGET SYSTEMS. AS OPPOSED TO TACTICAL OPERATIONS, STRATEGIC OPERATIONS ARE DESIGNED TO HAVE A LONG-RANGE, RATHER THAN IMMEDIATE, EFFECT ON THE ENEMY AND ITS MILITARY FORCES.

JCS PUB 1-02

The impetus for maintaining the government and industrial teams has been provided by the continual development of systems. Trained workforces and specialized facilities cannot be maintained without a development program. Production of existing systems traditionally underwrites the development of the next by maintaining an industrial and governmental base. While no one can know what the future holds, viable strategic systems (and, especially, submarine-based systems) will be needed well into the next century. When a new strategic weapon system is needed in the future, development may be forced to proceed without an existing industrial base. In the absence of such a development, the life of existing strategic systems must be extended via the application of new technology. A key consideration in the planning for strategic systems, therefore, is the preservation of the key industrial and governmental base. Of particular interest in this regard are reentry system technology, rocket motors, and high-performance inertial guidance systems.

The definition of the strategic mission given in Joint Chiefs of Staff (JCS) Publication 1-02 (see shaded text) is more expansive and is concerned primarily with the intended targets and the level of control required. Other studies have begun to consider the strategic problem without limiting the solution to nuclear weapons. Another way to describe *strategic* is in the larger context of strike warfare. Strike warfare is the destruction or neutralization of enemy targets ashore using conventional or nuclear weapons. In other words, it is more accurate to think of strike warfare as a continuum, with the strategic mission as one extreme. This is shown in Figure 1. This view of strike encompasses the use of ballistic missiles of all ranges with conventional payloads against strategic targets, as well as short-range missiles for power projection or in a fire-support role in a littoral environment. Since it is not weapons-systems based, it also includes aircraft and cruise missiles.

This new definition of the strategic mission still assumes that deterrence is primary. It assumes, however, that the weapons required to deter may vary with circumstances. For example, a very capable nuclear triad is appropriate when dealing with a similarly capable adversary. On the other hand, SLBMs with conventional warheads may be used to augment the nuclear force or to supplant it when faced with a different adversary or situation. Taken further, smaller short-range missiles (on either submarine or surface platforms) may be appropriate in a theater-level conflict or in a littoral situation. They may deter or can be used to support landbased operations in the theater.

Studies that attempt to define strategic systems requirements assume a range of possible futures. They vary from a resurgent Russia with a large nuclear capability, to a much smaller treaty-limited nuclear force and multiple countries who possess nuclear weapons, to a world with no nuclear power comparable to the U.S. The variety of weapons previously described are characteristic of those needed in each of these situations. Perhaps the biggest challenge will be to sustain an appropriate strategic capability in the future within a constrained DoD budget. Maintaining a capable government-industry team will be critical to meeting this challenge.

In short, four thrusts associated with future strategic systems have been identified: maintenance of the industrial base, improved planning systems, modernization and life extension of existing systems, and the expansion of the strategic mission. There are ongoing efforts associated with each thrust. The Reentry Systems Application Program (RSAP), for example, addresses maintenance of an industrial and governmental base in reentry systems through the development of technology to extend the life of current reentry systems and components. One area receiving attention is the replacement of heatshield materials. The SLBM Retargeting System (SRS) program is addressing the improvement of the strategic retargeting processes from landbased planning and processing to shipboard implementation. This program, which began in 1989, has included both hardware and software upgrades and was one of the driving forces behind the SLBM Fire Control (FC) Life-Cycle Cost Control (LCCC) program. The FC LCCC program, besides adding capability needed to improve onboard retargeting processes, will yield a shipboard FC system that is supportable (and upgradable) well into the future. It will replace a computer-centered architecture (with a 1970s era computer and other specialized elements) with a distributed computer architecture utilizing nondevelopmental items (NDI) and commercial off-the-shelf (COTS) components (hardware and software) to the greatest extent possible. There have also been studies (leveraging the Advanced Technology Demonstration/Advanced Concept Technology Demonstration (ATD/ACTD) and Independent Research and Development (IR&D) programs) that address technology issues associated with the development and fielding of conventional SLBMs and the incorporation of existing small missiles, such as the Army Tactical Missile System (ATACMS).

NSWCDD has a long history in the SLBM program. It has been the primary developer of FC and targeting software for all SLBM systems from POLARIS (A1) to TRIDENT (D5).[1] It has

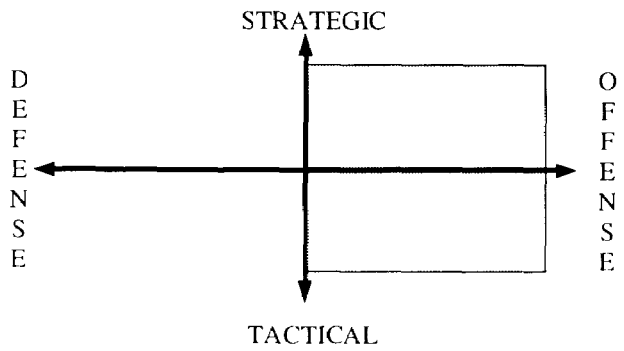

Figure 1—The Strike Continuum

an equally long history in developing and testing reentry systems. It has roles in the TOMAHAWK cruise missile, in surface ship-based missiles, and in Naval Surface Fire Support (NSFS) programs. These are described in previous issues of the *NSWCDD Technical Digest.*

The articles in this issue describe some of the NSWCDD efforts supporting the four thrusts outlined above. Morrison and Vamos describe the RSAP as well as the conditions that gave rise to it. Hill, Lafferty, and Marren address the wind tunnel facilities at NSWCDD, from its origins after World War II to its upgrades and use in testing many reentry and space systems. Gillum and O'Hare continue the discussion with a description of the analysis and testing of reentry body nosetip and heatshield materials. Regan considers a specific technical issue associated with a maneuverable reentry body. In particular, he develops a moving mass control system for such a vehicle and analyzes vehicle design and autopilot issues.

There are several articles that describe new technical solutions to standard targeting problems. Davis and Owen present a computer algorithm that can be used to solve the multiple constraint targeting problem characteristic of shipboard mission planning for SLBM. Godin describes a new approach to solving the traditional sequencing and grouping problems associated with the targeting of multiple, independently targeted reentry vehicle (MIRV) systems, such as TRIDENT. He proposes the application of a fuzzy-logic-based expert system to this problem. Nuclear warhead detonations can be used to produce a high-altitude electromagnetic pulse (HEMP). Brown and Bressler describe the military utility of this phenomenon and the fundamental physics that support a first-principles computer code developed by NSWCDD.

FC modernization can take several forms. Cooper and Philpott address some of the implications of developing software for an NDI/COTS-based distributed, synchronous, real-time FC system. They describe the current system and its associated constraints, and the implementation of NDI/COTS elements in a way that satisfies these constraints. FC modernization may also address the upgrading of computations to either incorporate new mathematical techniques or better utilize the capability provided by a new shipboard computer architecture. Two specific examples are included. Rufty presents the development of an accurate and computationally efficient gravity model based on point masses, point dipoles, and point quadrupoles. He develops the model and describes its applicability to both SLBM and other applications. Wright describes the current modeling of reentry weather data in SLBM FC computations and possible improvements to it.

As noted previously, NSWCDD has supported a variety of efforts related to the development and testing of small short-range missiles that have applicability to possible future strategic missions. One such system is a Navy version of the ATACMS (sometimes called NATACMS). NSWCDD supported N8 in an ATD program to demonstrate the effectiveness of the ATACMS in a shipboard environment. Frazer and Bibel describe the modifications required to the Army missile and launcher, the flight test program (including a launch from USS *Mount Vernon*), and postflight results.

REFERENCES

1. Gates, Robert V., "Strategic Systems Fire Control," *Naval Surface Warfare Center, Dahlgren Division Technical Digest,* 1995 Issue.

THE GUEST EDITORS

MR. ROBERT V. GATES

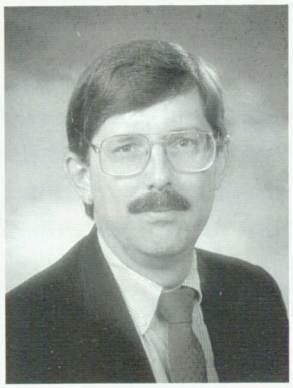

MR. ROBERT V. GATES has a B.S. in physics from the Virginia Military Institute, an M.Eng. in engineering science from the Pennsylvania State University, an M.A. in political science from the Virginia Polytechnic Institute and State University, and graduated with distinction from the Naval War College. He is currently Director of Strategic Planning for NSWCDD. His previous assignment was as a Principal Physicist in the Strategic and Space Systems Department of NSWCDD where he developed concepts for future Navy strategic systems, performed targeting analysis for the CNO staff, and led the Strategic and Strike Warfare Focus Team at NSWCDD. Employed at NSWCDD since 1970, he has provided technical support in the areas of stellar inertial guidance, accuracy modeling, and flight test support for the development of FC and targeting support for TRIDENT I, TRIDENT II, and the United Kingdom POLARIS SLBM programs. He has also held a variety of management positions within the SLBM Research and Analysis Division at NSWCDD. He is a member of Pi Alpha Alpha, the national Public Administration Honor Society. Among his awards is the Navy Meritorious Civilian Service Award.

DR. ALFRED M. MORRISON

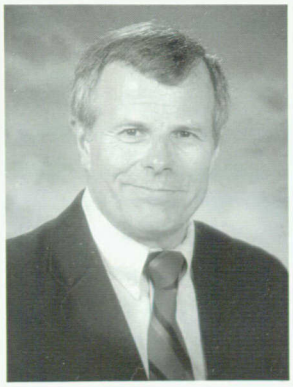

DR. ALFRED M. MORRISON is an SES/Senior Level engineer currently assigned to the Strategic and Strike Systems Department as Chief Scientist for Submarine Launched Ballistic Missiles and Reentry Systems. He has been involved in Strategic Missile: technology development, ground and flight testing, and reentry systems engineering. He was responsible for the technical direction of the NSWCDD reentry programs supporting Trident I, the Trident Improved Accuracy Program, and Trident II. He is currently involved in the development of programs aimed at extending the life of deployed SLBM systems. He holds a B.S., M.S., and Ph.D. in aerospace and mechanical engineering from the University of Notre Dame. He is a member of the Naval Submarine League and the Society of Sigma Xi, and is an Associate Fellow of the American Institute of Aeronautics and Astronautics.

The Reentry Systems Application Program (RSAP)

Dr. Alfred M. Morrison and Dr. John S. Vamos

In this age of reductions in strategic nuclear forces and decreasing defense budgets, economics has forced the refurbishing of currently deployed systems and the extension of their operational life expectancies, rather than the building of new systems. The issue of greatly extending the useful age of components and material systems beyond their design lives, from approximately 20 years to as many as 60 years, is a problem that the reentry system industrial base has not faced in the past. Congress has funded the Reentry Systems Application Program (RSAP) with the objectives of providing the technology to maintain the currently deployed reentry systems beyond their original design lives. Topics covered in this article include: a brief history of the genesis of the program, an overview of the objective and approach to conducting the program, a discussion of a recently conducted reentry industrial base survey, and the results of a ground test program evaluating potential replacement candidate heatshield materials. The reentry system industrial base is found to be undergoing significant erosion. The reentry system heatshield is identified as a component that the industrial base no longer supports and which has the potential for age-related performance degradation. Arc heater tests and high-temperature thermomechanical properties characterization experiments show the potential for the development of a replacement heatshield material.

Background

In his National Security Policy Statement (July 1994), the President outlined rationale for the maintenance of nuclear forces with the following policy statements:

"Even with the Cold War over, our nation must maintain military forces that are sufficient to deter diverse threats...We will retain strategic nuclear forces sufficient to deter any future hostile foreign leadership with access to strategic nuclear forces from acting against our vital interest and to convince it that seeking a nuclear advantage would be futile. Therefore we will continue to maintain nuclear forces of sufficient size and capability to hold at risk a broad range of assets valued by such political and military leaders. A critical priority for the United States is to stem the proliferation of nuclear weapons and other weapons of mass destruction and their missile delivery systems."

In response to this policy, the Department of Defense (DoD) undertook, for the first time in 15 years, a comprehensive review of U.S. nuclear forces by establishing the Nuclear Posture Review (NPR).

Nuclear Posture Review

The DoD faced a series of new environments as the NPR was initiated. The security environment had undergone rapid and dramatic change. There was a reduction in the conventional threat in Europe. The threat posed by Russia was also reduced and was significantly changed, as driven by continuing political and economic reform in the Former Soviet Union (FSU). Regional threats had become more important than ever before. The economic environment was paced by budget constraints that were more severe than at any time during the existence of U.S. Strategic Forces. Substantial reductions in U.S. Strategic Forces were planned and underway. For the first time since the deployment of U.S. Strategic Forces, there was no active or planned program for the development of strategic weapons. These new environments created a need for stock-taking; for rebalancing the Strategic Forces infrastructure, industrial base, and technology base; and for developing a plan to retain quality people.

Results of NPR

The NPR set out military requirements for U.S. Strategic Forces based on projections through the year 2003. Full implementation of Strategic Arms Reduction Treaties (START I and START II) was assumed. Capabilities of the FSU remained the primary concern. Russia (or anyone else) was not to be targeted today, but U.S. Strategic Forces were directed to be prepared for the possible emergence of hostile governments in Russia or for the failure of the arms control process in the FSU. Preparedness was to take the form of a "warhead upload hedge," which would preserve options for uploading or reconstituting U.S. Strategic Forces in response to changes for the worse in political relations with Russia or to the failure to fully implement START I or START II. Options for making faster, deeper force reductions were also to be kept open in the event that new strategic arms reductions agreements could be negotiated.

Figure 1 illustrates the warhead upload hedge. The top curve of Figure 1 depicts the reductions toward START I limits accomplished by the FSU before economics brought them to a halt. The bottom curve shows the corresponding U.S. reductions, which met START I levels in 1994 and are on a path to meet START II levels by 2003. Up and down ramps below the "START I Accountable Warhead Limit" line illustrate potential upload/reconstitution hedges, as well as potential faster/deeper reductions. Infrastructure requirements identified by the NPR as necessary to support the upgrade/reconstitution hedge included replacement of the guidance systems and remotoring of the propulsion systems on Minuteman III, continued production of the Trident II D-5 missile body beyond 1995 to maintain the missile industrial base, funding of the sustainment of strategic missile guidance systems, and maintenance of the reentry system industrial base.

SAG Industrial Base Study

In parallel with the NPR, the U.S. Strategic Command (USSTRATCOM) Strategic Advisory Group (SAG) studied the Submarine Launched Ballistic Missile (SLBM) and Intercontinental Ballistic Missile (ICBM) industrial bases. The purposes of the SAG study were to identify those management assurances necessary for USSTRATCOM to retain confidence in the dependability of SLBMs and ICBMs for the next period of years, to determine subsystem areas where special actions would be needed to assure performance, and to define those measures necessary to assure special action subsystems. For the purpose of the study, the SLBM and ICBM industrial bases were defined as the

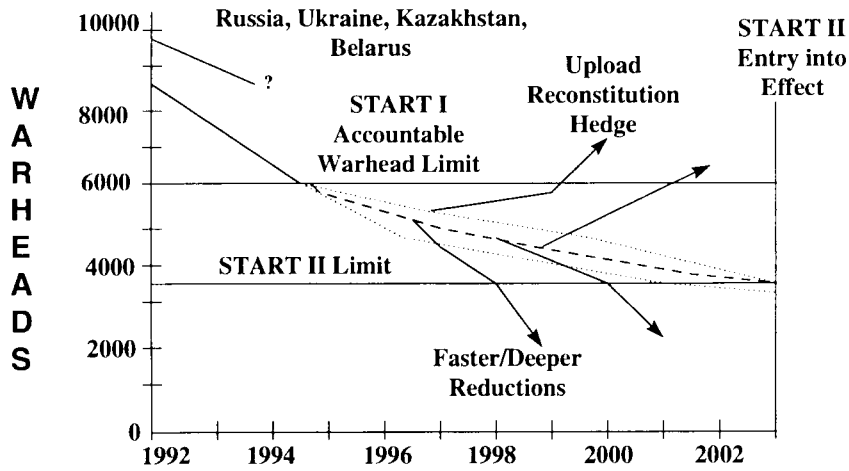

Figure 1—Force Structure Paths

combination of U.S. Government System Program Offices (SPOs), dedicated industrial companies (primes, subs, and associate contractors), and the system depots and service/national laboratories necessary to perform all of the acquisition and support functions, from research and development (R&D) to operations and maintenance (O&M) modification, for a fielded SLBM or ICBM weapon system. Key industrial base assumptions for the study were:

1. No new weapon system acquisitions would be conducted for an extended period of years.
2. No, or very few, new weapon system performance requirements would be issued for an extended period of years.
3. Severe limits would exist on money and people resources (government and industry) supporting SLBMs and ICBMs.
4. Company CEOs would make SLBM and ICBM industrial base decisions, with or without DoD input.

The study found that the ballistic missile life cycle had been broken. Since the initial deployment of U.S. SLBMs and ICBMs over 40 years ago, there had always been a ballistic missile acquisition industrial base in place to aid in O&M problem solution. Historically, when a ballistic missile weapon system reached operational phase, and modifications were required, a new system configuration was started. Based on the NPR plan, for the first time in 40 years, no new SLBM or ICBM systems were planned. In response, prime and subsystem contractors were rapidly downsizing, and suppliers were getting out of the ballistic missile business.

The reentry system industrial base was also assessed. Adequate reentry bodies for NPR requirements existed and had been delivered to the government. Reentry system production was over, and no new requirements were being worked. As a result, key people were being reassigned or were retiring, and the technical capability to fix unforeseen problems was found to be rapidly eroding. The study found that, without an adequate reentry system industrial base technology program, no materials or expertise would be available to maintain the existing fleet. The study also found that reentry systems must have a meaningful project to sustain an adequate engineering base, and low production rates were not found to be a solution.

The SAG Industrial Base Study made a series of recommendations, including the establishment of a reentry system advanced technology demonstration program. Such a program was required to enable solutions to unknown problems, which would develop with the life extension of the ballistic missile fleet. The creation of a reentry system advanced technology demonstration program was also seen to offer the possibility of reentry system technology insertion when needed and to assure the availability of critical test facilities such as the Arnold Engineering Development Center (AEDC) Plasma Jet Arc Heater.

REENTRY SYSTEMS APPLICATION PROGRAM (RSAP)

The reentry system industrial base recommendations from the NPR and from the SAG Industrial Base Study were addressed when the DoD proposed and Congress funded the RSAP (Navy) and the Reentry Vehicle Applications Program (RVAP, Air Force). RSAP and RVAP are cooperative programs whose objectives are to provide the technology necessary to maintain U.S. reentry systems beyond their original design lives, to maintain the minimum essential capability necessary to address reentry system aging phenomena, and to maintain the minimum essential technologies necessary to address future requirements of in-service SLBM and ICBM reentry systems. RSAP and RVAP are planned and conducted to take advantage of economic and technical synergies between the programs. The RSAP/RVAP coordination process is schematically depicted in Figure 2. Coordination is also regularly conducted among RSAP/RVAP, the Research and Technology Development (6.1/6.2) community, and the Small Business Independent Research Program in order to eliminate duplication of effort and to leverage DoD technology investments. The unique set of weapon requirements applicable to reentry systems are the most severe of all the strategic weapon subsystems requirements. These requirements,

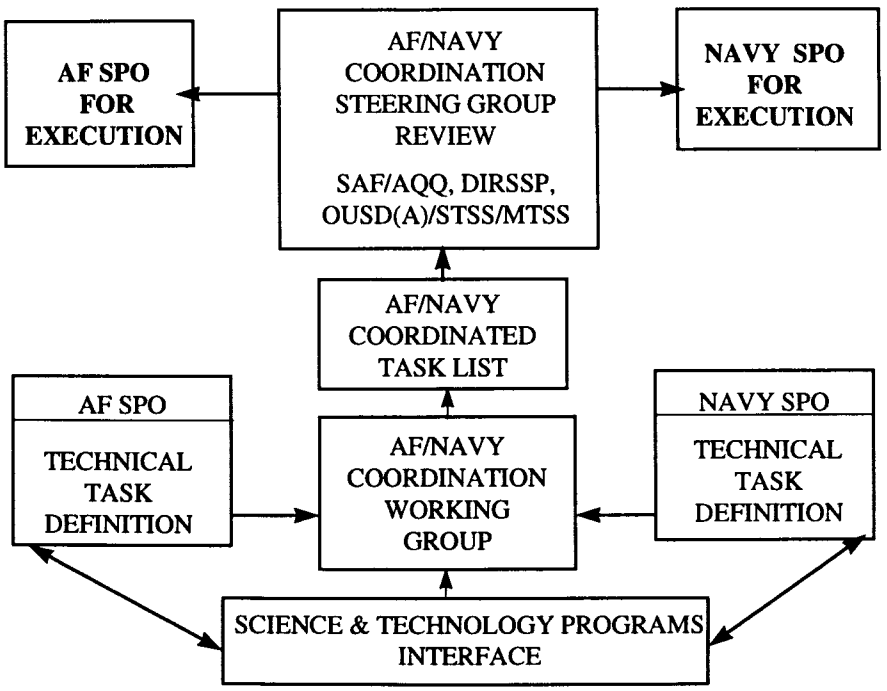

Figure 2—RSAP/RVAP Coordination

MISSION: HOLD STRATEGIC TARGETS AT RISK VIA SAFE, RELIABLE, AND ACCURATE WARHEAD DELIVERY AND DETONATION AT INTERCONTINENTAL RANGES WITHIN 30 MINUTES AND AFTER 15 YEARS DORMANCY

REQUIREMENTS:

- HIGH LEAKAGE AGAINST TERMINAL DEFENSE
- HIGH-KILL PROBABILITY, ACCURACY, AND RELIABILITY
- SEVERE WEIGHT AND MASS PROPERTY CONTROL
- DORMANT FOR 15 YEARS (DESIGN), 23 YEARS TO DATE ON MK 12
- OPERATIONAL READINESS IN LESS THAN 30 SECONDS
- NUCLEAR SAFETY: INADVERTENT DETONATION PROBABILITY $< 1.0 \times 10^{-9}$

ENVIRONMENTS:

- ASCENT HEATING AND DUST/DEBRIS EROSION
- NUCLEAR ENCOUNTERS (HUNDREDS OF ENCOUNTERS)
- ENDO- AND EXO-ATMOSPHERIC MECHANICAL AND ELECTRICAL EFFECTS 10 TO 20 TIMES HIGHER THAN BOOSTER LEVELS
- SHOCK LOADS BOOST, DEPLOYMENT AND REENTRY UP TO 200 G'S IN REENTRY 34 G (RMS) INTERNAL COMPONENT VIBRATION
- REENTRY THERMAL LOADS 185 ATMOSPHERES PRESSURE
- TEMPERATURES WOULD MELT UNPROTECTED ALUMINUM IN LESS THAN 1 MSEC

Figure 3—Unique Reentry Requirements

as given in Figure 3, mandate the focusing of supporting technologies to the extent that leveraging of other weapons technology for reentry applications is not possible. This also explains the need for a stand-alone reentry systems advanced technology demonstration program as called for by both the SAG Industrial Base Study and the NPR.

RSAP was implemented in FY 95. Three programmatic tasks were to be completed and reported to congressional staff before the initiation of technical program activity. These tasks included a Reentry System Industrial Base Assessment, to provide a detailed report on the erosion of the reentry system industrial base; a Reentry System Technology State-of-the-Art Assessment, to identify any emerging technologies that would support the life extension of reentry systems; and a Technical Program Plan, to provide details of the technical tasks that would be accomplished under RSAP.

Reentry System Industrial Base Assessment

The objective of the Reentry System Industrial Base Assessment was to evaluate existing and far-term capabilities of the reentry industrial base to support reentry system design, development, manufacturing, and in-service operations. The approach to conducting the assessment included identifying all prime contractors, suppliers, test facilities, etc., that make up the reentry system industrial base; ranking the criticality of the particular expertise that was so identified; and defining critical areas in which technical tasks must be performed to prevent further erosion of critical elements of the reentry system industrial base. The identification of the critical elements of the reentry system industrial base was accomplished by constructing detailed "technical task trees" for the design, development, manufacture, and in-service support of each reentry system component. Output from the Reentry System Industrial Base Assessment included lists of

reentry system industrial base critical capabilities, critical reentry system industrial base capabilities that are at risk or no longer exist, and recommended reentry system capabilities requiring sustainment.

The status of the critical reentry system capabilities, as determined by the Reentry System Industrial Base Assessment, was much the same as that projected by the SAG Industrial Base Survey. Figure 4 presents an example of the diminishing reentry system industrial base capability. The number of reentry system industrial base employees, as a percentage, is presented for years from 1990 to 1996. The percentage is established relative to the number of employees in the reentry industrial base in 1990 when the Trident II Mark 5 Reentry System was operationally deployed. The trend represented in Figure 4 shows a steady decline to six percent in 1996. This trend was also found to exist for reentry ground test experimental facilities.

One of the reentry system capabilities that was identified as critical and requiring sustainment was the ability to manufacture the after-body heatshield subsystem. Major elements of the development and manufacturing "task trees" for the heatshield material had disappeared, and other ballistic missile system components made of the same material had begun to show age-related material demise. As a result, an RSAP task was initiated to develop the technology necessary for the design and manufacture of a "replacement" heatshield system.

HEATSHIELD DEVELOPMENT

Current Navy reentry body heatshields are made of a rayon-fiber-based carbon phenolic material. The rayon fiber used in the Navy heatshields was produced by AVTEX Corporation. This fiber has not been manufactured since 1986 as a result of the closure of the manufacturing facility and demise of the company.

The goals of the Navy RSAP Heatshield Task are twofold. The first goal is to demonstrate the capability of material vendors to manufacture acceptable heatshield material, to existing heatshield specifications, utilizing the remaining stocks of AVTEX rayon fiber. The second goal, in light of the fact that AVTEX rayon fiber is no longer produced, is to identify alternate-fiber-based carbon phenolic materials that could replace the current AVTEX rayon-fiber-based system.

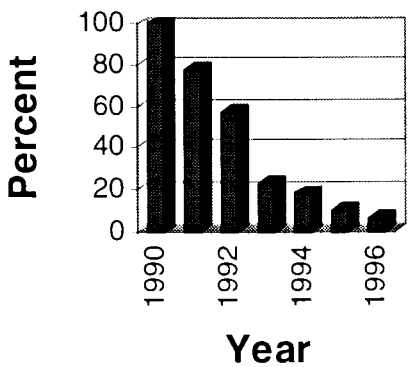

Figure 4—Example of Diminishing Reentry System Industrial Base Reentry System Employees

Alternate rayon fiber development is being pursued by the Air Force under the RVAP Program. Navy/Air Force development activities are coordinated through the RVAP/RSAP AF/Navy Coordination Working Group.

The Navy RSAP Heatshield Task is taking the following approach:

1. Transition replacement fibers from technology development programs and contractor IRAD programs to advanced development.
2. Manufacture replacement heatshield materials.
3. Evaluate materials in ground-test and flight-test environments.

Within the Navy, the RSAP Heatshield Task is a coordinated effort between the Strategic Systems Programs and the Navy 6.2 Strategic and Spacecraft Weapons Materials Program, directed by the Naval Surface Warfare Center, Dahlgren Division (NSWCDD). During FY 95 and 96, potential candidate non-rayon-fiber-based replacement heatshield materials were developed and subsequently evaluated to determine their performance.

The performance of the heatshield materials was assessed by plasma arcjet ablation ground tests and thermomechanical material characterization measurements. Performance was judged relative to the performance of AVTEX rayon-fiber-based heatshield materials.

Carbon Phenolic Material Test Specimens

Carbon phenolic composite materials are characterized by the type of fiber and type of resin infiltration process used in their manufacture. All material samples investigated to date were tape-wrapped carbon phenolic composites based on three different precursor fiber types. AVTEX rayon-fiber-based (Navy reference heatshield fiber), pitch-fiber-based, and polyacrylonitrile (PAN)-fiber-based materials were tested. There were two AVTEX rayon-fiber-based materials. The Navy reference material was constructed with the resin impregnation process, while the material designated HM Reference was constructed using an alternate resin impregnation process identified as the hot-melt process. The high-strength, high-modulus T350 PAN-fiber-based materials, designated 23-XAB and 25-XAB, and the pitch-fiber-based materials, designated A and A-100, were all constructed using the hot-melt process.

Carbon phenolic materials received from the manufacturer were subjected to a variety of tests to characterize them, in a nondestructive manner, and to determine their thermomechanical properties. The Southern Research Institute (SoRI), Birmingham, Alabama, performed all of the material characterizations. Nondestructive tests included visual inspection; a check for delaminations using edge X-rays; and measurements of density, porosity, and ultrasonic velocity. These measurements aided in the preparation of test specimens for ablation screening tests and for thermomechanical characterization tests.

HEATSHIELD PLASMA ARCJET ABLATION SCREENING TESTS

Test Facility

The AEDC High Enthalpy Ablation Test Unit (HEAT) H1 Facility at Tullahoma, Tennessee, is a continuous-flow, electric-arc-heated facility. Air is used as the working fluid. An axisymmetric expansion nozzle provides a supersonic free jet that discharges into the atmospheric environment of the test building. A schematic of the facility and supporting elements is shown in Figure 5.

A rotary model injection system with eight model mounting positions is used. This system can be programmed to inject test models at various axial stations, advance or retract axially,

and expose the models to the flow for various intervals of time. A maximum of seven models can be tested in a single run, as one position is left vacant for heater start-up and shutdown. Diagnostic probes, such as a pitot pressure probe or a calorimeter, may be used to characterize the flowfield; however, there is a one-to-one substitution between probes and models for each probe used in a run. Additional details of this facility may be found in Reference 1.

Test Instrumentation

Instrumentation used in the testing of heatshield material specimens permitted standard HEAT facility measurements of quantities such as pressure, temperature, water flow rate, current, and voltage. Wedge and null point calorimeter probes were swept through the flow to measure heat flux profiles. Heat flux profiles, along with chamber pressure measurements, were used to generate inferred enthalpy profiles.

Pyrometry was employed to measure the surface temperatures of ablating heatshield materials. Pyrometers were focused at locations on the heatshield surface that corresponded to the positioning of back-face thermocouples.

The Laser Wedge Recession (LWR) system was used to measure the ablation of the candidate heatshield materials as a function of time. A laser was used to project light onto the surface of the sample at a 45-degree angle relative to the surface normal. The reflection of the laser light was picked up by a receiver located 90 degrees from the light source. As the test material receded (ablated) normal to the surface, the laser beam appeared to be displaced along the surface plane of the material. The amount of displacement of the light was directly proportional to the amount of recession. A detailed description of this technique may be found in Reference 2.

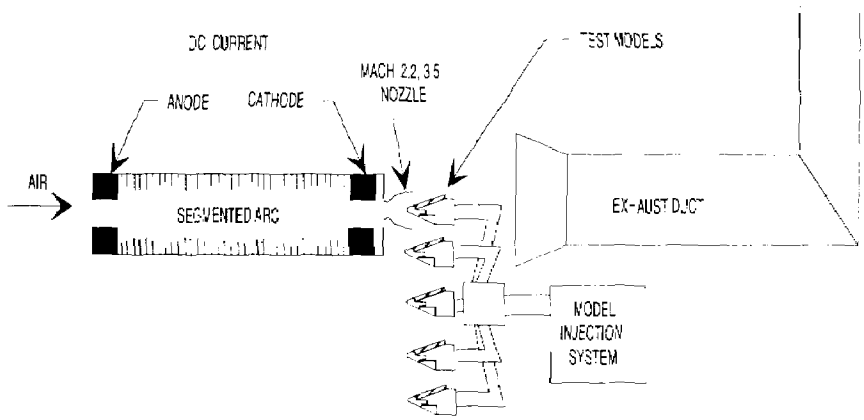

Figure 5—AEDC HEAT Facility

Motion picture cameras were used to provide surveillance and to record catastrophic failures if they occurred. These cameras were not relied upon to record data when testing heatshield material specimens.

Each model was instrumented with K-type thermocouples bonded to the back face of the material specimen. The measured data from these thermocouples were used to evaluate the relative insulation performance of the candidate materials used in the tests. Thermocouple locations coincided with the thermocouple

locations on the wedge calorimeter to ensure that the heating environment was known.

Test Description

Test Conditions—For the tests described in this article, a Mach 3.5 contoured nozzle having a throat diameter of 0.9 inch and an exit diameter of 3.00 inches was used. The facility operating conditions were adjusted to produce a desired heat transfer rate of 1065 BTU/ft^{2}sec on the model at an axial location 2.00 inches from the leading edge of the model (chamber pressure of 105 Atm, inferred enthalpy of 6200 BTU/lbm).

Models—Each material test specimen was machined to a length of 0.9 inch, a width of 3.0 inches, and a thickness of 0.375 inch. Model thickness was selected such that it was sufficiently thick to preclude burn-through, yet thin enough to provide sufficient heat transfer to the backface in a reasonable amount of time. The length and width of the test material specimens were dictated by the size of the standard holders used at the AEDC facility. The models were secured to the holders with a graphite clamp arrangement.

Holders—The test materials were mounted on heatshield wedge holders. A schematic of the model holder is shown in Figure 6. A single heatshield-material test specimen was attached to each holder. The upper surface of the holder, to which the test material specimen was attached, was inclined at a fixed angle of 15 degrees to the flow. The holder was made of copper, with additional thermal protection afforded by a leading edge of bulk graphite and by a generic carbon/silica phenolic insulator on the underside of the holder. This arrangement allowed the holders to be reusable.

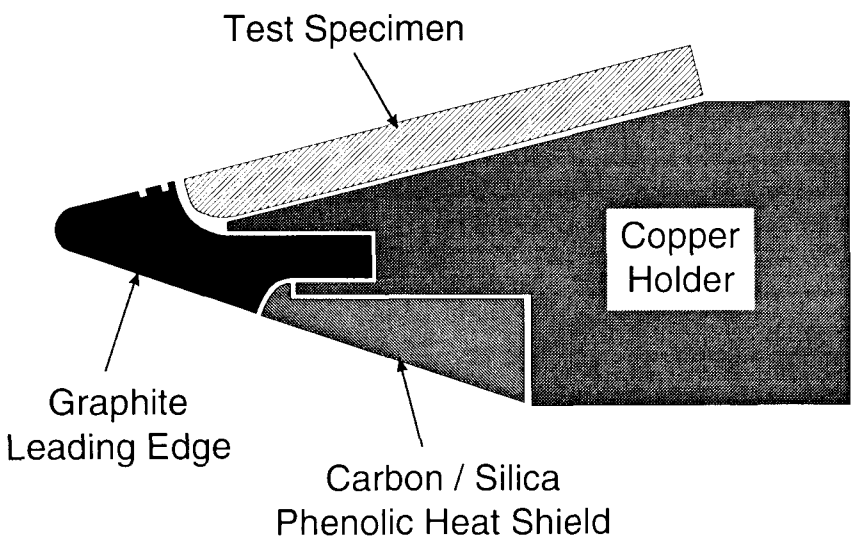

Holder Assembly (Not to Scale)

Figure 6—Schematic of Model Holder

Test Procedure

The heater was started and allowed to run for six seconds prior to the sweep of the calorimeters through the flow. This six-second interval allowed the arc flowfield conditions to stabilize. After the calorimeter sweep, a one-second elapsed time was allowed prior to model insertion. Models were introduced into the flow at a location where the leading edge of the model holder was 0.1 inch from the nozzle exit and were held there for seven seconds. After the last model exited the flow, the heater was shut down, and recording of recession data and pyrometer data was stopped. Backface thermocouple data were recorded for another 40 seconds after heater shutdown.

Ablation Test Results

The total recession data of pitch- and PAN-fiber-based carbon phenolic composite material are shown in Figure 7, along with data for the rayon-fiber-based carbon phenolic Navy reference material. These data were taken at a location on the centerline of the model 1.25 inches downstream of the leading edge at a time of seven seconds, corresponding to the end of the test. These results indicated that both pitch- and PAN-fiber-based carbon phenolic materials exhibited ablation performance that was generally as good as the rayon-fiber-based materials.

The centerline backface thermocouple data at a location 2.00 inches downstream of the leading edge, and at a time 20 seconds after the model entered the plasma arcjet flowfield, are shown in Figure 8. The pitch- and PAN-fiber-based composites exhibited backface temperatures near that of the reference material, indicative of thermal insulation performance as good as that of the reference material.

HEATSHIELD MATERIAL CHARACTERIZATION TESTING

SoRI is a not-for-profit, contract research organization located in Birmingham, Alabama. The Engineering Division of SoRI has conducted characterizations for high-temperature materials used for Navy and Air Force since the early 1960s. SoRI has developed many facilities and techniques for measuring the mechanical and thermal properties of materials at temperatures from cryogenic to 5500°F.

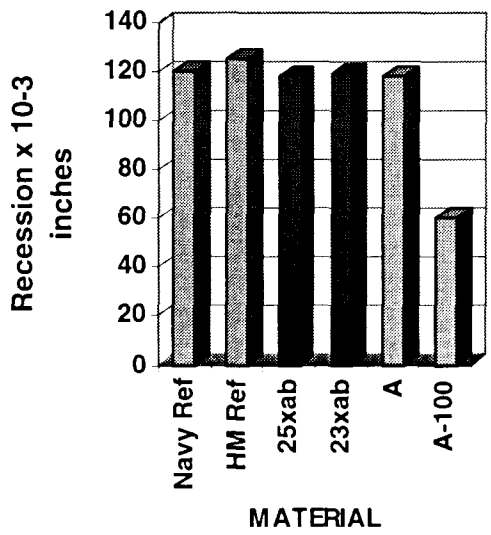

Figure 7—Recession Data

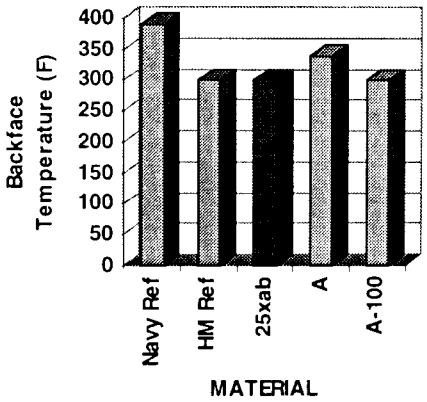

Figure 8—Backface Temperature

Tensile Strength and Elastic Modulus

Tensile strength and elastic modulus were measured in a gas-bearing tensile test facility developed by SoRI to evaluate the tensile properties of materials from ambient temperature to high temperatures. Coupon specimens contained in a furnace were loaded in tension-to-failure. Tensile load and tensile strain were continuously recorded during the test. Tensile strength was calculated from measured load at failure, and elastic modulus was calculated from the slope of the load-strain curve recorded during the initial part of the test. Quartz lamp furnaces were used for temperatures from ambient to ~1200°F; graphite furnaces were used for temperatures from 1200°F to 5500°F. Strain measurements were made with high-temperature clip-on extensometers. Load-time data were recorded for load rate control, load-strain data were recorded for preparation of stress-stain curves, and temperature-time data were recorded for low-temperature evaluations where heating rate was an important parameter. Ultimate tensile strength, elastic modulus, and strain-to-failure were calculated from the measured load-strain curve; each specimen was inspected for proper failure mode. Data tables, stress-strain curves, and summary graphs were reported.

Thermal Expansion

Thermal expansion was measured using dilatometers to record length changes of coupon specimens during heating. For temperatures up to 1500°F, quartz dilatometers were used; for temperatures up to 5500°F, graphite dilatometers were used. The dilatometers were calibrated on a regular schedule using the National Institute for Scientific Testing (NIST) fused silica standard for the quartz dilatometers and in-house developed ATJ graphite standards for the graphite dilatometers. For the carbon phenolic materials used in reentry body heatshields, heating rate is an important parameter at low temperatures. For the low-temperature runs with controlled heating rates, length changes were measured during continuous heating with linear variable differential transformers. Thermal expansion was calculated from the change in length that occurred from initial temperature to each temperature (final length - initial length); calculated expansion values were plotted versus temperature to create a thermal expansion curve. Values of instantaneous or secant coefficient of thermal expansion could be calculated from the thermal expansion curve.

Thermal Conductivity

The thermal conductivity was measured in the Comparative Rod Apparatus (CRA), which is used for temperatures up to ~2000°F. Measured thermal conductivity of carbon phenolic materials is dependent on thermal preconditioning, so that care must be given to describing the conditions of the material before the test and the actual conditions during the test.

The CRA used a "guarded" column containing two test specimens and two reference specimens. Heat flow was measured into and out of the column using the reference specimens, and temperatures were measured along the column. Thermal conductivity was calculated from the known heat flows and the

measured temperature gradients in the specimens. The specimen column was "guarded" with temperature profiles that matched those in the column to ensure that heat flow was one dimensional along the length of the column. Reference materials included copper, Armco iron, 316 stainless steel, and Pyroceram. References were selected to match the thermal conductivity of the material being tested. Test method measurement uncertainties were on the order of five percent.

Thermomechanical Test Results

Properties of the candidate heatshield materials were measured. Tests performed included tension at room and elevated temperatures, thermal expansion to 5000°F, and thermal conductivity to 600°F. Results of some of the tests are presented in Figures 9 through 12. Figures 9 and 10 show, as expected, that the high-strength, high-modulus T350 - 23 XAB and T350 - 25 XAB used in the PAN candidates produced the highest strength and highest modulus composites. These low-temperature-fired PAN fibers also yielded a lower thermal conductivity composite, as shown in Figure 12. The PAN conductivity characteristics showed little temperature variation between room temperature and 600°F. This behavior is desirable from a design standpoint. The pitch candidates also outperformed the Navy reference material with respect to thermal conductivity, which showed little variation with temperature. The pitch-fiber-based candidates did not perform as well as the PAN candidates with respect to tensile strength and modulus, but they were comparable to the Navy reference material. In the thermal expansion tests, all of the replacement material candidates performed better (expanded less) than the Navy reference material.

CANDIDATE HEATSHIELD MATERIAL

Test Conclusions

The results of the plasma arcjet ablation testing and the thermomechanical screening and characterization of alternate fiber carbon phenolic heatshield materials indicated that the ablation performance and thermomechanical properties of these materials were as good as or better than those of the AVTEX rayon-fiber-based material, the Navy reference material. All

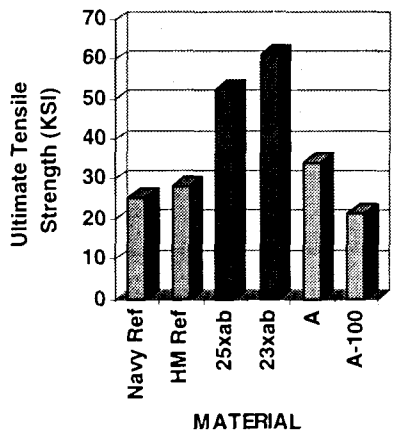

Figure 9—Room Temperature Tensile Strength

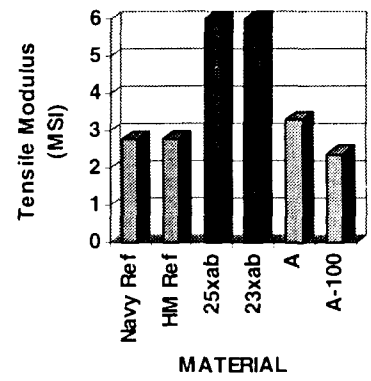

Figure 10—Room Temperature Tensile Modulus

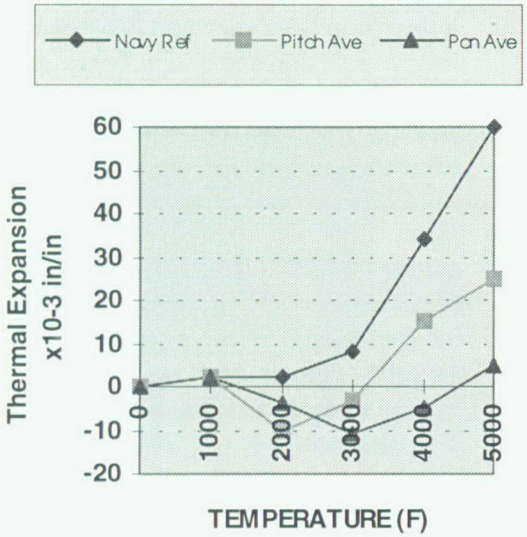

Figure 11—Thermal Expansion

candidates are undergoing further evaluation. The use of ground-test facilities and material characterization measurements is an effective means for screening alternative materials relative to the existing reference material. Ultimately, the overall performance of any replacement material must be determined in full-scale flight tests.

In the decision-making process associated with the choice of a replacement material, factors and issues in addition to material performance must also be considered. Many new, alternate replacement fibers were in the realm of R&D. The availability of such fibers is questionable from the standpoint of the ability to produce quantities necessary for component fabrication at an affordable cost. Replacement components must have a capability to meet mission requirements equivalent to the components of the existing systems. In addition, a replacement component must have minimal impact on the overall system, and that impact must be understood. A link must exist between the replacement component and current, existing ground-test and flight-test data bases.

Figure 12—Thermal Conductivity

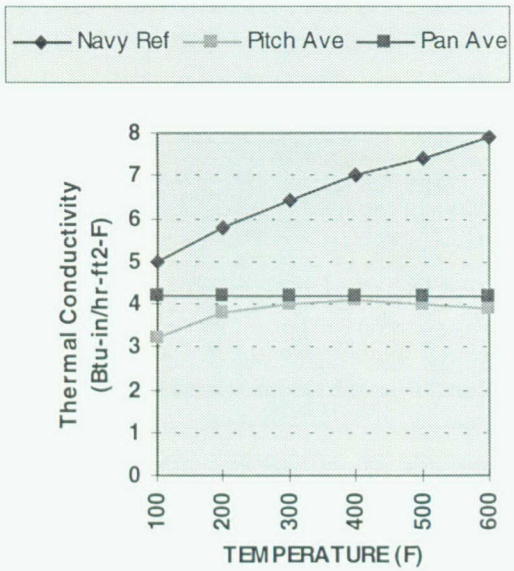

The replacement component must be affordable. Reductions in the cost of replacement components by a factor of two may be a required reality in the future. In an era with little or no new system production, manufacturers will not operate facilities in a continuous manner. The consistency of replacement components must be ensured and must not be subject to the start-up and shutdown cycles inherent in intermittent operation of material processing facilities.

Future Plans

Additional candidate materials have been identified, and test specimens will be produced, screened, and tested as appropriate. Testing similar to that described will take place on each of the candidate materials. Since many new materials are expected to be available for testing, productivity enhancements in the test procedures are being pursued. One such productivity enhancement is the development and use of a model holder to accommodate two material specimens on each model mount position. A double-wedge configuration, with material specimens on both the top and bottom surfaces, is planned to be utilized in future testing. A schematic of this arrangement is shown in Figure 13. A result of preliminary testing of a double-wedge calorimeter configuration, which mirrors the material test model, is shown in Figure 14. Gardon gages were mounted on the top and bottom of the double-wedge configuration at various locations to measure the heat flux to the calorimeter. The results of this test indicated that the plasma arcjet flowfield environment was uniform and symmetrical, and suitable for testing materials in a double-wedge model test configuration.

Ablation testing of actual heatshield materials, excised from conical frusta, is planned to assess the effects of aging on the ablation performance of these materials. To test these specimens in the present test setup would require the machining of the curved specimens into flat samples. Removal of stock from the inner and outer surfaces of the curved specimens may not be desirable, since the thickness of the flat specimen would be reduced from that of the curved specimen, and the stock removal process may alter the state of the "aged" material. A curved model holder, also shown schematically in Figure 13, has been designed, as has a curved calorimeter model. These items should allow the excised heatshield materials to be successfully tested in an ablative environment.

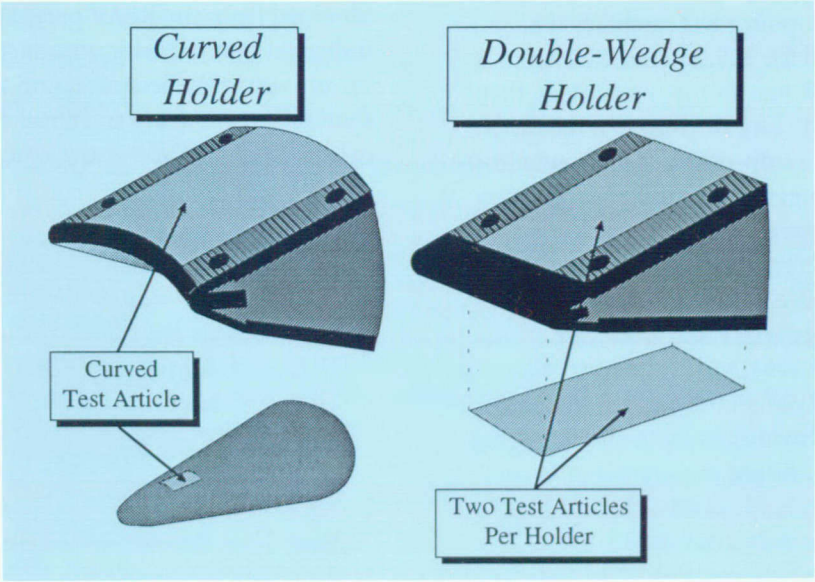

Figure 13—Schematic of Model Holder

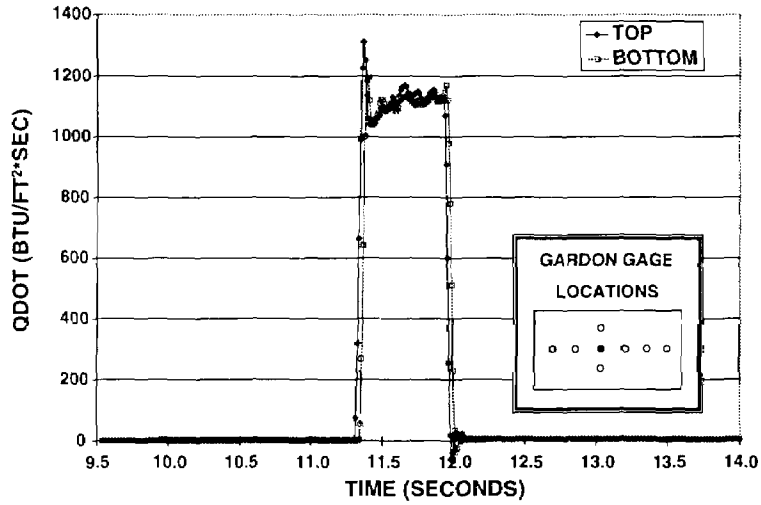

Figure 14—Gardon Gage Heat Transfer Results

Investigations are also planned to produce a simulated trajectory environment in the plasma arcjet. A wedge model with the ability to change its angle relative to the flow and to move toward the nozzle exit may be able to simulate conditions of increasing pressure and heating associated with reentry in the earth's atmosphere.

SUMMARY

U.S. strategic policy has established a continuing need for U.S. nuclear Strategic Forces. The NPR has set forth a strategy that preserves options for ramp-up to a reconstitution hedge or ramp-down to deep cuts from our current strategic reduction plan. Various studies have determined that the strategic industrial base is rapidly eroding due to an absence of ballistic missile development or production programs. RSAP has been established to maintain SLBM reentry systems beyond original design life and to maintain essential capability necessary to address aging phenomena and future requirements for in-service SLBM reentry systems. Results from a Reentry Systems Industrial Base Survey indicated that the reentry industrial base has undergone significant erosion. The reentry system afterbody heatshield was identified as a critical component that can no longer be manufactured and which is subject to aging effects. RSAP has established technical tasks to develop the technology necessary to support the replacement of operational heatshield systems. The results of plasma arcjet heater experiments and high-temperature mechanical properties characterization experiments have been presented that show the potential for the development of a non-rayon-fiber-based, tape-wrapped heatshield material system. Results obtained from the RSAP program to date have indicated that the basic approach holds promise for providing the technical and industrial foundation necessary to support the life extension of SLBM reentry systems.

REFERENCES

1. *Test Facilities Handbook*, Volume 1 and Volume 3, May 1992, Arnold Engineering Development Center, Arnold Air Force Base, Tennessee.

2. Sherrouse, P. And Carver, D., "Demonstrated Real-Time Recession Measurements of Flat Materials During Testing in High-Enthalpy Flows," AIAA Paper No. 92-0765, 1992.

THE AUTHORS

DR. ALFRED M. MORRISON

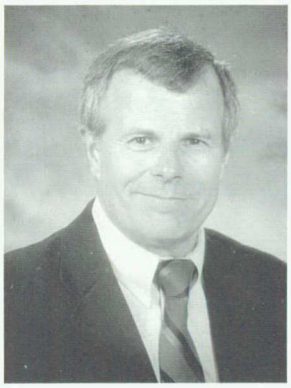

DR. ALFRED M. MORRISON is an SES/Senior Level engineer currently assigned to the Strategic and Strike Systems Department as Chief Scientist for Submarine Launched Ballistic Missiles and Reentry Systems. He has been involved in Strategic Missile: technology development, ground and flight testing, and reentry systems engineering. He was responsible for the technical direction of the NSWCDD reentry programs supporting Trident I, the Trident Improved Accuracy Program and Trident II. He is currently involved in the development of programs aimed at extending the life of deployed SLBM systems. He holds a B.S., M.S., and Ph.D. in aerospace and mechanical engineering from the University of Notre Dame. He is a member of the Naval Submarine League and the Society of Sigma Xi, and is an Associate Fellow of the American Institute of Aeronautics and Astronautics.

DR. JOHN S. VAMOS

DR. JOHN S. VAMOS is the Head of the Reentry Systems Branch in the Strategic and Strike Systems Department. He has been involved with the high-temperature aspects of hypersonic flow, reentry technology development, and reentry systems engineering for 24 years. He has a B.M.E. from Villanova University and a Ph.D. in astronautical and aeronautical engineering from Ohio State University. He is a member of the American Institute of Aeronautics and Astronautics and the Society of Sigma Xi.

Wind Tunnel Testing of Strategic Systems in NSWCDD's Tunnel #9

Mr. John A. Hill, Mr. John F. Lafferty, and Mr. Daniel E. Marren

Strategic reentry systems operate in the hypersonic flight regime. This environment is thermo-structurally the most severe and aerodynamically one of the least predictable for atmospheric flight. In order to improve the understanding of atmospheric reentry and thereby improve the accuracy and reliability of Navy Reentry Systems, Strategic Systems Programs (SSP) and the Naval Surface Warfare Center, Dahlgren Division (NSWCDD) funded the development of the world's most advanced hypersonic ground test facility, NSWCDD's Hypervelocity Wind Tunnel #9 (Tunnel 9). As technology advanced, Tunnel 9 has been upgraded to provide capabilities unmatched by any hypersonic ground test facility in the Department of Defense (DoD) or the National Aeronautics and Space Administration (NASA). Test facilities such as Tunnel 9 will be vital to reentry system life extension programs such as the Navy's Reentry System Applications Program (RSAP) and the Air Force's Reentry Vehicle Applications Program (RVAP). This article will discuss the history of the wind tunnel complex at White Oak, Maryland, the development and use of Tunnel 9 in support of strategic reentry systems, the transition of its use to other hypersonic systems, and the completion of upgrades to support these programs.

Introduction

Tunnel 9 located at the White Oak, Maryland, site of NSWCDD provides clean, uniform aerodynamic flowfields at high Reynolds numbers with relatively long run times. The Reynolds number is a nondimensional flow parameter that ratios the flight vehicle's inertial forces to its surface frictional forces and is used to determine the characteristics of the vehicle's boundary layer. Tunnel 9 has played a major role in the testing of strategic reentry systems, endoatmospheric interceptors, and aerospace plane programs. Specific testing areas include:

- Research into hypervelocity flow to understand flight vehicle stability characteristics, boundary layer transition, surface heat transfer, and aerodynamic forces

- Vehicle component testing to aid in systems development, for example, systems using jet interaction or flaps for control or testing hypersonic inlet designs

- ✦ Flight confidence testing to proof systems before flight testing such as shroud removal on interceptors
- ✦ Classified testing where the models and data can be protected at a government facility

Tunnel 9 Facility Description and Operation

Tunnel 9 is a blowdown facility that currently operates at Mach numbers of 7, 8, 10, 14, and 16.5. Tunnel 9 uses pure nitrogen as the working fluid. The test section is over 12 feet long and 5 feet in diameter, which enables testing of full-scale model configurations. Ranges for Reynolds numbers and supply conditions are listed in Table 1.

Table 1—Tunnel 9 Nominal Capabilities

Mach Number	Supply Pressure Range (psia)	Nominal Supply Temperature (degrees F)	Reynolds Number Range ($X10^6$/ft)	Run Time Range (seconds)
7	2,600 - 11,800	3,000	3.7 - 15.8	1 - 6
8	1,000 - 12,000	1,100	4.5 - 50.0	0.33 - 6
10	500 - 14,000	1,350	0.86 - 20.0	0.23 - 8
14	100 - 20,000	2,750	0.072 - 3.8	0.7 - 15
16.5	21,000	2,880	3.24	3.5

During a typical run, the vertical heater vessel is used to pressurize and heat a fixed volume of nitrogen to a predetermined pressure and temperature. The test section and vacuum sphere are evacuated to approximately 1 mmHg and are separated from the heater by a pair of metal diaphragms. When the nitrogen in the heater reaches the desired temperature and pressure, the diaphragms are ruptured. The gas flows from the top of the heater, expanding through the contoured nozzle into the test section at the desired test conditions. The nozzle internal shape changes smoothly from the nozzle throat to the test cell in a contour designed specifically for each Mach number. As the hot gas exits the top of the heater, cooler nitrogen from four pressurized driver vessels enters the heater base. The cold gas drives the hot gas in a piston-like fashion, thereby maintaining constant conditions in the test section during the run. A layout of Tunnel 9 is shown in Figure 1. A complete description of the current Tunnel 9 capabilities can be found in Reference 1.

HISTORY OF HYPERSONIC FACILITIES AT NSWCDD AND DEVELOPMENT OF TUNNEL #9

The following section is included to provide insight into the origin of the wind tunnel complex at the White Oak site of NSWCDD.

This historical account is based on Reference 2 and is largely anecdotal. However, it provides a unique perspective on the events and facilities ultimately leading to the development of Tunnel 9. In addition, Figure 2 gives a pictorial perspective of the historical programs and facility developments to support those programs.

As World War II came to a close in Europe in the spring of 1945, the advancing Americans captured a German installation at Kochel in Bavaria. This site included two supersonic wind tunnels. These tunnels had been recently moved to Kochel, in response to an Allied bombing raid in August of 1943, from their original home at the Pennemunde Rocket Development Station. These extremely valuable, unique

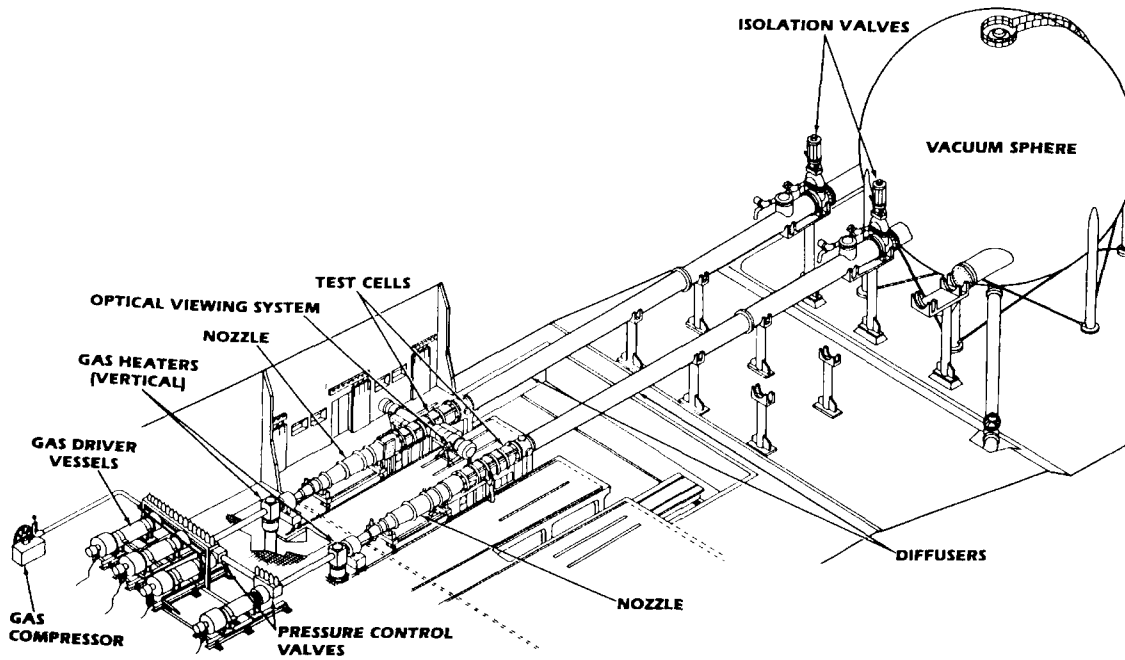

Figure 1—Hypervelocity Wind Tunnel #9

facilities were worth moving because they were being used in the development of German weapon programs, such as the V-2 Rocket. In July 1945 the custody of these facilities was awarded to the U.S. Navy, and by January 1946 they had been dismantled and transported to the United States. Custody of the tunnels was passed from the Chief of Naval Operations to the Bureau of Ordnance to the Naval Ordnance Laboratory at White Oak, Maryland. German scientists from the Kochel Facility were transferred to White Oak starting in 1946 to assist in the installation and modernization of the two tunnels designated Supersonic Tunnel 1 and Supersonic Tunnel 2. The two 40- × 40-cm tunnels were operational for shakedown and calibration purposes by July of 1948, and in February of 1949 Research and Development (R&D) and Test and Evaluation (T&E) testing had begun. Over the years, these tunnels were upgraded and modernized. The hardware from Tunnel 1 was eventually used to create a vacuum chamber for calibrating instrumentation, and Tunnel 2 was finally deactivated in the early '90s. Many advances in designing and building supersonic testing facilities, as well as improving measurement techniques, were developed in these two tunnels. Several well-known weapon systems were also ground tested in these two facilities, including the Navy's Polaris Mk-1 and Mk-2 Reentry Bodies (RBs). Almost 60 years after Tunnel 1 first became operational at Pennemunde, the hardware from two of the world's first supersonic wind tunnels can still be seen while touring the Tunnel Facilities at White Oak.

With the nucleus of the German scientists and financial backing from the Navy, other facilities were developed at White Oak. Tunnel 3

became operational in 1949 and was primarily used for supersonic diffuser research. The design of the 16- × 16-ft propulsion wind tunnel diffuser at the Arnold Engineering Development Center (AEDC) in Tullahoma, Tennessee, was based on research from Tunnel 3. Tunnel 3 was given to the Aerospace Engineering Department of the University of Maryland in 1955. Tunnel 4, the first hypersonic (Mach numbers >5) tunnel at White Oak became operational in 1950. It had a 12- × 12-cm test section and was the first tunnel to reach Mach 10 without liquefying the air during the temperature loss incurred when the flow is expanded through the nozzle. In 1957, the nozzles, test section, and diffuser were given to the Von Karman Institute of AGARD in Brussels, Belgium, and replaced by a larger test cell and axisymmetric nozzle with a 12-inch exit diameter. The first Mach 10 aerodynamic measurements on the Polaris Mk-1 RB were made in Tunnel 4. It was modernized in 1964 to operate between Mach 10 and 18. The technical advances made to reach these higher Mach numbers, such as replacing air with hot, pressurized pure Nitrogen as the working fluid, would aid in the design of future wind tunnels including Tunnel 9. Tunnels 5 and 7 were planned but never completed, and Tunnel 6 was built in 1950 to study supersonic turbulence and shock-wave phenomena. The next significant development in the area of hypersonics was the construction of Tunnel 8. Tunnel 8 was completed in 1956 and was nominally a 20-inch diameter high Reynolds number facility operating between Mach 5 and Mach 10. Tunnel 8A, installed in 1970, was a pilot facility to Tunnel 9. Its 24-inch nozzle exit diameter produced extremely uniform Mach 18 flow and was used for high-altitude testing of various reentry bodies and the space shuttle.

The majority of the hypersonic testing in the '60s and '70s supported strategic offensive and

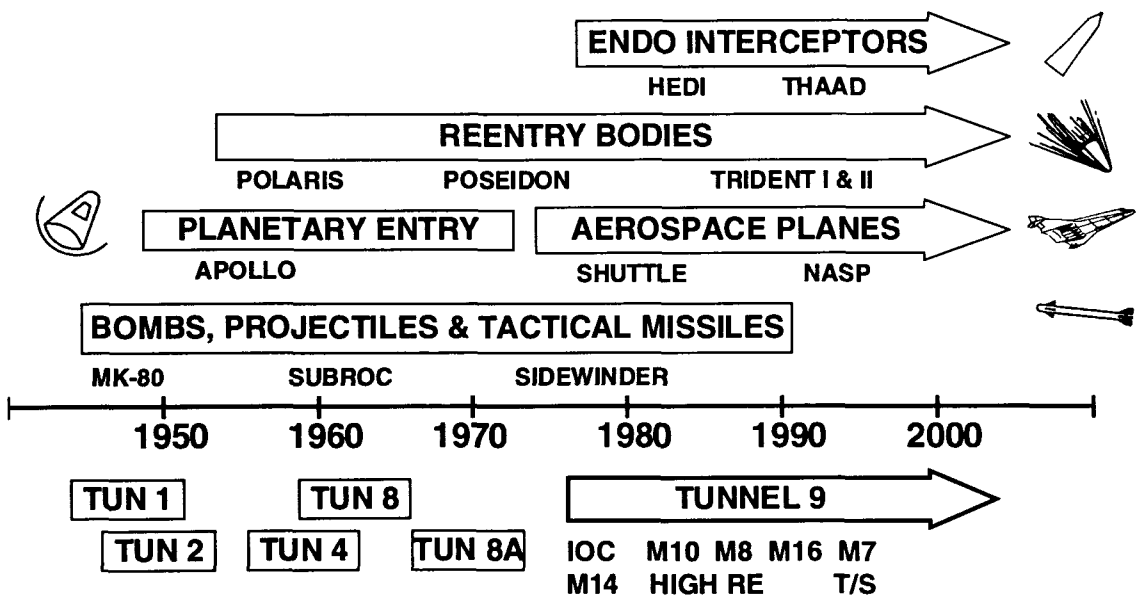

Figure 2—History of NSWCDD Wind Tunnel Testing and Development

defensive weapon systems. With the escalation of the Cold War, it was necessary to deploy accurate and reliable systems. The requirement for reliable and accurate systems drove the requirements for understanding the aerothermodynamic environment of reentry. In order to improve the understanding of reentry, a new facility with enhanced capabilities was envisioned. Tunnel 9 was designed using all the technological advances developed in the previous 15 years. Tunnel 9 was originally planned to produce Mach 10, Mach 15, and Mach 20 flow through a test cell that could accommodate full-scale reentry bodies. Three axisymmetric contoured nozzles would each be resident in a different leg of the tunnel, but all three would take advantage of a common high-pressure driver system and vacuum sphere.

The contract to build Tunnel 9 was awarded in 1967, and by 1972 most of the major facility items had been completed. A shakedown of the facility began in 1973 and was completed by 1977. However, the initial operating conditions varied somewhat from the original plan. The Mach 20 leg has yet to be realized, and the planned Mach 15 capability was modified to achieve Mach 14. By the end of 1978, the world's newest and most advanced hypersonic ground test facility was operating at Mach 10 and Mach 14. The advances that made Tunnel 9 unique, when it was built and which still maintain its position today, are its combination of operational envelope, its capability for testing full-scale models, and its long run times, which allow for an order of magnitude more data per run than shock tunnels. Long, contoured axisymmetric nozzles also provide the uniform flow ideal for aerodynamic testing. After Tunnel 9 came on-line in the late '70s only Tunnels 2, 8 and 8A were still in operation.

As a result of a 1976 Joint Logistic Commanders Study of "Consolidation of Functions and Facilities," Tunnel 9 was identified as DoD's primary hypervelocity wind tunnel, and the Air Force's Tunnel F at AEDC was subsequently closed. In 1984, the NSWCDD tunnels lost their Navy institutional funding, causing the full cost of testing to be borne by the test-sponsoring organizations. NSWCDD made a cost reduction decision to no longer support the maintenance and repair of the older wind tunnel facilities at White Oak. The test capabilities provided by the older tunnels could be duplicated elsewhere in the country. Since Tunnel 9 remained unique in its test capabilities, maintenance and repair assets were concentrated on Tunnel 9.

TUNNEL #9 TESTING FOR STRATEGIC REENTRY SYSTEM PROGRAMS

Tunnel 9 was originally built to support the Navy's Trident Missile Program, specifically to test the effects of reentry on full-scale shapes. The Navy's Mk-500 Maneuvering Reentry Body (MaRB) was planned to be the first reentry system tested in Tunnel 9. It was designed to use its high velocity and maneuverability to defeat in-place Ballistic Missile Defenses by evading the interceptors. When contracting issues delayed Tunnel 9's opening, the Mk-500's ground test program was completed elsewhere. Tunnel 9's initial operational capability in 1977 did directly support the assessment of aerodynamic drivers for the SSP under the Improved Accuracy Program. Data from this testing was used in the design of the D5/Mk-5 reentry system, the first SLBM system with hard target kill capability.

Although other tunnels within the United States can produce high Mach numbers, only Tunnel 9 can produce a simulation that matches both Mach and Reynolds numbers, in the altitude regime critical to strategic offensive weapon systems, for sufficient test times. Mach number effects and Reynolds number effects cannot be accurately scaled from lower Mach number and Reynolds number data obtained in other facilities, especially in the altitude regime where turbulent boundary layers dominate the flowfield. Tunnel 9's ability to obtain transitional and fully turbulent boundary layers on full-scale models and over-scale nosetips

makes it ideal for testing strategic reentry systems.

Over the last 20 years, Tunnel 9 has provided a broad spectrum of reentry systems testing from static stability and drag testing of the Navy's Mk-4, to specialized testing to determine the effects of base pressure, at high angles of attack, on stability moments for the Navy's Mk-5. The first strategic reentry system tests in Tunnel 9 were begun in 1977 and included the Advanced Maneuvering Reentry Vehicle (AMARV) sponsored by the DoD Joint Advanced Ballistic Reentry Systems (ABRES) Program. In 1979, the Navy's Strategic Systems Program Office (SSPO) began sponsoring a series of tests of the Mk-4 reentry system. This series included testing to determine the aerodynamics and boundary layer heat transfer of the ablated nosetips shapes and testing to study high-altitude, high angle-of-attack aerodynamics. Descriptions of these tests can be found in References 3 through 6.

During the initial flight testing of the Mk-5 reentry system, flight data indicated that the center of pressure of the Mk-5 at high angle of attack was different than predicted. Very specialized testing in Tunnel 9 verified the theory that explained this flight anomaly.

The Air Force's Intercontinental Ballistic Missile (ICBM) Office also performed tests in Tunnel 9. In addition to the ABRES tests, the Air Force sponsored tests that included reentry vehicle (RV) nosetip studies and testing of other possible future reentry systems, such as kinetic energy impactors. Besides DoD agencies, DoD contractors also used internal R&D funding to sponsor reentry system testing in Tunnel 9. An example of this is the Lockheed Missile and Space Company test of a maneuvering RB concept in 1981.

Even though Tunnel 9 was originally developed primarily for testing strategic reentry systems, as national interest was kindled in the Strategic Defense Initiative (SDI), known as "Star Wars," the interest in hypersonic interceptors also increased. With the potential proliferation of weapons of mass destruction and international terrorism, interest in the hypersonic interceptor concepts will remain high.

In the '80s, testing of strategic interceptors became one of Tunnel 9's primary business lines. At this time, interest in developing other hypersonic vehicle systems, such as the National Aerospace Plane (NASP), also increased. The primary focus of testing in Tunnel 9 switched to the testing of other hypersonic vehicles, such as NASP, and strategic and theater missile defense systems. Specific enhancements and facility developments to support these programs were undertaken, which allowed Tunnel 9 to maintain a unique place in the hypersonic ground test community.

TUNNEL #9 TESTING OF OTHER HYPERSONIC SYSTEMS

Numerous experiments have been performed in Tunnel 9 that have supported SDI and the Ballistic Missile Defense Organization (BMDO) endoatmospheric interceptor programs. The unique capabilities of Tunnel 9 have been included in the BMDO T&E infrastructure for critical testing in the areas of aerodynamics, aerostability, divert and control jet interaction, aero-optics, window cooling, and thermal structural testing. These capabilities have proven to be particularly important to the Army's High Endoatmospheric Defense Interceptor (HEDI), Theater High-Altitude Area Defense (THAAD), and the Israeli/U.S. Arrow missile programs, where such testing is critical. Tunnel 9's operational envelope, pictured in Figure 3, is also well suited to support the requirements of the Theater Missile Defense (TMD) development testing.

The TMD endoatmospheric interceptor programs have taken advantage of Tunnel 9's unique capabilities to develop hypersonic

interceptors that defend against a variety of threats at all levels of the atmosphere. For these hypervelocity intercepts, highly accurate systems are required. Lessons learned on earlier interceptor flight tests identified the need for flight duplication during ground testing. Issues with missile shroud separation, Reynolds number scaling, aero/thermal effects on sensor window heating, jet interaction effects, and aero/optics are dependent on true flight duplication of important flight parameters, including long run times consistent with endgame scenarios. The need for highly reliable, realistic T&E is paramount.

During the 1980s there was also a renewed interest in hypersonic flight vehicle development. NASP, the primary program during this time, used Tunnel 9 extensively for high Mach number aerodynamic and scramjet inlet testing. High Mach number testing is critical to the development of such a vehicle because the extrapolation of data to higher Mach numbers is not reliable for these complex, high lift-to-drag ratio (L/D) configurations. Engine inlet design and testing provides a significant challenge for NASP due to the engine/airframe integration necessary for hypersonic cruise scramjet operation. The entire flowfield ahead of the scramjet affects the engine inlet flowpath, thereby coupling the engine development with the aerodynamic flowfield. Tunnel 9's high Mach number capability, long run times, and large test cell provided the high data rates necessary to meet the NASP ground test needs.

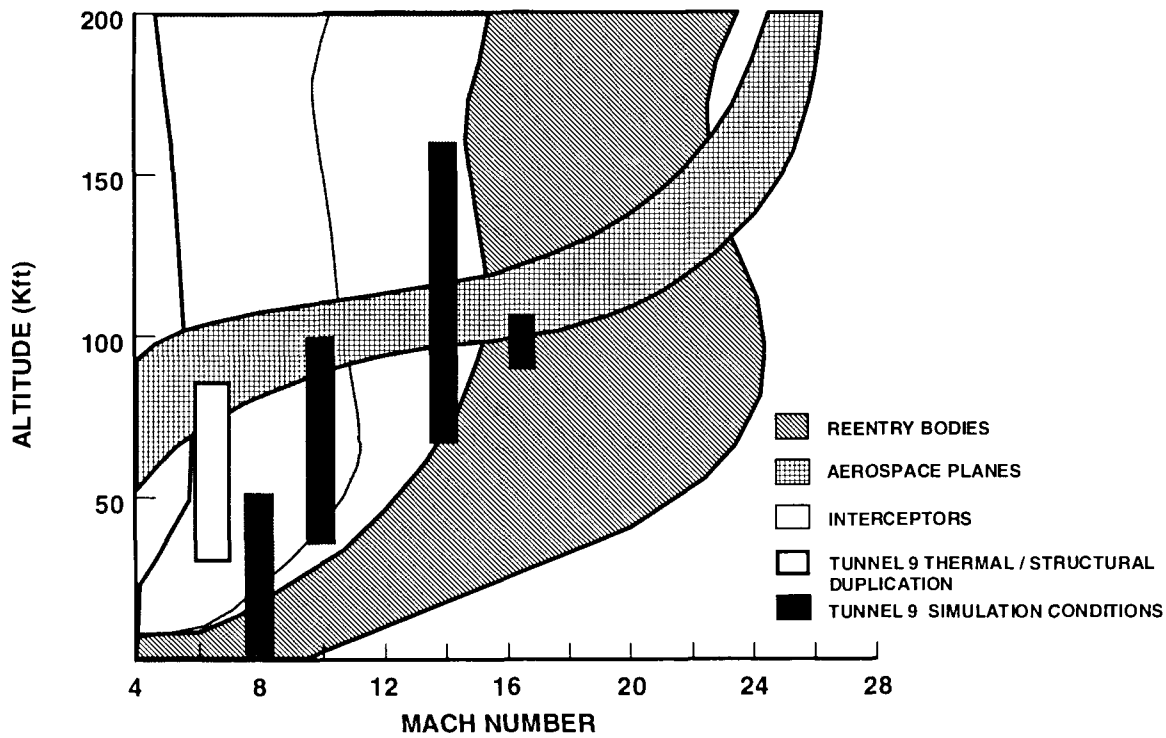

Figure 3—Tunnel 9 Operating Conditions

During the early stages of the NASP program, multiple aerospace contractor teams were in competition. Each team provided a different configuration. Multiple full-body aerodynamic configurations and engine flowpath/scramjet inlet tests were performed in Tunnel 9.[7,8] Full-body aerodynamic and inlet configuration testing at Tunnel 9 was enhanced by the ability to test large, heavily instrumented models. Inlet models are the largest nonpitching models tested to date in Tunnel 9, reaching lengths exceeding 10 feet. Long run times allowed inlet models to be started, unstarted, and restarted during a single run to assess the dynamic nature of the process.

Most of the testing described in the preceding sections required upgrades in instrumentation and tunnel capability or both to meet the data collection requirements specified by the sponsors. A discussion of some of the most important facility upgrades follows.

UPGRADES TO TUNNEL 9 TO SUPPORT STRATEGIC SYSTEMS

Mach 10 High Reynolds Number

In order to obtain natural boundary layer transition on full-scale reentry body frustra and oversized reentry body nosetips, very high Reynolds numbers are required. To accurately predict the aerodynamic characteristics of an RB, it is necessary to know when and where on the body the boundary layer transitions from laminar flow to turbulent flow. Only in a facility that can simulate full-flight Mach and Reynolds numbers concurrently can this type of data be generated. To achieve these flow parameters, the Mach 10 leg of Tunnel 9 was significantly redesigned.[9] The nozzle supply pressure was increased to 15,000 psi, resulting in a tenfold increase in the mass flow rate through the test cell. The pressure and mass flow increases resulted in a fourfold increase of Reynolds number from 5.4×10^6 to 20×10^6. This Mach 10 high Reynolds number capability allowed boundary layer transition studies to be completed on Navy reentry systems.

Mach 14 High Altitude

As a reentry body descends through the atmosphere, the aerodynamic stability of the vehicle drives any angle of attack towards zero. This phenomena is known as angle-of-attack convergence. During the testing of the Navy's Mk-4 reentry system, the predicted angle-of-attack convergence was not observed. If any aerodynamic parameter cannot be accurately predicted, it will be not be properly modeled in fire control, resulting in an uncertainty that decreases a weapon system's accuracy. Heatshield outgassing was postulated as a possible culprit, but there was no way to test the theory.

Heatshield outgassing occurs at high altitudes when the friction created by the air begins to heat the heatshield. As the temperatures on the heatshield increase, volatiles begin to percolate to the heatshield surface and are injected into the boundary layer. This mass injection into the boundary layer changes the nominal boundary layer characteristics, creating a local change in all of the aerodynamic parameters in the area of the mass injection. The question to be answered was, "Were the aerodynamic changes observed in flight caused by heatshield outgassing?"

In order to test this theory, a technique for simulating mass addition to the boundary layer using porous models was designed, developed, and characterized at NSWCDD White Oak.[10] This technique, combined with the ability to simulate very high altitudes, was developed for the Mach 14 leg of Tunnel 9. The resultant test series verified the theory that heatshield outgassing at high altitudes could generate the aerodynamic forces necessary to recreate an observed flight test anomaly.[6] The data from these tests were used to adjust aerodynamic models and SLBM fire control.

OTHER UPGRADES

Mach 8 High Dynamic Pressure

During the early development of high-speed endoatmospheric interceptors, designers needed a way to protect the critical seeker windows from the harsh environment experienced during flyout. A protective shroud was developed, which was to be ejected from the infrared guided seeker before final homing. Lessons learned on earlier interceptor flight tests identified the need for flight duplication. Problems involving shroud failure on certain interceptor flight tests were partially due to improper scaling from smaller scale wind tunnel models, which were ground tested at lower dynamic pressures. A capability was developed for Tunnel 9 that provided very high dynamic pressure (~100 psi), resulting in the desired environment.[11] Subsequent shroud designs were validated in Tunnel 9 using full-scale hardware at flight dynamic pressures in the Mach 8 test leg, which are described in References 12 and 13. We believe testing with this upgraded capability contributed greatly to the total success of follow-on flight tests.

Mach 7 Thermal and Structural Facility

The Mach 7 Facility was developed with funding from BMDO. BMDO is developing high-speed endoatmospheric interceptors that encounter severe aerothermal environments during the unshrouded endgame portion of flight. Seeker window survivability, material structural degradation due to thermal loading, and degradation of seeker performance, are all important design considerations. Earlier endoatmospheric interceptor designs utilized sophisticated seeker window cooling techniques to protect the seeker window from these extreme conditions. The penalties for such cooling schemes are optical aberrations and distortion of the target signal, as well as adding weight and complexity to the missile. Aberrational characteristics of windows, such as attenuation, boresight error (BSE), and blur have an adverse effect on seeker performance at high speeds. Therefore, evaluation of interceptor performance in a ground test facility that can provide full-flight duplication will greatly reduce risk to the program. No existing facility could provide full-flight duplication with run times comparable to endgame scenarios. Such a facility was obtained by upgrading Tunnel 9.

The Mach 7 Thermal and Structural Facility operates similarly to Mach 14. Mach 7 utilizes the high pressure and temperature capability of the Mach 14 heater and concentrates that high enthalpy flow in a smaller, high-energy core. Using the Mach 14 supply plenum, the flow is expanded to only Mach 7, maintaining high enough pressure and temperature to provide full-flight duplication. To achieve flight duplication at Mach 7, supply temperatures of 3000 degrees Fahrenheit are required. Reference 14 provides a complete description of the Mach 7 Facility and calibration.

Mach 16.5

During the development of NASP and other planetary entry vehicles, extrapolation to high Mach numbers from existing data bases was insufficient to model the complex, high-speed inlet flows and to predict drag on the vehicles. The NASP program funded a development to increase the Mach number capability to Mach 16.5. This development leveraged off the Mach 14 Heater and Nozzle and used the phenomenon of supercooling to achieve flowfields, extending the current data base to more realistic operational envelopes for these vehicles.[15]

Even though these upgrades were not originally developed to support strategic systems, they will provide ground testing opportunities not available in the past to strategic system developers. For example, the Mach 7 or 8 facility could be used to test a braking system for a deep earth penetrator that

was deployed from a submarine launched ballistic missile (SLBM), traveled 4000 miles to reach the target, and needed to be slowed to optimum earth entry angle and velocity.

FUTURE REQUIREMENTS

Reentry Systems Applications Program

Tunnel 9 is part of the industrial base required for the design, development, testing and deployment of strategic reentry systems. This industrial base is rapidly eroding primarily because there are currently no plans to build any new strategic missile or reentry systems. With the reductions in strategic nuclear forces and decreasing defense budgets, economics has forced the military to extend the service life of our current nuclear arsenal. In response to the eroding industrial base and the requirement to extend the life of deployed systems, Congress has initiated RSAP. This program has both a Navy and an Air Force component. The objective of this program is to maintain the minimum industrial base so that aging parts may be replaced or refurbished, thereby allowing the extension of the service life of currently deployed reentry systems from 20 to as many as 60 years. RSAP has recognized that Tunnel 9 is an integral part of this industrial base. Therefore, as part of its "Capability Retention Task," the Navy's RSAP program has pledged to provide an annual testing budget to help ensure Tunnel 9 remains viable and available. This budget will be used to test RSAP specific products, such as tests of aged components or tests to requalifiy replacement parts for flight. The budget could also be used to test systems to meet future reentry systems requirements or even to upgrade the tunnel's capability. The first RSAP-sponsored test in Tunnel 9 was completed in April 1997.

With treaties limiting the number of nuclear delivery systems, it is clear that the Navy's systems will have to perform current, and in the future maybe even additional, missions with fewer RBs. To do this, could require enhanced performance or even upgraded systems. Increasing the performance or capabilities of currently deployed systems to meet future requirements would require use of the entire industrial base, including Tunnel 9. Fortunately, even without recent funding from strategic weapon developers, Tunnel 9 has remained viable by transitioning from strategic to other types of testing and by constantly upgrading its capabilities. RSAP intends to help Tunnel 9 remain available now and in the future as an integral component of the industrial base.

Ballistic Missile Defense Office

BMDO continues to have a need for the unique capabilities of Tunnel 9. BMDO requirements include the need to test full-scale interceptors in an environment that duplicates flight. These requirements translate to the need to test larger models in full-flight environments, the addition of instrumentation upgrades that complement the long run times and high heating environment of the thermal and structural facility, and the capability to test reaction control systems in these severe aerothermal environments.

IN CONCLUSION

NSWCDD's site at White Oak, Maryland, has been closed by the 1995 Base Relocation and Closing (BRAC) Commission. As part of the base closure, Tunnel 9 was declared excess by the Navy. To prevent the loss of this unique national asset, U.S. Strategic Forces Command and BMDO proposed that Tunnel 9 continue operations under BRAC reuse provisions. Under this plan, the facility and the personnel billets will be transferred from the Navy to the Air Force to be managed as part of the AEDC. This transfer is scheduled for October 1, 1997. Thus, Tunnel 9, the legacy of Navy high-speed wind tunnel testing, will remain in operation at the White Oak site.

This article has provided the historical perspective to show why a facility like Tunnel 9 was developed by the Navy at White Oak, how it was integral to the development of currently deployed reentry systems, how it has remained viable over the years, and why it is imperative that it exist in the future to support strategic reentry system testing.

REFERENCES

1. Boyd, C. and Ragsdale, W.C., *Hypervelocity Wind Tunnel 9 Facility Handbook*, Third Edition, NAVSWC TR 91-616, Silver Spring, MD, Dec 1991.

2. Hastings, S.M., *The NSWC/WOL Wind Tunnels—A Chronology*, Unpublished K-20 Records, Silver Spring, MD, Aug 1979.

3. Jobe, M.D. et al., *Bi-Modal Flowfield Feasibility Demonstration in the NSWC/WO Hypersonic Tunnel (WTR 1319)*, NSWC MP 79-217, Silver Spring, MD, May 1979.

4. Ragsdale, W.C. et al., *High Mach Number Aero-Stability Tests with Ablated/Eroded Nosetip Shapes (WTR 1367)*, NSWC MP 82-544, Silver Spring, MD, Nov 1982.

5. Hedlund, E., *High Altitude Outgassing Test WT-315*, Wind Tunnel Test Report, Silver Spring, MD, Dec 1986.

6. Fiscina, C., *High Altitude Aerodynamic Tests With Simulated Heat-Shield Outgassing*, NSWC 82-572, Silver Spring, MD, Dec 1982.

7. Collier, A.S. et al., *The National Aerospace Plane Model C+ Wind Tunnel Test in the Hypervelocity Tunnel No. 9*, NSWCDD/TR-94/146, Silver Spring, MD, Apr 1994.

8. Lafferty, J.F. and Swinford, N.F., *Naval Surface Warfare Center Hypervelocity Wind Tunnel No. 9 NASP High-Speed Inlet Test WTR 1609*, NSWCDD/TR-93/90, Silver Spring, MD, Dec 1993.

9. Kavetsky, R.A. and Hill, J.A.F., *Mach-10 High Reynolds Number Development in the NSWC Hypervelocity Facility*, AIAA-85-0054, Reno, NV, Jan 1985.

10. Smith, T.S., *Theory and Experimental Verification of Compressible Low Density Subsonic Flow Through Curved Porous Surfaces With Non-Uniform Thicknesses*, AIAA-87-1387, Honolulu, HI, Jun 1987.

11. Swinford, N.F., *Hypervelocity Tunnel 9 Mach 8 Calibration*, NSWCDD/TR-93/40, Silver Spring, MD, Mar 1994.

12. Resch, L. et al., *Hypersonic Shroud Separation Testing At The Naval Surface Warfare Center Hypervelocity Wind Tunnel 9*, AIAA 92-2757, Huntsville, AL, May 1992.

13. Resch, L. et al., *Hypersonic Shroud Separation Testing and Modeling Capabilities at the Naval Surface Warfare Center Hypervelocity Wind Tunnel 9*, AIAA 94-2495, Colorado Springs, CO, Jun 1994.

14. Lafferty, J.F. and Marren, D. E., *Hypervelocity Wind Tunnel No. 9 Mach 7 Thermal Structural Facility Verification and Calibration*, NSWCDD/TR-95/231, Silver Spring, MD, Jun 1996.

15. Lederer, M.A., *Hypervelocity Wind Tunnel Number 9 High Mach Number Development Program*, NSWCDD/TR-94/96, Silver Spring, MD, Dec 1994.

THE AUTHORS

Mr. John A. Hill

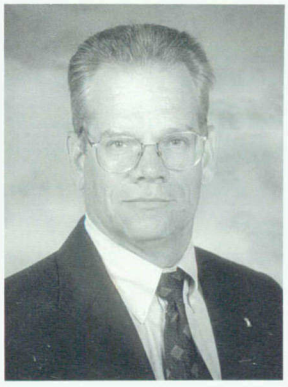

MR. JOHN A. HILL received his B.S. in aerospace and ocean engineering from Virginia Polytechnic Institute and State University in 1978, and his M.S. in aerospace engineering and applied mechanics from the University of Cincinnati in 1979. John joined the Flight Mechanics Group of the Reentry Systems Branch at White Oak in 1981. During his career at NSWCDD, John has been an analyst, task leader, and program manager for Navy- and SSP-sponsored programs. He is currently a Senior Reentry Systems Consultant to SSP's Reentry Branch, where he develops program plans; interfaces with DoE Laboratories, other DoD and Government Agencies, and DoD Prime Contractors; defines and directs ground test programs; and aids SP-282 in proposing and managing Advanced Technology Demonstrations (ATDs), Advanced Concept Technology Demonstrations (ACTDs), and special flight test programs. John is also currently managing NSWCDD's RSAP efforts where NSWCDD is providing RB nosetips, RB heatshields, and ground testing to the entire program.

Mr. John F. Lafferty

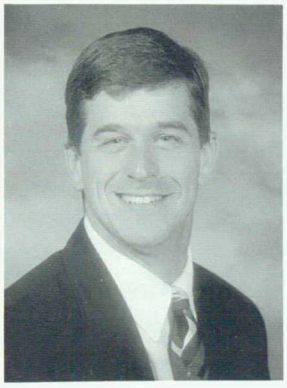

MR. JOHN F. LAFFERTY received his B.S. in aerospace engineering from the University of Cincinnati in 1987 and his M.S. in engineering management from the University of Maryland in 1992. He joined the Aerodynamics Branch of NSWCDD in 1985 as a co-op student trainee and was transitioned to full-time in 1987. John is a senior project leader, a group leader, and a technical expert in the field of advanced aerodynamic facility development at the Hypervelocity Wind Tunnel No. 9. Over the past few years, John has been the project engineer for the development of the newest upgrade to Tunnel 9—the development of the Mach 7 Thermal/Structural Facility. He is currently the lead project leader for the RSAP Tunnel 9 test program, which is being conducted in close coordination with the Reentry Systems Branch personnel and Navy SSP. John is a senior member of the AIAA and a member of the AIAA Aerodynamic Measurement Technology Technical Committee.

Mr. Daniel E. Marren

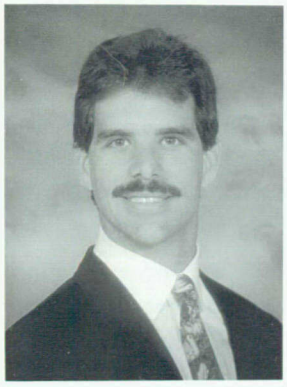

MR. DANIEL E. MARREN is currently the Aerodynamics Group Leader at NSWCDD's Aerodynamics Branch in White Oak, Maryland. Dan has worked at NSWCDD since 1985. Among his responsibilities are the planning and executing of wind tunnel test programs for various sponsors, costing and scheduling of all wind tunnel programs for NSWCDD's Tunnel 9, and the planning of facility upgrades and developments to satisfy specific program needs. Previously Dan has served as ground test coordinator for U.S. Navy SSP programs, providing evaluation and consulting for ground testing plans. Most recently Dan has been working as the Tunnel 9 task manager for BMDO testing at Tunnel 9. Dan received his B.S. degree from the University of Cincinnati in 1987 and an M.S. in engineering management from the University of Maryland in 1992.

Evaluation of Reentry Systems Nosetips and Heatshields Using an Arc Heater Facility

Mr. Michael J. Gillum and Dr. Leo P. O'Hare

The analysis and ground testing of reentry body nosetip and heatshield materials require simulation of the severe aerothermal environment that such components would encounter. Although wind tunnels are the most recognized type of aerodynamic ground test facility, they cannot adequately simulate the high-enthalpy, high-pressure environment needed to evaluate candidate reentry materials. Arc heaters, on the other hand, can provide the necessary pressure and thermal environments; however, the number of such facilities is rapidly diminishing. Most of the current Navy reentry heatshield and nosetip material testing is performed at the Arnold Engineering Development Center's Von Karman Facility High Enthalpy Aerothermal Test Unit (AEDC VKF HEAT). The arc facility has been utilized to evaluate candidate nosetip and heatshield materials, to evaluate the aging effects associated with heatshield life extension, and to develop instrumentation techniques for flight-test support.[1-3]

Introduction

As noted above, arc heaters are needed to simulate the proper pressure and thermal environments for the characterization and ground testing of reentry body nosetips and heatshields. The AEDC HEAT test units are the only state-of-the-art, high-pressure arc facilities in the world, providing high-enthalpy test conditions simulating aeroheating environments consistent with endoatmospheric flight at velocities from 5,000 ft/sec up to and exceeding 20,000 ft/sec. Test units include H-1, H-2, H-3, and H-R.

Description Of Test Facility

The AEDC HEAT-H1 Facility is a continuous-flow, electric arc-heated facility. It uses air as the working fluid and expands the flow to a supersonic free jet in the atmospheric environment of the test building. The arc heater is characterized by its segmented construction and fixed distance between electrodes. These features make it

possible for high-pressure, high-enthalpy operation. A schematic of the arc heater, configured for nosetip testing, is shown in Figure 1.

A rotary Model Positioning System (MPS), with eight positions, can be programmed to inject test models at various axial stations downstream of the expansion nozzle, advance or retract axially, expose models to the flow for various intervals of time, and hold the stagnation point of an ablating model at a fixed point in the flow. A maximum of seven models may be tested in one run, since one position is left vacant for heater start-up and shutdown.

There are several axisymmetric expansion nozzles that may be used to generate different Mach numbers and/or thermal environments. Contoured nozzles provide a single test environment for a given set of input conditions; nozzles currently available have a range in Mach number of 1.8 to 3.5. Flared nozzles provide an axially varying test environment for a given set of input conditions.

Due to the inherent nature of this type of arc heater, flow properties vary across the jet at any given axial station. Flow properties, such as the enthalpy, take on a "spiked" profile, with the maximum value occurring along the nozzle centerline. Enthalpy profiles may be "flattened" somewhat by adding cold mixing air to the hot jet and/or by installing a stilling chamber between the heater exit and the expansion nozzle. These "flattened" profiles provide a more uniform enthalpy distribution across the jet, at the penalty of reducing the maximum enthalpy at the centerline.

It is important to point out that arc facilities provide relative performance data and not

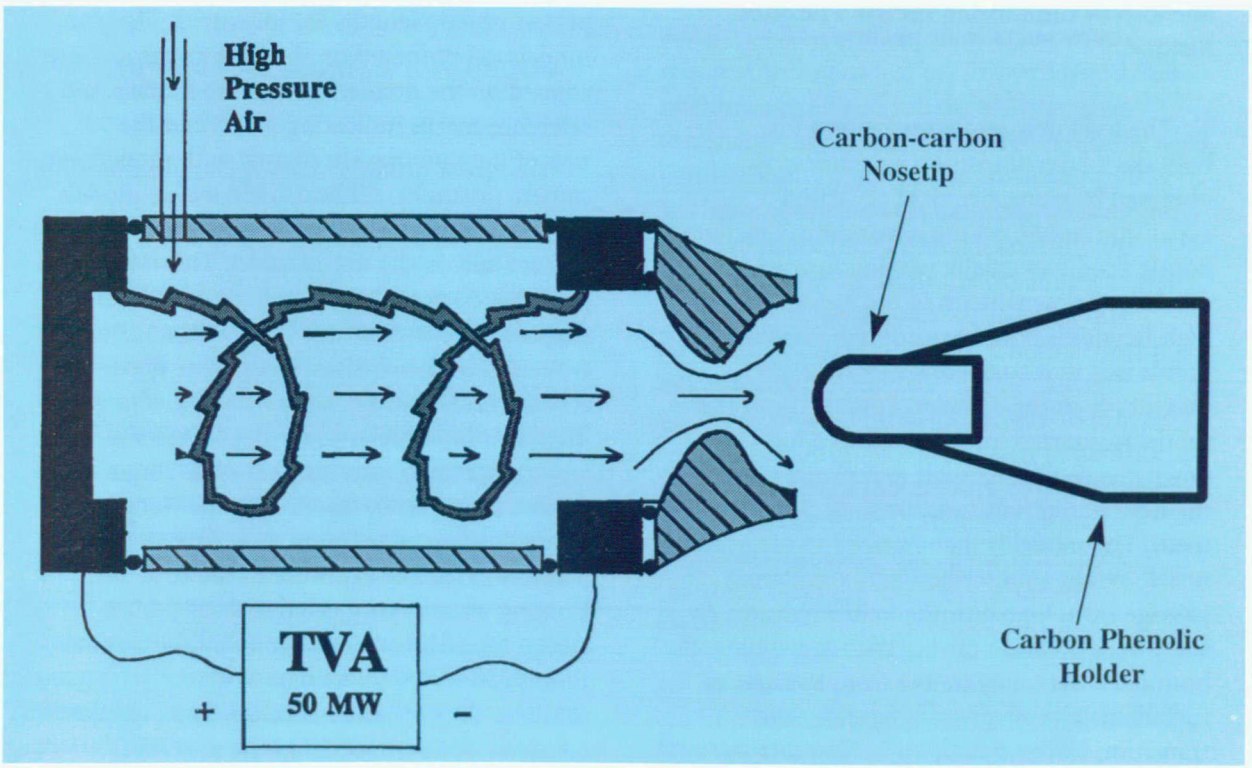

Figure 1—Schematic of Typical Arc Heater Operation, Configured For Nosetip Testing

absolute performance data. An arc does not produce a full-scale flight simulation; however, it is generally used to compare the performance of one material to another and/or to a reference material for which flight data exists. The arc is also invaluable for flight confidence testing.

Nose And Heatshield Material Test Types

Nosetip Material Testing—Arc heaters may be utilized to characterize stagnation point recession performance and to assess boundary-layer transition performance. Steady-state stagnation point recession testing is accomplished by using a contoured expansion nozzle and inserting the test model into the flow at a prescribed axial position downstream of the nozzle exit. As the stagnation point recedes, the MPS is moved forward to compensate, such that the stagnation point continually remains at the prescribed axial location. Recession data is obtained by viewing high-speed camera film and also by monitoring the MPS position history.

The test environment necessary for boundary-layer transition assessment is obtained by using a conical or "flared" expansion nozzle on the heater unit. The flared nozzle produces axially varying flowfield conditions downstream of the nozzle exit plane: high Reynolds Number and high pressure at the nozzle exit that continually decrease in magnitude in the downstream direction. The model is inserted into the flow at a location downstream of the nozzle exit plane, providing the desired high-altitude, laminar flow environment. The model is then ramped towards the nozzle exit at a prescribed rate, simulating passage from high altitude to low altitude. At some axial location during the ramp-phase, the boundary layer may transit from laminar to turbulent. The effects of boundary layer transition can be identified in film data by gouging that occurs on the nosetip model silhouette. The stagnation pressure and the Reynolds number where boundary layer transition is identified to occur, can be correlated to the axial position of the stagnation point relative to the nozzle exit.

Heatshield Material Testing—The arc heaters may be utilized to assess heatshield material ablation and insulation performance. Insulation performance can be obtained by fitting test samples with in-depth and/or backface thermocouples. Temporal ablation performance can be obtained by monitoring the test specimen surface topology with a Laser Wedge Recession system. A laser is projected onto the model surface 45° to the normal. As the surface recedes, the laser will appear to move equidistantly in the transverse direction along the test sample surface.

Test Procedures

Pretest—Before installing models in the test unit, model pretest photographs are taken, and pretest nosetip lengths are measured. The test models are mounted on the MPS stings and are aligned on the nozzle. For nosetip models, the reference marks indicating the 0° and the 90° rays of the nosetips are aligned with predefined camera positions. All heatshield wedge models are tested with the leading edge oriented horizontally in the test position. This is done primarily to accommodate data acquisition. Alignment of each wedge model depends on the type of model; two-sided wedges are generally tested with the wedge holder leading edge on the flow centerline in order to provide similar environments to each sample, while single-sided wedges are typically tested with the wedge holder leading edge below centerline to provide maximum surface exposure to the core flow. Cooling water is connected to each cooled wedge model, and thermocouple instrumentation is connected to the data system. Each sensor is then response checked. Final checks are made of the model alignment, model injection sequence, model instrumentation, data acquisition systems, motion picture camera setup, laser recession monitor, and arc heater systems.

Test—Nominal chamber pressures for nosetip transition test runs and heatshield runs range from 70 to 120 atm. Model injection sequences and runsheets are included for each test run. Nosetip transition models are generally injected downstream of the nozzle exit, preheated for a specified time, and then ramped forward at a prescribed rate until blockage of the laser beam near the nozzle exit occurs. Heatshield samples are injected and held at an axial station near the nozzle exit throughout the model exposure.

Posttest—At the completion of the programmed sequence, the arc heater is shut down. Water lines are disconnected, posttest resistance checks are made on the heatshield thermocouples, the models are removed, and posttest model photos are taken. The nosetips and heatshield samples are generally returned to NSWCDD via Southern Research, Inc., (SoRI) after posttest inspection and analysis.

NOSETIP AND HEATSHIELD EVALUATION

Evaluation Of Candidate Nosetip Materials

The arc heater has frequently been utilized for nosetip ablation performance evaluation and for nosetip boundary-layer transition onset characterization. Steady-state ablation runs may be made to assess the ablation performance of a given nosetip material or nosetip configuration at a constant pressure/altitude condition. Transition runs may also be made to evaluate the performance over a range of pressure/altitude conditions beginning with the low-pressure, high-altitude, laminar flow heating type of condition, and ramping up to the high-pressure, low-altitude, turbulent flow heating type of condition. Data acquired by the motion picture cameras, as well as the position history of the rotary injection system, may be used to quantitatively describe the recession performance and boundary-layer transition altitude.

Evaluation Of Aging Effects

The current requirements to provide the technology to maintain and extend reentry systems beyond their original design life have led to a need to better understand and to more accurately predict the effects of aging on various system components. This further translates into the need to maintain the minimum essential capability necessary to address aging phenomena and to meet the future requirements for in-service Submarine Launched Ballistic Missile (SLBM) reentry systems. For instance, the heatshield on the Mk4 reentry body is nearing the end of its originally scheduled life. Concern over the performance of the Mk4 heatshield materials beyond this life expectancy has led to the requirement to understand the effects of aging on heatshield sections; the arc heater provides a unique opportunity to explore these concerns.

Development of Curved Holders for Conical Sections—The evaluation of aging effects requires testing of tactical forward heatshield sections, since these are the only form of heatshield material that has been naturally aged. Until recently, much of the arc heater testing has been performed on flat material samples; however, since the heatshield sections are conical, a need arose for the capability to test curved material samples. To support this requirement, AEDC and the Thermal Technologies Incorporated (TTI) developed and recently evaluated a curved holder to test conical sections in the arc heater. In addition to this test holder, a curved-surface calorimeter probe was developed and tested to provide flowfield definition and characterization. A sketch of this type of holder is shown in Figure 2.

Development of In-Depth Thermocouple Instrumentation—To facilitate better understanding of material performance, various embedded thermocouple techniques have been developed, and their performance and integrity have been tested in the arcs. Thermocouple

techniques included "woven in place," "flight-test heatshield plugs," "Modified TTI plug," and "across-ply plugs." Most of these concepts, including backface thermocouples, have been shown to perform well in the arcs.

Connection To Navy Textron Data Base

The closing of the Textron facility eliminated the ability to properly simulate the effects of char formation on heatshield sections. This facility allowed the formation of a layer of char on the exposed face of a heatshield sample, simulating an integrated flight heating distribution. AEDC recently developed and evaluated a variable-pitch wedge technique to recover this critical heatshield test capability previously available only at Textron.

The technique, as shown in Figure 3, involves introducing the model downstream of the nozzle, below centerline, at a negative angle of attack to simulate the laminar heating environment at high altitudes. To transition to the low-altitude environment, the model is simultaneously ramped forward, raised toward the centerline, and pitched to a larger positive angle of attack.

At this time, the thermal and mechanical designs have been evaluated. The Textron test environment conditions have been reproduced, as proven by calorimeter measurements at both the laminar (or low-heating-rate) position and the high-heating-rate position. This capability is necessary to fully understand char effects on aging of heatshields and on new material candidates.

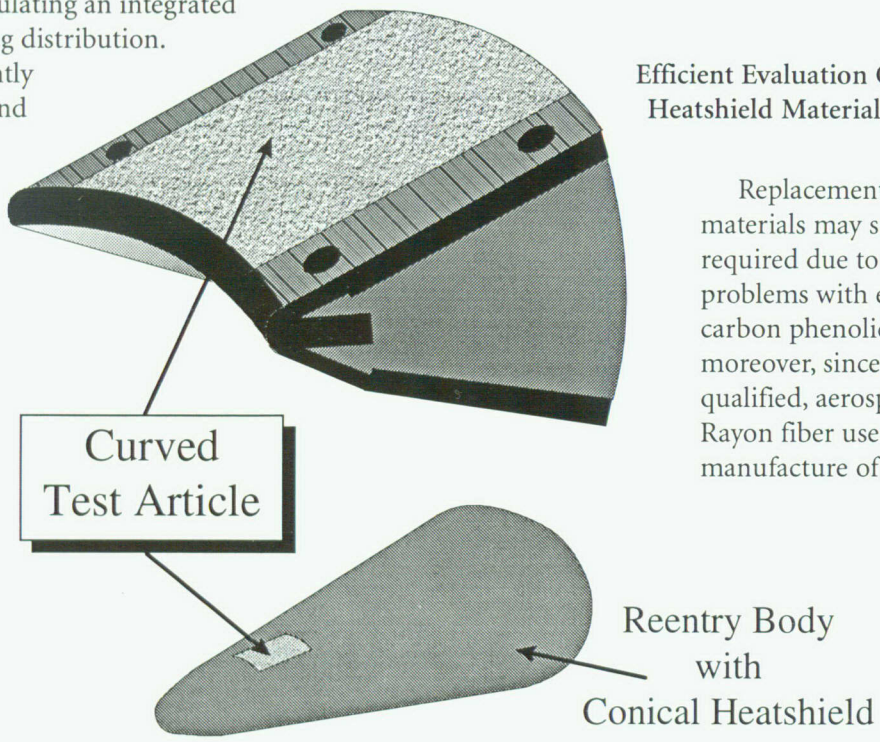

Figure 2—Curved-Holder for Testing Conical Heatshield Sections

Efficient Evaluation Of New Heatshield Material Candidates

Replacement heatshield materials may soon be required due to age-related problems with existing carbon phenolic heatshields; moreover, since the qualified, aerospace-grade Rayon fiber used in the manufacture of existing heatshields is no longer available, a new carbon phenolic material must be developed and tested.

The efficient evaluation of new material candidates requires the testing of multiple samples to characterize variations in material response and to assess facility repeatability. Until recently, the arc test capability was limited to one single-sided wedge holder per sting

position. This greatly limited the number of samples that could be investigated. In response to the need to test multiple samples efficiently, AEDC and TTI developed a double-wedge holder. Figure 4 shows both the typical single-sided wedge holder and the new double-wedge holder concept. A new dwell calorimeter was developed to compare and characterize the flowfield on-centerline and off-centerline. It has been proven that the arc flowfield has good symmetry and, therefore, that both sides of the double-wedge holder will be exposed to the same conditions. This technique greatly reduces the cost and total run time when evaluating new material candidates.

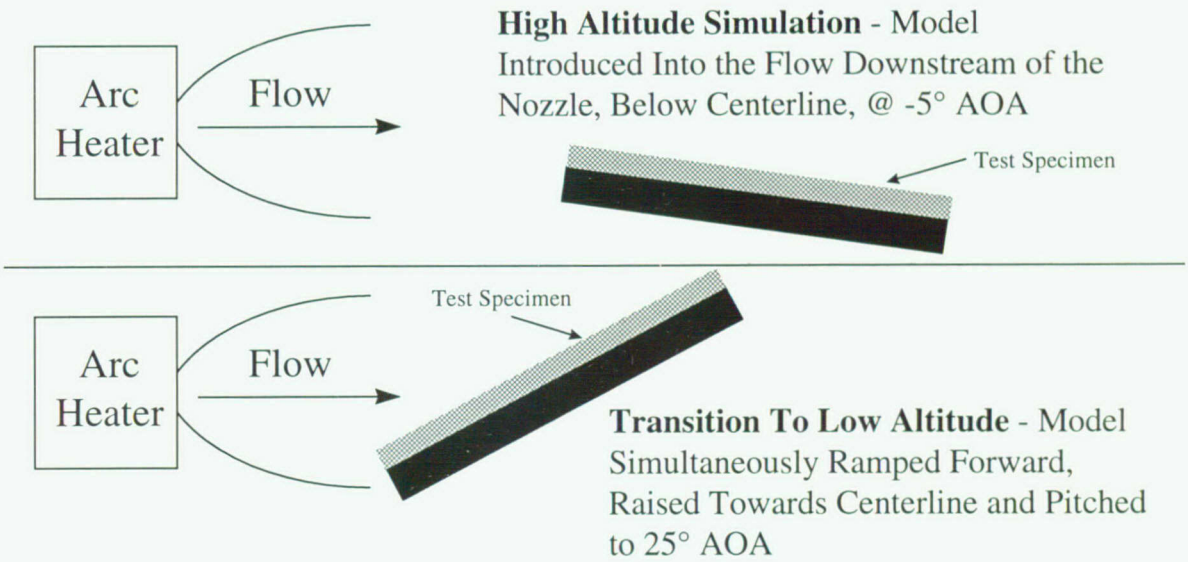

Figure 3—AEDC Variable-Pitch Wedge Technique

Flight Test Support

Flight test instrumentation requires robust design to survive the severe flight-test environment. The arc facility provides a timely, affordable opportunity to develop and evaluate instrumentation concepts prior to flight testing. Recent experiments have included the development and evaluation of heatshield ablation detectors and heatshield recession gauges. Heatshield ablation detectors monitor recession on a flight-test vehicle heatshield when embedded detector materials are activated upon exposure to the flow. During the arc test, a laser grid was utilized to assess the surface thickness at activation time of the embedded detector materials, thereby calibrating the technique. Also, recent arc tests were conducted to assess the effect of embedded wire thickness on localized heatshield ablation to provide data to optimize the design of heatshield recession gauges.

SUMMARY

The arc facility has been utilized to evaluate candidate nosetip and heatshield materials, to evaluate the aging effects associated with heatshield life extension, and to develop instrumentation techniques for flight-test support. For example, boundary-layer transition onset characterization for various nosetip materials has been conducted in the arc facility. An efficient evaluation of new material candidates for heatshields has recently been demonstrated through the use of double-sided wedge holders for the arc's rotary injection system. Flight instrumentation requires robust

design to survive severe flight-test environments, and the arc facility provides timely and affordable opportunities to develop and evaluate instrumentation concepts prior to flight testing. The evaluation of aging effects requires the testing of tactical forward heatshield sections (conical/curved) and the development of more accurate instrumentation techniques. The development and evaluation of curved holders for conical sections and in-depth thermocouple instrumentation has recently been conducted in the arc facility. A development effort is underway to relate the Navy Textron Data Base previously established at the Textron facility with a new variable-pitch wedge concept in the AEDC facility. The closing of the Textron facility eliminated the ability to properly simulate the effects of char formation on reentry heatshields. The new capability at AEDC is critical to maintaining this testing technique and providing a connection to the previous data base.

REFERENCES

1. Horn, D.D. and Smith, R.T., *AEDC High-Enthalpy Ablation Test (HEAT) Facility Description, Development, and Calibration*, AEDC-TR-81-10, Jul 1981.
2. Test Facilities Handbook (Thirteenth Edition), *Von Karman Gas Dynamics Facility, Vol. 3*, Arnold Engineering Development Center, Arnold Air Force Base, Tennessee, May 1992.
3. Smith, D.M. and White, R.L., *BMO Peacekeeper Nosetip Transition Test in the HEAT-H1 Test Unit*, AEDC-TSR-91-V31, Feb 1992.

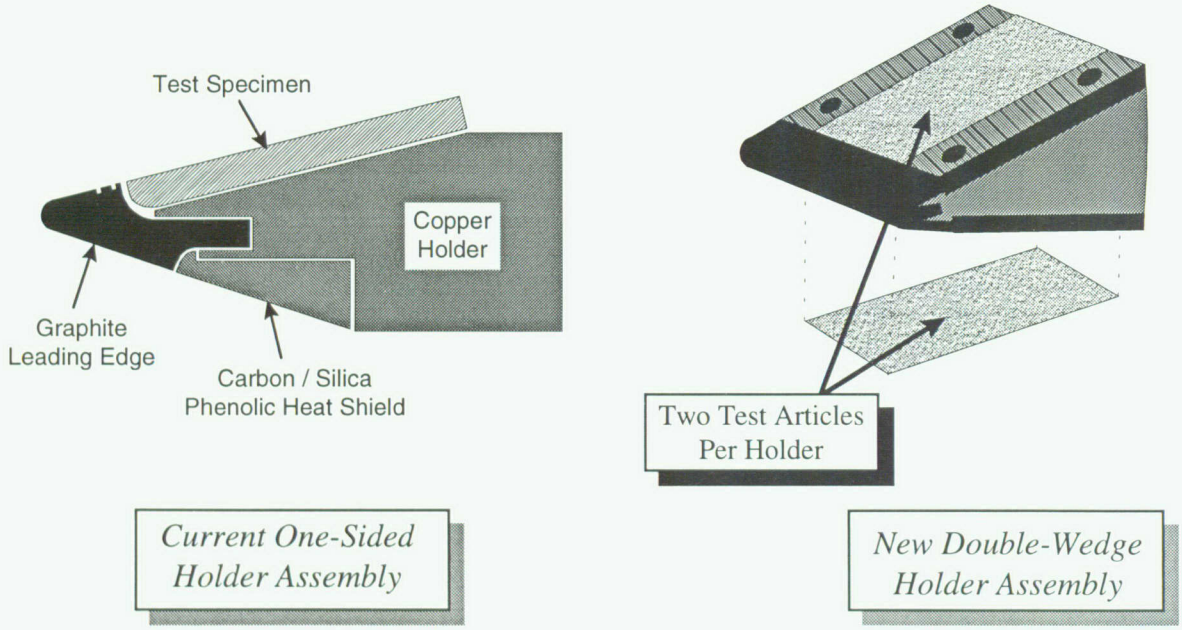

Figure 4—Typical One-Sided Holder and New Double-Wedge Holder

THE AUTHORS

MR. MICHAEL J. GILLUM

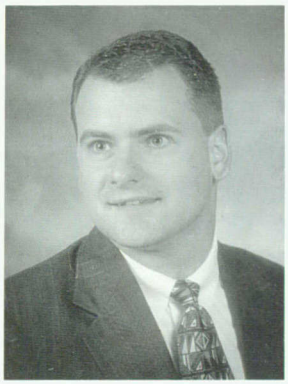

MR. MICHAEL J. GILLUM is an aerospace engineer in the Reentry Systems Branch of the Strategic & Strike Warfare Department. He has been involved with the high-temperature aspects of hypersonic flow, reentry technology development, ground testing, and reentry systems engineering, working in the Aerothermal Analysis Group for the past eight years. He holds a B.S. and an M.S. in aerospace engineering from the University of Maryland at College Park. He is currently seeking a Ph.D. in aerospace at the University of Maryland. He is a student member of the American Institute of Aeronautics and Astronautics.

DR. LEO P. O'HARE

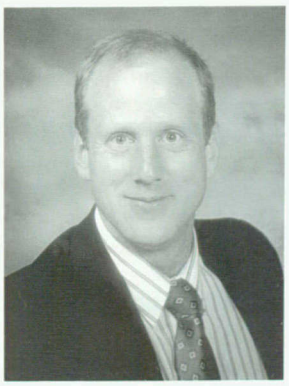

DR. LEO P. O'HARE is an aerospace engineer in the Reentry Systems Branch of the Strategic & Strike Warfare Department. He has been involved in reentry system technology development, ground testing, advanced material development, and plasma dynamics. He holds a B.S., M.S., and a Ph.D. in aerospace engineering from the University of Maryland at College Park. He is also a member of the American Institute of Aeronautics and Astronautics.

Moving Mass Roll Control For Fixed-Trim Reentry Bodies

Mr. Frank J. Regan

Future missions for atmospheric reentry bodies (RBs) will place emphasis on altering the trajectory or redirecting the velocity vector during the terminal (reentry) phase of the flight. With a built-in asymmetry, lift is developed continuously normal to the velocity vector. There must be some provision to roll the body and thereby direct (or redirect) the lift vector. Because of the high thermal environment, aerodynamic controls will encounter conditions of severe heat transfer. External thrusters also have the disadvantage of requiring internal storage of a chemical propellant. An attractive alternative is the Moving Mass Roll Control System (MMRCS).

The MMRCS controls the roll attitude of a lifting RB by moving a mass laterally to offset the center of mass of the RB from the configurational plane of symmetry. Since the controller remains entirely within the aero shell, it is impervious to aerodynamic or thermal loads. This study includes the analysis of a roll autopilot. A roll angle, commanded by the guidance algorithm, is compared to the actual roll angle, and the difference (error signal) is sent to the controller. The controller then calculates the appropriate lateral position of the moving mass. A second-order lag is used to model the response characteristics of the controller.

The ability of the linear MMRCS roll autopilot to control the highly coupled nonlinear plant (RB) during a typical mission profile is demonstrated using a nonlinear simulation of the full seven degree of freedom (7-DOF) governing equations of motion. The moving mass roll control (MMRC) appears to be a relatively simple and effective method of modulating the roll angle of a lifting RB, especially to meet precision requirements against a target without an active defense.

Background

If we examine the whole range of atmospheric vehicles from light airplanes and helicopters through high-performance aircraft and even RBs, we find that there is a commonality in the principle of vehicle control. All such vehicles develop an aerodynamic pressure field whose distribution is altered in some manner to achieve a desired control force. For convenience, this pressure field is integrated into two

components—lift and drag. Drag is the component of the aerodynamic force in the direction of the oncoming velocity vector, and lift is the orthogonal component.

The centroid of this pressure field (first moment) defines the location of the center of pressure. Vehicle control is effected by moving the center of pressure away from the center of mass. The resulting moment then rotates the vehicle in some preferential direction. The same control function can be achieved by moving the center of mass rather than the center of pressure. While movement of the control mass moves the center of mass, it has no effect upon the location of the center of pressure. However, the change in body attitude resulting from center-of-mass offset will cause the pressure distribution to proportionally change. The center of pressure will also move to the new center of mass.

Figures 1 and 2 illustrate two generalized aerospace vehicles. In Figure 1, a pitching moment is generated by deflecting the elevator, causing a rearward movement of the center of pressure. Since the center of mass has not moved, the moment arm $\underline{r}_m$ causes a negative (nose-down) pitching moment about the y-axis. The alternative method of generating the identical pitching moment (shown in Figure 2) is to move the center of mass. In both cases, the aerodynamic moment will cause an angular displacement. When the vehicle (with either control system) reaches an angle at which the centers of pressure and mass coincide, the vehicle will have reached a trim condition (zero moment) at a new angle of attack.

In Figure 2, the movement of the control mass from null at the vehicle's center of mass results in a change in angle of attack proportional to the offset of the center of mass from the center of pressure. Since the output (angle of attack) is proportional to the input (movement of the control mass), the controller is called a *proportional* controller.

If the control mass is moved in the direction of the positive body-fixed x-axis through a distance $\underline{r}_c$, the center of mass moves through a distance $\underline{r}_c$. If M is the mass of the vehicle exclusive of the control mass, we may define the distance $\underline{r}_m$ as

$$\begin{aligned} \underline{r}_m \sum m_i &= \sum \underline{r}_i m_i \\ \underline{r}_m [M + m_c] &= \sum \underline{r}_i m_i + \underline{r}_c m_c \end{aligned} \qquad (1)$$

where the first summation on the right is over the whole vehicle, exclusive of the control mass. Since the origin of the body-fixed frame is at the center of mass, the first term on the right vanishes. Thus, we may rewrite Equation (1) to express the vehicle mass-offset vector $\underline{r}_m$ as

$$\underline{r}_m = \frac{m_c \underline{r}_c}{(M + m_c)} = \left(\frac{\mu}{M}\right) \underline{r}_c \qquad (2)$$

where

$$\mu = \frac{m_c M}{(M + m_c)} = \frac{m_c}{1 + \frac{m_c}{M}} \quad \text{or} \quad \frac{\mu}{M} = \frac{\frac{m_c}{M}}{1 + \frac{m_c}{M}}$$

The parameter μ is called the *reduced mass*, and it has the same physical units as mass. For most controllers, $m_c << M$, which leads to the approximation $\mu/M \approx m_c/M$ or the mass ratio.

Equation (2) shows that the constant of proportionality (gain) between the control movement $\underline{r}_c$ and the center-of-mass movement $\underline{r}_m$ is the mass ratio m_c/M. If L is body length r_m/L for an aircraft, is as large as 0.05. For an RB, on the other hand, r_m/L is around 0.005. With a mass ratio of 1/30 (a 10-lb control mass in a 300-lb RB), this requires an r_c/L of 0.15, or the mass must be moved about 15 percent of the body length. Even though this distance appears "reasonable," it may not always be practical in an RB with severe packaging constraints. A trade-off is then required to

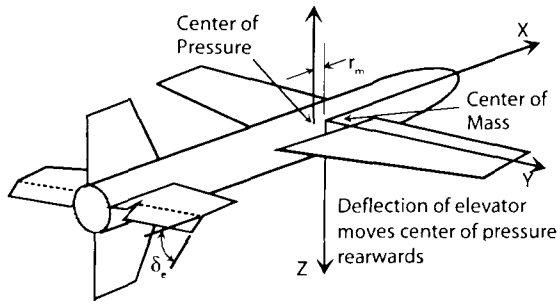

Figure 1—Control Through Configuration Change

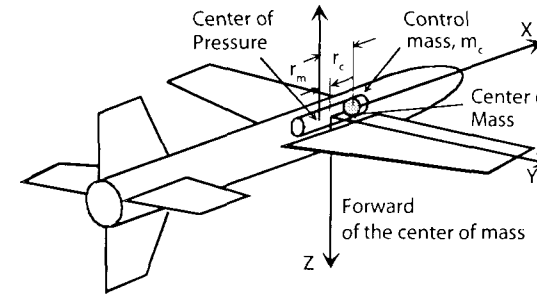

Figure 2—Control Through Movement of Center of Mass

increase the moving mass to minimize its travel within the body.

The moving mass need not be ballast since some mass may be a functional part of the RB. For example, a battery operating the Inertial Measurement Unit (IMU) should not be affected by the rapid motion that might be required as part of the control mass. In this article, we will limit our interests to roll control. We will assume that sufficient static margin exists for the passive aerodynamics to maintain stability. The control mass will move at a right angle to the axis or plane of symmetry.

INTRODUCTION

Let's now concentrate on vehicles that are good candidates for a moving mass control: the axisymmetric vehicle and the fixed-trim vehicle. The axisymmetric vehicle essentially has rotational symmetry about an axis. It is assumed that the mass distribution places the center of mass on this axis of symmetry (centerline) and ahead of the center of pressure. With the center of mass ahead of the center of pressure, the vehicle is stable and, without disturbances, will fly a ballistic trajectory (drag only). A control mass moving laterally will offset the center of mass from the configurational axis of symmetry. The result is that under trim conditions the net aerodynamic force must pass through both the centers of mass and pressure. Figure 3(a) shows that a lateral force develops as a result of the movement of the control mass. This force is then available for making small changes to the trajectory.

In Figure 3(b) we have designated a- and b-axis systems. The a-axis has its origin at the center of mass of the vehicle when the control mass is at null; the vehicle's plane of symmetry is coincident with the xz plane. The a-axis is useful for bringing the aerodynamic forces and moments into the simulation. Movement of the control mass off-null defines the b-axis. The b-axis originates at the instantaneous center of mass and is parallel to the a-axis. Note that we have changed the vectors locating the center of mass from null from $\underline{r}_m$ to $\underline{r}_{b/a}$ (b-frame relative to a-frame) and the location of the control mass from the origin of the a-frame from $\underline{r}_c$ to $\underline{r}_{c/a}$. The vectors $\underline{r}_{c/b}$ and $\underline{r}_{b/a}$ are obvious. In any practical application, the tube containing the control mass (shown in Figure 3(b)) must rotate relative to the body in order to direct the lift force.

It might be of some interest to determine the level of side loads that a typical moving mass controller is capable of developing. First, assume that the moment (in coefficient form) may be written as

$$C_n = C_{no} + \left[\left. \frac{dC_m}{d\alpha} \right|_{\beta=0} \beta_T \right] = 0 \qquad (3)$$

Since we are assuming a trim condition, we have set the moment equal to zero. The trim sideslip angle β_T may be written as

$$\beta_T = -\left[\frac{C_{no}}{\left(\frac{dC_m}{d\alpha}\right)}\right] = -\left[\frac{C_{no}}{C_{m\alpha}}\right] \qquad (4)$$

Because we are moving the control mass along the y-axis, we will generate a side force and a yawing moment C_n. For simplicity, we will assume that $dC_n/d\beta = dC_m/d\alpha = C_{m\alpha}$.

By definition, C_{no} is the moment that exists at zero sideslip angle. From Figure 3(a) it is obvious that C_{no} is the product of drag times the center-of-mass offset:

$$C_{no} = C_{Do}\left(\frac{r_m}{L}\right) \qquad (5)$$

where L is the reference length (body length), and C_{Do} is the zero-lift drag coefficient. The moment derivative, $dC_m/d\alpha$, is the static margin times the normal force derivative as

$$\frac{dC_m}{d\alpha} = C_{m\alpha} = \frac{f}{L}\frac{dC_N}{d\alpha} = \frac{f}{L}C_{N\alpha} \qquad (6)$$

where $dC_N/d\alpha$ is the change in normal force with angle of attack.

Inserting Equations (5) and (6) into Equation (4) gives for the sideslip angle at trim β_T:

$$\beta_T = \left(\frac{C_{Do}}{C_{N\alpha}}\right)\left(\frac{r_m/L}{f/L}\right) \qquad (7)$$

We can now compute a typical trim sideslip angle for a symmetric RB taking the following numerical values as typical:

$C_{Do} = 0.10 \quad dC_N/d\alpha = 1.5$ /rad

$r_m/L = 0.0020 \quad f/L = 0.010$

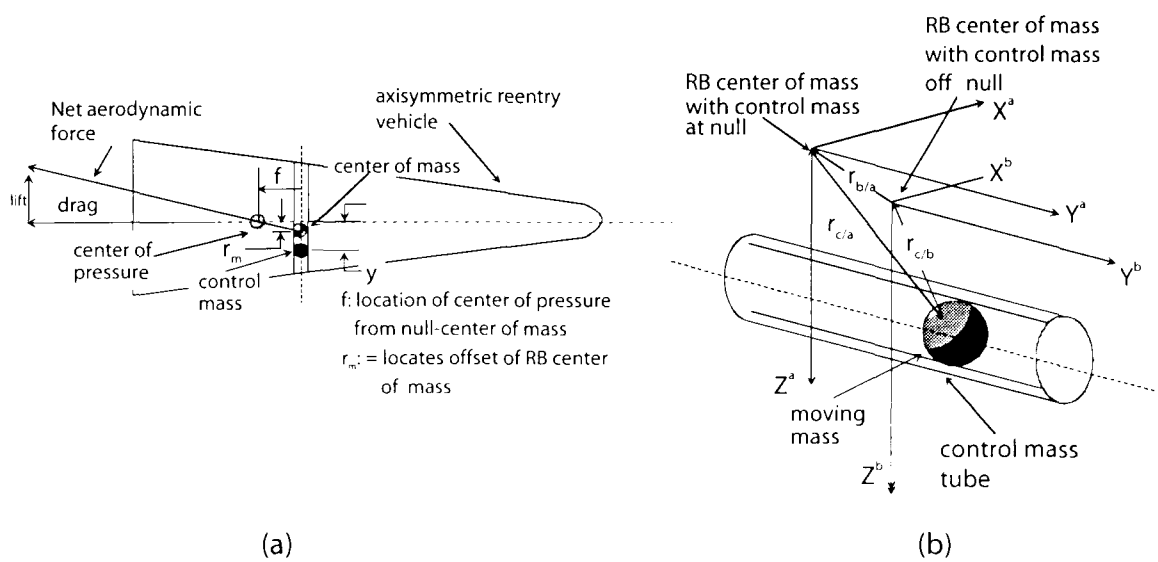

Figure 3—Movement of Control Mass to Offset the Reentry Body's Center of Mass

The trim angle of attack then is

$$\beta_T = \left(\frac{0.1}{1.5}\right)\left(\frac{0.002}{0.010}\right) = 0.0133\,\text{rad} = 0.76\,\text{deg}$$

From Equation (7), it is obvious that the lateral force (in coefficient form) is given as

$$C_y \approx -C_{Do}\left(\frac{r_m/L}{f/L}\right) = -C_{Do}\left(\frac{r_m}{f}\right) \qquad (8)$$

Equation (8) clearly points out the classical compromise between maneuverability and stability. A large value of f indicates a large static margin and, hence, large directional stability. However, a large value of f also means a small value of lateral or maneuvering force. Reducing the static margin f reduces static stability but gives a large value of side force and, hence, maneuverability. Thus, the relative presence of maneuverability and stability is determined by the ratio of r_m/f. If static stability is fixed at some lower bound, then maneuverability is set by r_m which, in turn (according to Equation (2)), requires either a large control mass ratio m_c/M, a large range of motion ("stroke") r_c, or both.

If we assume a drag polar to account for drag change with angle of attack (or lift coefficient), we get

$$\frac{C_y}{2C_{Do}} \approx \left.\frac{C_L}{C_D}\right|_{max} = \left(\frac{r_m}{f}\right) \qquad (9)$$

Note the drag polar requires that the drag coefficient at maximum lift-to-drag ratio be twice that of the zero-lift drag coefficient. The maximum lift-to-drag ratio—as well as C_{Do}, the drag coefficient at zero angle of attack—is determined solely by the configuration or shape of the vehicle (and the flow environment). Equation (9) provides a relationship that sets the center-of-mass offset from the axis of symmetry required to achieve the maximum lift-to-drag ratio. As shown in Equation (2), a given value of mass-offset, r_m, requires positioning the moving mass with a mass ratio, μ/M, at a distance, r_c. For a conical body, the maximum lift-to-drag ratio is something between 1.5 and 1.9.

The preceding discussion was concerned with the axisymmetric RB with a moving mass, whose tube must be rotated relative to the body to change the direction of the lift force. In Figure 4, the moment balance is shown. Assuming that the control mass moves along the y-axis, the offset center of mass is also along the y-axis. The angle-of-attack plane is contained in the xy plane, so the moment vectors are normal to this plane, i.e., parallel to the z-axis. Note the presence of the restoring moment $(dC_m/d\alpha)\beta_T = (f/L)(dC_N/d\alpha)\beta_T$, according to Equation (6), and the asymmetry moment $C_{no} = C_{Do}(r_m/L)$. Both of these moments are antiparallel and have equal magnitudes at the trim sideslip angle.

The fixed-trim vehicle is illustrated in Figure 5. Two convenient methods for developing fixed trim is either to bend the nose or to cut out a portion of the base. Within the definition of fixed trim is the variable-trim vehicle. Fixed trim here is taken to mean an alteration to the otherwise symmetric configuration to enable the vehicle to trim at a nonzero angle of attack. With a fixed-trim RB, the moving mass is used to control the direction of the lift that is generated by the configurational asymmetry. In the axisymmetric vehicle, location of the control mass off the axis of symmetry generates a side force; the tube must then rotate relative to the body to give direction to this lift. In the fixed-trim vehicle, the moving mass tube could be fixed to the vehicle. The control mass is moved along the tube, offsetting the vehicle's center of mass and generating a rolling moment. By rolling the vehicle, the lift force is given a preferred direction. In brief, the moving mass control in an axisymmetric vehicle gives a skid-to-turn maneuver in a

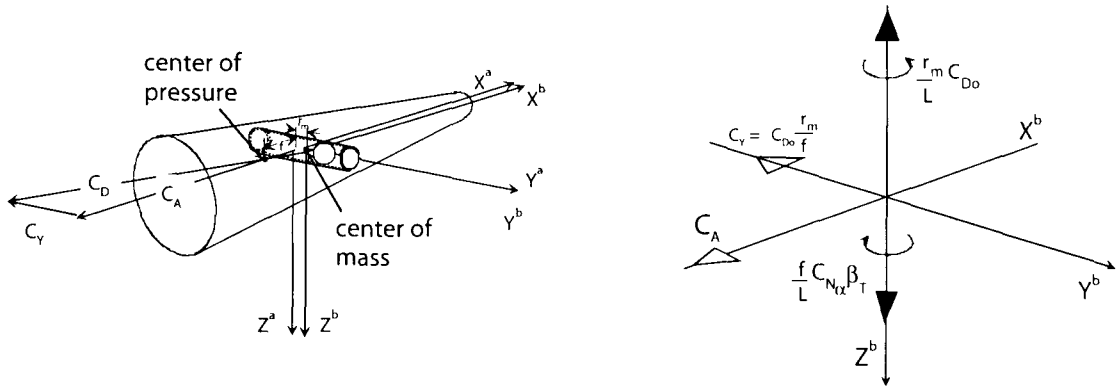

Figure 4—Forces on an Axisymmetric Vehicle with a Moving Mass Controller

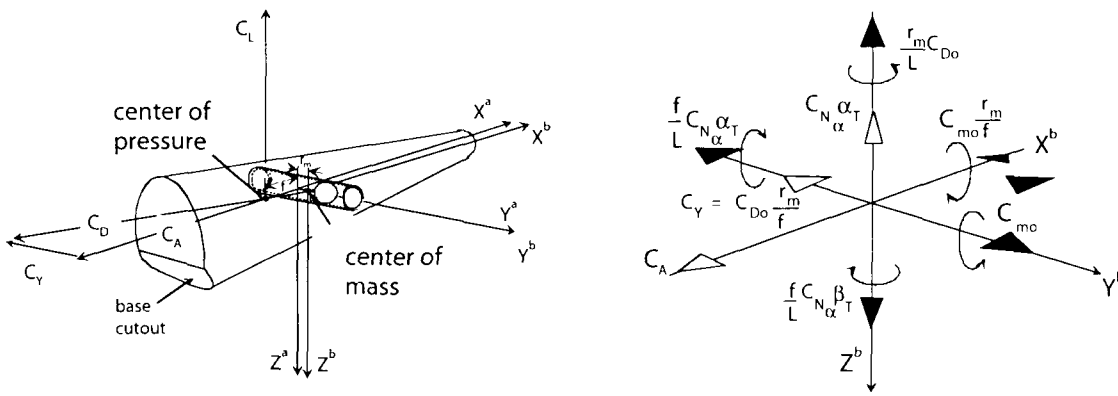

Figure 5—Forces on a Fixed-Trim Vehicle with a Moving Mass Controller

direction opposite to that of the movement of the control mass. On the other hand, in the fixed-trim vehicle, the movement of the control mass gives a bank-to-turn in the direction of the control mass movement.

For the axisymmetric vehicle, we may summarize the aerodynamic force and moment loads as

$$C_y = C_{N\alpha} \beta_T \qquad (10)$$

$$C_n = 0 = C_{Do} \frac{r_m}{L} + C_{N\alpha} \frac{f}{L} \beta_T \qquad (11)$$

Equations (10) and (11) follow immediately from Equations (3) through (6) and are repeated because of their equal applicability to the fixed-trim vehicle. Figure 4 shows the forces and moments acting on the axisymmetric vehicle. The aerodynamic loads are axial C_A along the negative x-axis and transverse along the negative y-axis. The aerodynamic moment constituents are along the z-axis; because of the trim condition, these constituents are of equal magnitude but opposite direction. Forces are shown with the open arrow, and moments are shown with the solid arrow.

The fixed-trim vehicle has pitching and rolling moments as well as a yawing moment. Because of the base cutout, the vehicle will trim (zero moment) at an angle of attack α_T. We may

sum the pitching moments and equate to zero to give

$$C_m = 0 = -C_{N\alpha}\frac{f}{L}\alpha_T + C_{mo} \qquad (12)$$

and the corresponding normal force

$$C_N = C_{N\alpha}\alpha_T \qquad (13)$$

Obviously, we can solve for the normal force as

$$C_N = \frac{C_{mo}}{(f/L)} \qquad (14)$$

The term C_{mo}, sometimes called the *camber*, quantifies the magnitude of the cutout or the nose bend (or whatever asymmetry is used to trim at a nonzero angle of attack). If the vehicle were oriented relative to the flow such that there is no normal force, i.e., $C_N = 0$, then the existing moment would be C_{mo}.

With the tube containing the control mass directed along the y-axis, there will be a rolling moment C_l about the x-axis equal to

$$C_l = C_{N\alpha}\frac{r_m}{L}\alpha_T \qquad (15)$$

$$C_l = \left(\frac{r_m/L}{f/L}\right)C_{mo} = \left(\frac{\mu}{M}\right)\left(\frac{r_c}{L}\right)\left(\frac{1}{f/L}\right)C_{mo} \qquad (16)$$

In addition, the side force C_y and moment given in Equations (10) and (11) also are present in the fixed-trim vehicle. Figure 5 illustrates a fixed-trim vehicle; the adjacent figure indicates the applied forces (open arrows) and moments (solid arrows).

The force and moment diagram in Figure 5 allows us to summarize the control problems of the fixed-trim vehicle. Note that the fixed-trim RB has three forces: the axial force along the negative x-axis, the negative y-force caused by the mass-offset, and the normal force along the negative z-axis caused by the camber or the nonzero trim angle. We have assumed that moments about the y- and z-axes always sum to zero (trim condition); only the moment about the x-axis (the rolling moment) is unbalanced.

With a built-in, fixed-trim angle of attack, a lift force acts on the vehicle at all times (unless some provision is made for varying this asymmetry). Moving the control mass rolls the body to direct this "built-in" force. Bringing the control mass to null will stop the roll angle. Because there is virtually no roll-damping, the roll acceleration is $d^2\phi/dt^2$ and is proportional to r_c, the position of the control mass. Thus the roll angle is proportional to the second integral of the position of the control mass as

$$\phi \approx -\frac{\mu}{M}\frac{1}{f}C_{mo}\int\int r_c\,d\tau dt \qquad (17)$$

Assume that the vehicle has banked to an angle ϕ by the movement of the control mass to the right (positive). The net horizontal force is in coefficient form

$$C_y = C_{N\alpha}\alpha_T\sin\phi - C_{Do}\frac{r_m}{f}\cos\phi$$

$$\approx \phi\alpha_T C_{N\alpha} - C_{Do}\frac{r_m}{f}$$

Assume that α_T is 1/6 radian and that the bank angle is also 1/6 radian. Inserting the numerical values given following Equation (7) into Equation (18), we have

$$C_y = \left(\frac{1}{6}\right)\left(\frac{1}{6}\right)(1.5) - 0.01\left(\frac{0.0020}{0.010}\right) = 0.0217$$

Table 1—Geometry and Mass Properties of Reentry Body

Description	Value	Units
Cone half-angle	8.0	degrees
Base radius	10.8	inches
Nose radius	1.9	inches
Length	66.0	inches
Weight (Mass)	400 (12.4)	lbs (slugs)
Cont. Weight Mass	10 (0.31)	lbs (slugs)
Roll Inertia	1.8	slug-ft^2

So, with sufficient bank angle and camber moment C_{mo} (or trim angle of attack α_T), there is a net force to the right. However, we must recognize that because of the variation of roll angle with the double integral of control mass position (Equation (17)), for small initial movement of the control mass, the vehicle will act like an axisymmetric vehicle. and a motion of the control mass to the right will cause the nose to move to the left and generate a force to the left. As the roll angle rapidly develops (again due to the double integral variation of roll angle with time), the vehicle will bank to the right and have a force to the right.

REENTRY BODY (RB) DESIGN

The RB is an 8-degree sphere-cone with a bluntness ratio of 0.175. A base cut parallel to the centerline generates a trim angle of 6.1 degrees with a corresponding lift-to-drag ratio of 1.7. The geometry and mass properties are given in Table 1. For the details of the RB and the control system design/analysis, the reader should consult Reference 1.

The vehicle's aerodynamic properties were generated using the Supersonic-Hypersonic Arbitrary Body Program (SHAB).[2]

In Figure 3, we defined the a- and b-axis systems. The xz plane of the a-frame contains the plane of symmetry of the RB. The origin of the a-frame is at the center of mass of the RB when the control mass is at null. The b-axes are parallel to those of the a-frame, but the origin is at the instantaneous center of mass. Let $\underline{r}_{c/a}$ and $d\underline{v}_{c/a}/dt$ be the (measurable) position and acceleration vectors of the control mass relative to the reference or a-frame. It can be shown that there is a reaction moment contribution given as

$$\underline{M}_c = -\mu \underline{r}_{c/a} \frac{d\underline{v}_{c/a}}{dt} \tag{18}$$

where μ is the reduced mass parameter. Obviously, if the control mass tube passes through the RB's center of mass, i.e., if $\underline{r}_{c/a}$ and $d\underline{v}_{c/a}/dt$ are colinear, $\underline{M}_c$ would be identically zero. However, if the mass tube is below and behind the RB's center of mass, $\underline{M}_c$ is positive and helps yaw the nose to the right. Movement of the control mass to the right rolls the RB to the right. The reaction moment given in Equation (18) mitigates much or all of the adverse yaw discussed earlier.

The roll equations must be simplified to form the basis for an autopilot design. Linearization of the roll equation results in the following second-order differential equation:

$$\frac{d^2\phi}{dt^2} + \omega_R \frac{d\phi}{dt} = Kr_m \qquad (19)$$

where ϕ is the roll angle, r_m is the position of the control mass, and ω_R and K are the roll-rate damping and the mass effectiveness parameters given, respectively, as

$$K = \mu q_\infty \left(\frac{SC_N}{I_X}\right) \approx \frac{m_c}{M} q_\infty \left(\frac{SC_N}{I_X}\right) \qquad (20)$$

$$\omega_R = \frac{C_{lp} d^2 q_\infty S}{I_x V_\infty} \qquad (21)$$

In Equations (19) and (20), m_c/M is the mass ratio, q_∞ is the dynamic pressure, C_N is the normal force coefficient at trim, and S and I_Y are the reference area and roll moment of inertia. C_{lp} is the roll-damping derivative, and V_∞ is the free stream velocity magnitude. The roll damping parameter ω_R is of secondary importance since the roll damping is very small.

The mass-effectiveness parameter K is the governing design parameter. K is a measure of the angular roll acceleration produced per unit of control mass displacement. The parameter K contains the key RB design variables and environmental conditions affecting roll performance. Obviously, roll response is enhanced by increasing the RB mass fraction m_c/M and the normal force coefficient C_N at trim. Decreasing the RB's axial moment of inertia I_x also increases roll response. Equation (20) also indicates that an MMRC is more responsive at higher values of dynamic pressure.

Initial sizing of K showed that a 10-lb moving mass control with a one-inch stroke was sufficient to provide roll response for the 400-lb Maneuvering Reentry Body (MaRB). The stroke was kept small along with the average actuator slew rates to keep to a minimum the weight, volume, and power requirements of the control system.

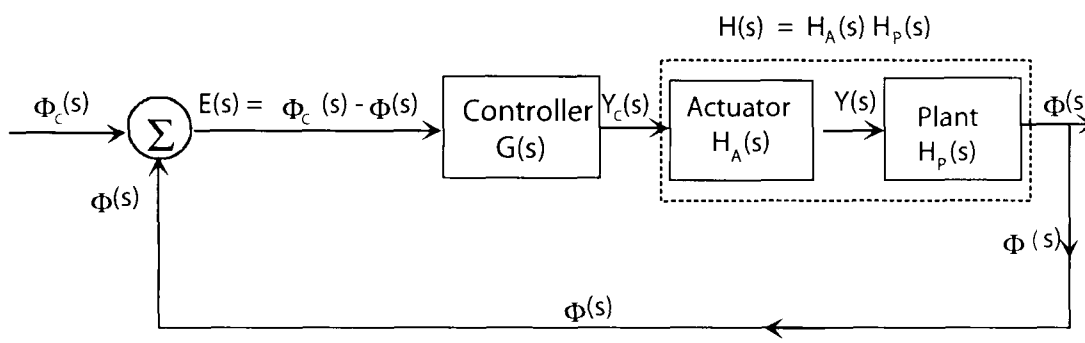

Figure 6—Block Diagram of Roll Autopilot

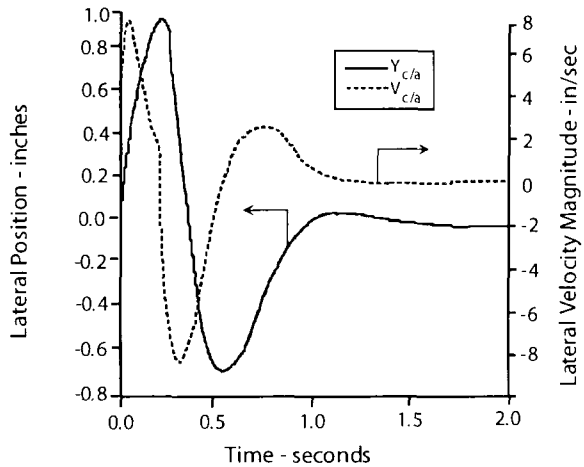

Figure 7—Lateral Position and Speed of Control Mass vs. Time (design point)

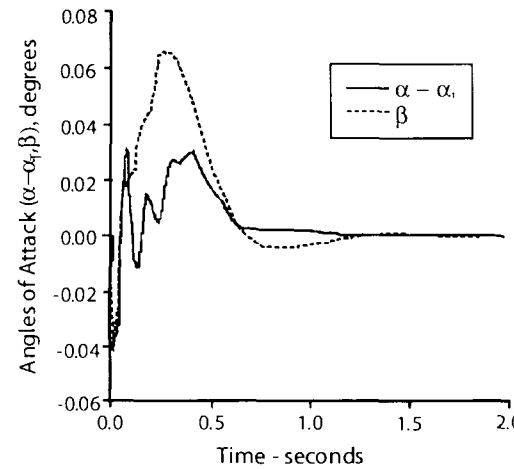

Figure 8—Disturbance Angle of Attack and Sideslip vs. Time (design point)

ROLL AUTOPILOT

Figure 6 shows a simplified block diagram of the linear roll autopilot. A roll angle is commanded by the guidance algorithm. This roll angle is then compared to the actual roll angle, generating an error signal E(s). This error E(s) is then sent to the controller. The controller calculates a commanded lateral position of the control mass. Position and speed of the control mass are always with reference to the a-frame.

To account for controller lag, the commanded position of the control mass y_c goes through the actuator, represented as a second-order system. The characteristic parameters of this actuator are the undamped frequency ω_A and the damping ratio ζ_A.

The success of the Moving Mass Control System (MMCS) depends upon a control law that selects a value of the commanded control mass position y_c, which rotates the MaRB to a roll angle commanded by the guidance algorithm. Reference 1 describes the design procedure based upon Linear Quadratic Regulator (LQR) methods using a full-state feedback. Essentially, the LQR method, by minimizing a performance index, selects the "best" state gains or constants. The states, weighted (or multiplied by) the appropriate gains are combined by an algorithm (controller) to set the command position y_c of the control mass.

Figures 7 and 8 present a graphical result of the movement of the control mass to develop roll. In Figure 7, both the position and speed of the control mass are shown. The stroke of the control mass is limited to one inch. Speeds are no larger than eight inches per second. Note that the mass moves to the right (positive) for about 0.3 seconds; according to Equation (17), the roll angle increases with the second integral of the mass position. Once the desired roll angle is achieved, the mass reverses direction, returning to null. With the turn completed, the mass moves to left of null (negative) to bring the roll angle back to zero.

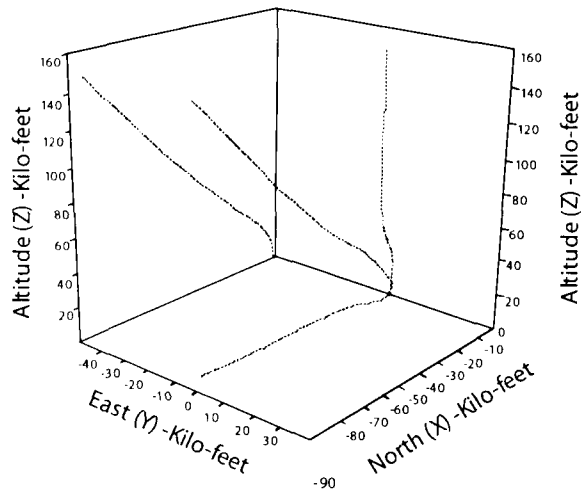

Figure 9—Mission Profile Trajectory

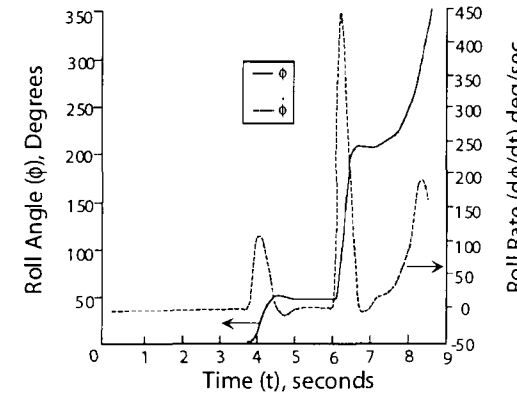

Figure 10—Roll Angle and Roll Rate vs. Time During the Mission Profile Trajectory

In Figures 7 and 8, reference is made to a design point. The design point is a point in a typical reentry trajectory where the performance of the autopilot is first evaluated. Among the design point parameters is a dynamic pressure of 50 Klbs/ft^2, a maximum roll angle of 10 degrees, and a maximum roll rate of 300 deg/sec. Further discussion of the design point is given in Reference 1.

SIMULATION OF A REPRESENTATIVE MISSION TRAJECTORY

The initial conditions for the Mission Profile Trajectory are as follows: velocity magnitude is 22,000 ft/sec, flight-path angle is 60 degrees, altitude is 150 Kft, and initial heading is north; the location of the initial point is 86.7-Kft south and 5-Kft west of the intended impact point.

The first maneuver consists of a low dynamic pressure suboptimal range extension maneuver initiated when the MaRB reaches 80 Kft. At this point, the guidance module commands the MMRC to roll the MaRB to a 45-degree roll angle and to maintain that attitude until the MaRB reaches an altitude of 40 Kft. The second maneuver (at high dynamic pressure) is initiated at 40 Kft. At this point, guidance commands from a cross-product steering algorithm are sent to the MMRC to direct the MaRB toward the target.

The results of the numerical simulation are shown in Figures 9 and 10. Figure 9 shows the three-dimensional trajectory and its projection in the cross-range, downrange, and ground planes. This plot shows that the MaRB turns to the east and pulls up slightly during the cross-range extension maneuver. It then pulls down toward the west to intersect the target.

The RB roll angle and roll rate are shown in Figure 10. This figure shows that the low dynamic pressure roll to 45 degrees was smooth and quick, with less than six percent overshoot (much like the response at the design point as shown in Figures 7 and 8). During the terminal target acquisition maneuver, the MMRC rolls the RB from 45 degrees to about 200 degrees. A small overshoot of the target near the end of the trajectory causes the MMRC to start rolling the MaRB back towards 50 degrees, at which point it impacts the ground. Figure 10 also shows that the roll rate never exceeds 450 degrees/sec.

Figure 11 is a plot of the relative lateral position vs. time of the moving mass with respect to the MaRB's a-frame. The smooth motion of the control mass is clearly evident. The final movement of the control mass is an attempt to correct for a slight cross-range overshoot of the target.

For the low dynamic pressure cross-range extension maneuver, β reaches a maximum of 0.05 degrees. Note the small negative initial spike (nose to the right) in β. This spike is caused by the reaction of the accelerating control mass in the direction of the positive y-axis. The adverse yaw reaches a peak of 0.13 degrees during the terminal target acquisition maneuver, which is performed at high dynamic pressure. The oscillations in sideslip are observed to be stable and well damped.

The adverse yaw that occurs during the maneuvering is shown in Figure 12.

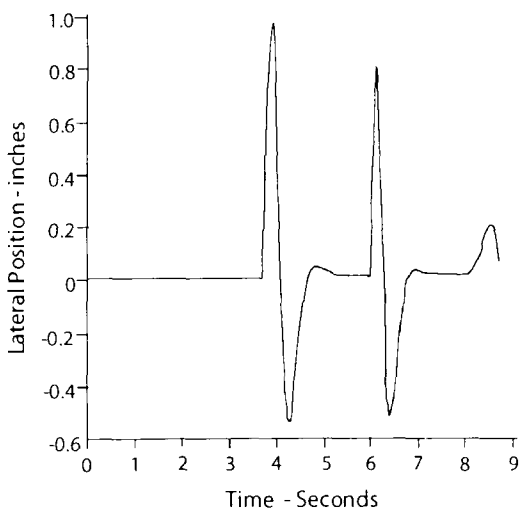

Figure 11—Lateral Position of Moving Mass vs. Time During Mission Profile Trajectory

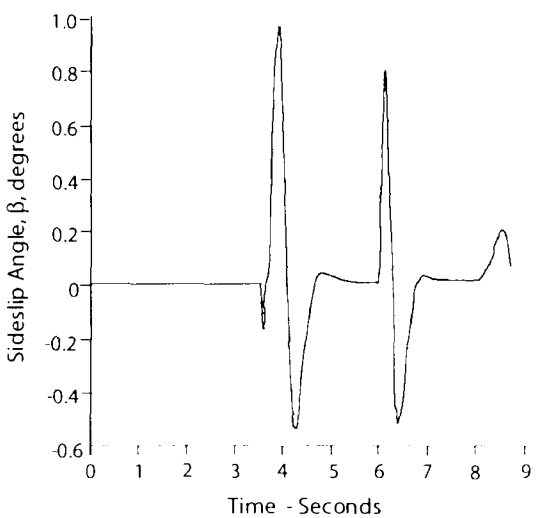

Figure 12—Sideslip Angle vs. Time During the Mission Profile Trajectory

CONCLUSIONS

An ongoing investigation has explored the utility and limitations of the moving mass controller. While no parallel simulation of the split-windward flaps was done, we might concede that the aerodynamic flap arguably produces a greater side force than the moving mass controller. However, against a benign or passive defense, large maneuvering loads are not required. The MMRC can easily steer out acquired trajectory errors without the high heating and dynamic loads that are part of the aerodynamic flap control. Even in an axisymmetric RB, a moving mass control can steer out over 1,200 feet of acquired trajectory error. However, the MMRC (in the fixed-trim RB) can alter the trajectory in a manner that is comparable to the split-windward flap without incurring severe heating loads.

The preliminary design of the fixed-trim RB followed from the derivation of the equations of motion of the moving-mass, two-body system. A linearization of the roll equation led to the mass effectiveness parameter, which was fundamental in the initial sizing of the control system. Further analysis showed that a small improvement in the control system response was possible by locating the control tube below and to the rear of the RB's center of mass.

Linear Quadratic Regulator synthesis was used to design the roll autopilot at one value of dynamic pressure. To obtain design-point roll response at off-design-point flight conditions, a gain scheduling function was generated; the argument of this function is the ratio of free-stream to design dynamic pressure. A nonlinear 7-DOF simulation enabled the fixed-trim MaRB to successfully complete a low dynamic pressure suboptimal cross-range extension maneuver and a high dynamic pressure terminal target acquisition maneuver. The response of nonlinear aerodynamic, inertial and dynamic cross-coupling predicted by the governing equations of motion did not significantly degrade performance of the linear moving mass control autopilot.

Because this effort is preliminary, roll disturbance torques arising from heatshield ablation were not modeled. In the future, certainly more sophisticated aerodynamic modeling should be used, particularly the inclusion of the effects of shape change on control robustness.

In spite of the limitations of this preliminary investigation, MMRC appears to be a relatively simple and effective method of modulating the roll angle of a lifting RB. The MMRC certainly deserves serious attention as a viable alternative to the more conventional aerodynamic flap and thruster roll control.

REFERENCES

1. Petsopoulos, T.; Regan, F.J.; and Barlow, J., "Moving Mass Roll Control System for a Fixed-Trim Reentry Vehicle," *Journal of Spacecraft and Rockets*, Vol. 33, No. 1, pp. 54-60, Jan-Feb 1996.

2. Gentry, A.E.; Smyth, D.; and Oliver, W., *The Mark IV Supersonic-Hypersonic Arbitrary-Body Program*, AFFDL-TR-73-159, Wright-Patterson Air Force Base, OH, Nov 1973.

THE AUTHOR

MR. FRANK J. REGAN

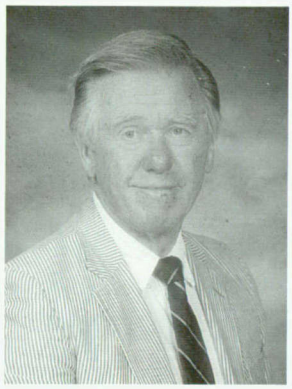

MR. FRANK J. REGAN is a graduate of the Massachusetts Institute of Technology with B.S. and M.S. degrees in aerospace engineering. Upon graduation, he worked in industry for about four years. In 1962, he joined the Naval Ordnance Laboratory (NOL/White Oak) as an aerospace engineer. His specialty was weapon dynamics; he had responsibility for making extensive wind tunnel measurements mainly at NOL, but also at other facilities, such as the Taylor Model Basin and the Arnold Engineering and Development Center (AEDC) in Tullahoma, Tennessee. He was instrumental in developing the wind tunnel free-flight technique, Magnus measurement balance, electromagnetic pitch damping transducers, air-bearing pitch and roll damping supports, and radio frequency (RF) telemetry from wind tunnel free-flight models and associated data reduction methods. In the more recent past, he has been active in the modeling of RB trajectories with a variety of end constraints emphasizing inertial navigation and guidance algorithms. He has written over 30 papers, which have appeared in refereed journals. He has been an adjunct faculty member of the Department of Aerospace Engineering of the University of Maryland, College Park, Maryland, for the past 15 years. He has also written two books on the dynamics associated with atmospheric reentry. At present, Mr. Regan is Group Leader of the Flight Mechanics Group at NSWCDD.

FREE—Algorithm for Solution of an SLBM Multiple Constraint Mission Problem

Ms. Shawna M. Davis and Mr. Davis L. Owen

The TRIDENT missile consists of four stages and multiple reentry bodies (RBs). Each RB flies a trajectory that is subject to its own constraints as well as being constrained by the trajectories of other reentry bodies. The ensemble of trajectories of the individual reentry bodies needs to be designed to avoid all constraints. Each RB trajectory must stay within the RB survival envelope. The ensemble of trajectories must minimize energy requirements for the missile, allow spatial separation of the trajectories, and control the time/impact patterns to maximize effectiveness.

Currently, each Trident missile is programmed to allow all its RBs to reach their respective targets without encountering intramissile constraints. However, the current process removes violations successively and can result in a solution that is suboptimum. This article describes a new algorithm where a system of constraint equations is developed to yield simultaneous solutions for all RB trajectories. These equations are solved by a least-squares method and result in a solution that is superior to the existing methodology. When developed fully, this algorithm has the potential to solve the constraint problem while not degrading system performance.

Introduction

Each RB carried by the TRIDENT missile is given an independent mission and flight time. The flight times are controlled by the time-of-flight (TOF) preset assigned to each RB. In the absence of constraints on any RB path or between any pair of RB trajectories, the TOFs are assigned to minimize the energy used by the missile to deploy the RBs. If constraints are violated, the TOFs are used to resolve constraints.[1]

The three major constraints affecting TOFs are to:

- Guarantee separation or spacing between RBs during flight
- Assure all RBs are within the RB survival envelope
- Avoid undesirable time and geometric relationships between RBs at fuzing

The first two constraints are hard constraints and are enforced by rigorous mathematical algorithms. The third constraint is handled indirectly by modifying the mission and by observing the effect on the TOF computations. Unlike the first two constraints, it is acceptable to minimize the occurrences of this constraint.

CURRENT ALGORITHM

All RBs are numbered and referenced according to the order that they will be released. The TOFs are currently computed recursively based on the RB release order. This process is initiated by the computation of the first RB's TOF, which is computed to satisfy mission requirements independent of any of the issues contained in this article. All TOF computations, including first body TOF, are dependent upon ship's position, and results can vary significantly over the projected patrol area.

The first two constraints are currently resolved directly in the computation of the TOFs. The conflict resolution process is begun by requiring that the initial estimate of each RB's TOF minimizes the velocity increment required to place it on its desired trajectory. This is denoted as the minimum energy (min energy) TOF (see Figure 1). The algorithm enforces the spacing constraint by computing time stayout windows for each RB based on the trajectories for all previously processed RBs (see Figure 2). For example, if the nth TOF is being computed, time stayout windows are computed with respect to the first through n^{th}-1 RB trajectories. If the min energy TOF falls into one of these stayout windows, TOF is increased to the minimum value outside of any stayout windows. If the final value of TOF violates the RB survival envelope, the algorithm then must search for an acceptable value. The RB survival envelope determines the minimum and maximum values of TOF.

The third constraint on TOF is due to impact time/position geometry and is expressed as a series of time-dependent ellipses. These ellipses are on the earth's surface near the impact area and, for each pair of RBs, can be written as a function of their TOF differences. The ellipses are used to determine an Impact Effectiveness (IE) ratio for each RB pair (see Figure 3). A ratio of 1.0 or greater is acceptable. Impact constraint violations can normally be minimized or eliminated by modifying the mission assigned to the missile in a way that changes the TOFs. Common techniques include interchanging the targets assigned to the RBs or iterating the spacing parameters.

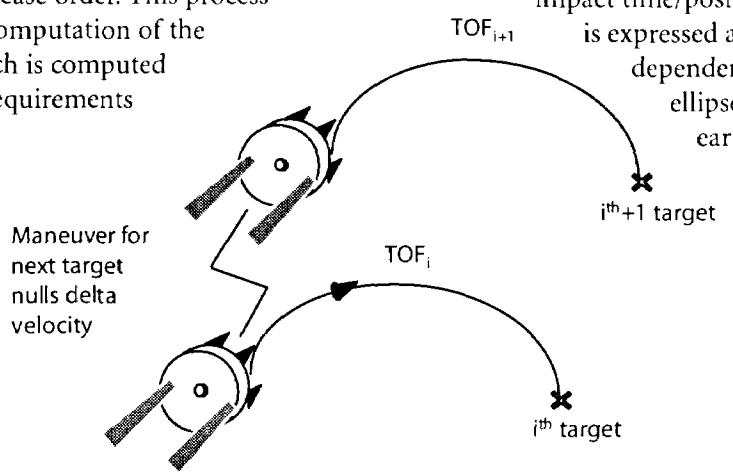

Figure 1—Minimum Energy TOF

Two disadvantages of the present methodology prompted this investigation into an improved algorithm. First, the impact geometry constraint is ignored during the actual TOF

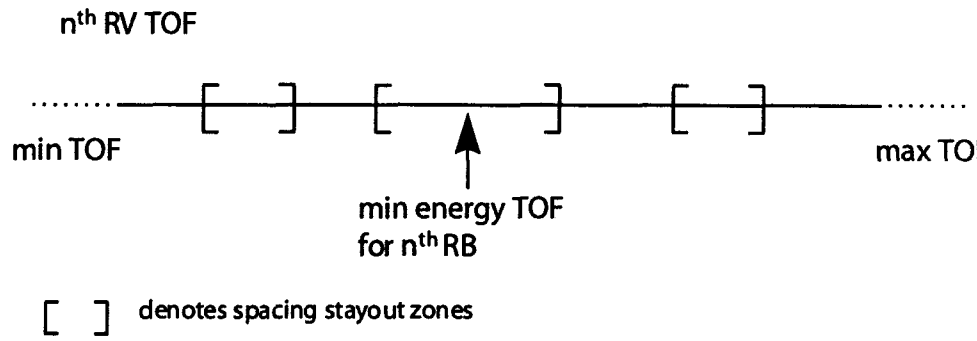

Figure 2—Window Concept for Spacing

construction and is satisfied later by a process of modifying the mission and observing the result. Second, it has been observed that the rule to increase TOF to satisfy spacing sometimes degrades the final solution. For these reasons, the present methodology frequently gives a solution that is suboptimum.

The new algorithm described in this article unifies all TOF constraints into one solution. The goal is to find the set of TOFs closest (least squares) to min energy that satisfy all constraints. This goal preserves the best features of the present methodology while repairing its deficiencies. First, the min energy concept is preserved and strengthened. Second, the technique of removing TOF constraints by time windows is preserved. The increase/decrease TOF issue for spacing is resolved by allowing the least squares to pick the best solution. Previous attempts to solve this problem with time windows floundered due to the fact that the spacing stayout windows are in RB release order, but the impact time windows are in impact order. This dilemma was resolved by replacing the recursive computation of TOFs by a simultaneous solution for all TOFs.

FREE ALGORITHM

There are two types of spacing constraints. The first constraint is actually a minimum velocity between consecutive RB deployments, which is mathematically equivalent to a variable spacing. The second constraint ensures spacing between all consecutive and nonconsecutive pairs. Since the spacing for nonconsecutive pairs is normally used to maximize IE, it became extraneous for FREE and was therefore eliminated. FREE recognizes the remaining spacing constraints on consecutive pairs and expresses them as time stayout windows.

RB survivability constraints are currently not defined in terms of a time window. The conditions the RB would encounter at reentry are predicted as a function of TOF and tested against the RB reentry envelope. This poses a slight problem for the FREE algorithm since a violation of minimum or maximum TOF is known only after a solution is found. However, this is not a serious concern since avoiding survivability constraints is one of the factors in the computation of the first RB TOF.

With FREE, the impact geometry constraint is used in conjunction with the spacing and survivability constraints. A couple of simple, but important, changes were made to the impact geometry computations. Originally, an IE ratio for each pair of RBs would be computed based on their impact time. The new method assumes all TOFs are initially the same. It then varies the TOF of one RB of each pair. This variance is done in increments from $-y$ to $+y$, where y is a given delta time from the TOF. With each TOF adjustment, the IE ratio is computed. The result is that for each pair of RBs, a time window where the IE ratio is above

1.0 can be found. Impact time windows are no longer dependent upon the impact order but can remain numbered based on their release order. This makes the IE time windows, or stayin windows, compatible with the other constraint windows.

All time windows are determined for each specified launch point in a given patrol area. An algorithm was developed to take the time windows for each launch point and determine one set of time windows that encompass the patrol area. An example of how these time windows are combined is provided in Figure 4. In Figure 4(a) the combining of stayin windows is depicted. Figure 4(b) depicts the combining of stayout windows. Once the time windows have been defined for the launch area, another algorithm is needed to combine the stayin and stayout windows for each pair. The stayout windows apply only to consecutive RBs. Stayin windows apply to both consecutive and nonconsecutive pairs (see Figure 5). The result will be stayin windows for each pair of RBs that encompass the entire patrol area. Any TOF within these windows is valid.

There are many benefits to describing the constraints as time windows. First, there is no need to iterate to find a conflict-free TOF. The constraints can be solved simultaneously. Second, there is no restriction on the direction of adjusting TOF. It can be increased or decreased from min energy TOF. Third, the optimum TOF can be found by forcing the TOF to be as close to min energy TOF as possible.

OPTIMIZATION ALGORITHM

The optimum TOF is solved for using a least-squares algorithm. The algorithm implemented takes the form of a least-distance programming technique (LDP),[2] which solves the system of equations of the form

$$\text{minimize } \|x\| \text{ subject to } Gx \geq h \qquad (1)$$

where

x = Solution vector of size n-1, where n equals the number of RBs to release. This vector contains the time increment from min energy TOF for each of the RBs, except the first.

G = Matrix of size $m \times n$-1 that contains ones, negative ones, and zeros, where m equals $(n-1)n$. This matrix is used to reference the time increments (x-components) to their corresponding stayin windows (h-components).

h = Constraint vector of size m that contains the start and ending times of the windows.

Gx is greater than or equal to h if every element of Gx is greater than or equal to the corresponding element of h.

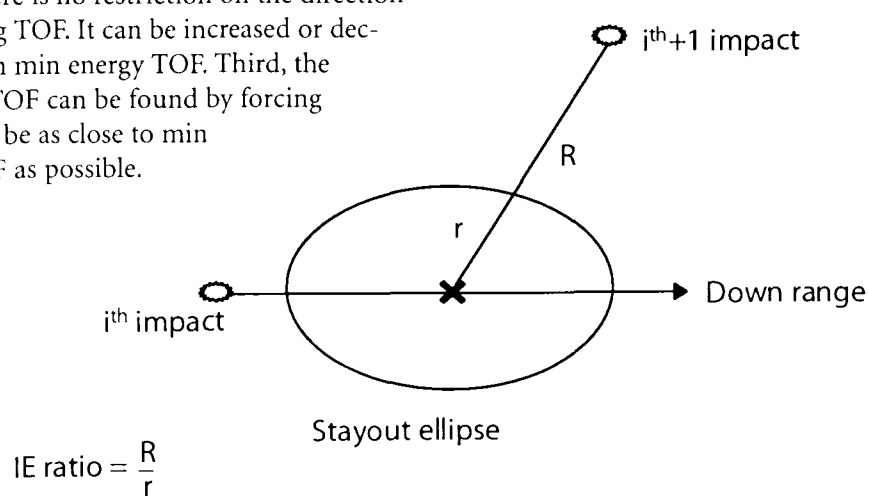

Figure 3—Impact Effectiveness Ratio

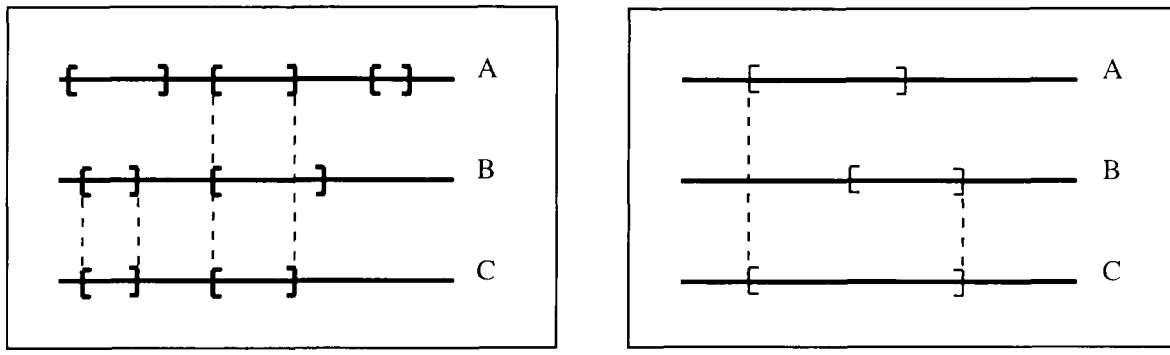

(a) Stayin Windows - IE constraints

(b) Stayout Windows - Spacing constraints

Figure 4—Combining of Windows for All Launch Points in Given Patrol Area

A: one through n^{th} launch points B: n^{th}+1 launch point C: one through n^{th}+1 launch points

The LDP technique described by Reference 2 obtains a solution to an arbitrary set of linear inequalities $Gx \geq h$ by reducing the problem to a form where the nonnegative least-squares method (NNLS)[2] can be invoked. NNLS computes x for the following least-squares problem

$$\text{minimize } \|Ax - b\| \text{ subject to } x \geq 0 \qquad (2)$$

This is closed-form and usually terminates after a reasonably small number of iterations. If $Gx \geq h$ has a solution, LDP will compute x of minimal norm, satisfying the inequalities. If the constraints are not compatible, the algorithm indicates that fact and then terminates.

As illustrated in Figure 5, it is possible to obtain more than one stayin window for any particular pair of RBs. The least-squares method is restricted to using one stayin window per pair. It is not feasible to check every combination of windows through the least squares to determine the best solution. However, it was found that almost any combination that produced a valid solution was as good or better than the current algorithm.

APPLICATIONS

FREE can be utilized in various ways. Its original design purpose was to deconflict a mission over an entire patrol area. The only

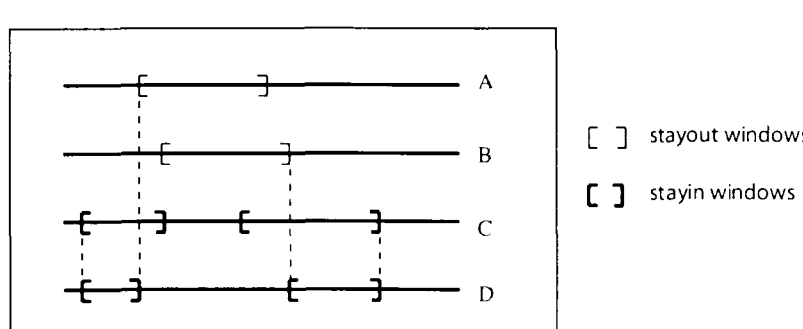

Figure 5—Combining of Windows for Consecutive Pairs of RBs

A: 1st spacing constraint B: 2nd spacing constraint C: impact effectiveness D: final resulting stayin windows

necessary input is the minimum and maximum latitudes and longitudes, and the degree of increment. If it exists, FREE will find one TOF for each RB that avoids spacing restrictions, maintains reentry survivability, maximizes IE, and minimizes the use of propellant. It is a simple, one-step process to deconflict the patrol area.

Often, it is desirable to know how the solution for the patrol area will work just outside the patrol area boundary. FREE has the capability of finding a solution for the given patrol area and then checking that solution over a specified expanded area.

Another method for using FREE is to deconflict strictly one launch point. FREE is extremely powerful in this point-by-point mode. It is useful when trying to find a solution for a difficult launch point. FREE will attempt to resolve the constraints for the given launch point. If it is not physically possible to resolve the constraints, the output from FREE will explain the reason: reentry survivability, spacing, IE, propellant usage, or a result of the interaction of these constraints.

In some situations, the mission may not be resolvable. If targets are tightly packed, it may not be possible to obtain an IE ratio above 1.0. If this target package cannot be modified, then it is still possible to use it, albeit with degraded effect. This degradation can be minimized by allowing IE ratios slightly below 1.0. The current conflict resolution process does not allow any flexibility in the IE ratio limit. However, the ratio limit in FREE is an adjustable variable. This allows FREE to minimize the negative effects of unavoidable conflicts.

RESULTS

The two main uses of FREE would be to deconflict a single launch point and to deconflict a patrol area. Many test cases were used as a checkout for FREE. In all scenarios, FREE did as well or better than the current process. Figures 6 and 7 are used to illustrate the improvement obtained by using FREE. All the examples are fictitious and do not indicate latitudes or longitudes.

The first example (Figure 6) illustrates the usefulness of FREE in the point-by-point mode. Each small square represents a launch point, of which there are approximately 1,000. The white area indicates launch points that were deconflicted. The light gray rectangle in the middle is an unachievable region that contains the targets. Dark gray areas indicate launch points that cannot be deconflicted. There are no TOFs that

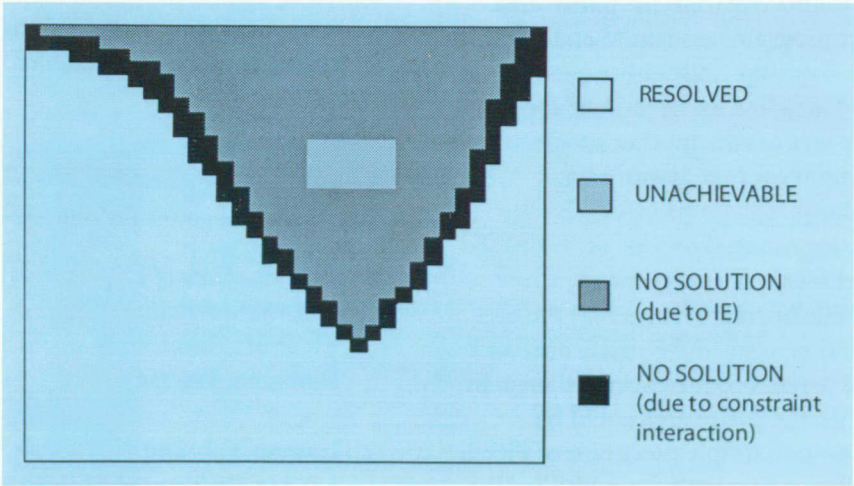

Figure 6—FREE Results Using Point-By-Point Method

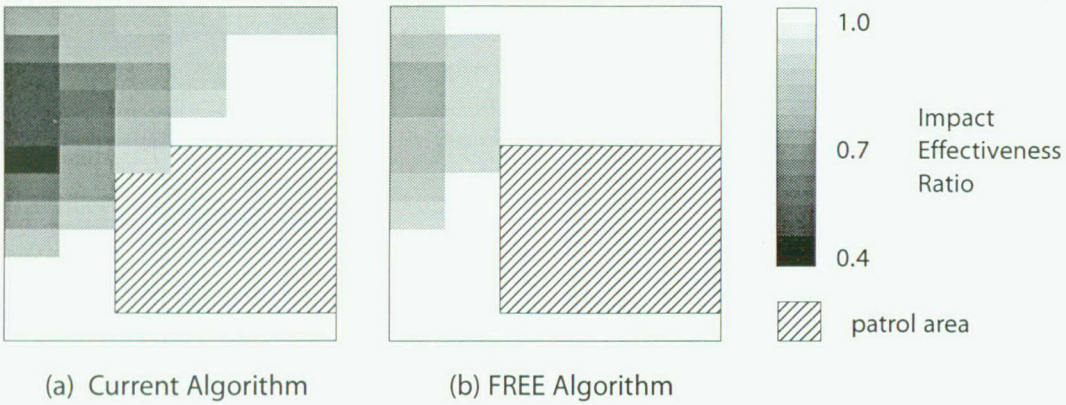

Figure 7—Impact Effectiveness Ratio Results for Deconflicting a Patrol Area

give an IE ratio above 1.0. The only way to use the mission for these launch points is to allow a ratio below 1.0. Black areas indicate launch points with no solution. Interaction of the spacing constraint with the IE constraint for a consecutive pair of RBs precludes a solution. A valid solution with an IE ratio above 1.0 may be possible if the release order is modified so that the conflicting pair is nonconsecutive instead of consecutive.

The second example (Figure 7) shows how FREE can be used to deconflict an entire patrol area. For the current process, the first step was to run a program to remove spacing and survivability conflicts within the patrol area. Next, another program was run to analyze the IE ratio. In this example, the entire patrol area and expanded area had an IE ratio of about 0.4. The final step was to run another program to improve the ratio over the patrol area. Figure 7(a) shows the results of the IE ratio. The outer box indicates the expanded area, and the cross-hatched box inside the expanded area indicates the patrol area. The current process deconflicted 96 percent of the patrol area and just under 50 percent of the expanded area. In contrast to this, the patrol area could be deconflicted by one simple execution of FREE. Figure 7(b) shows the result from FREE. All spacing and survivability constraints were avoided for the entire area. The IE ratio is above 1.0 for 100 percent of the patrol area and 75 percent of the expanded area.

Conclusions

Controlling flight time to avoid constraints is a topic of current interest in the Submarine Launched Ballistic Missile (SLBM) community. FREE is the initial prototype algorithm developed in response to these concerns. The ideas contained in FREE should represent the foundation for future constraint resolution algorithms. It is easily used and can be adapted for many applications. FREE is a good example of how existing concepts and methodology can be reexamined and reassembled into powerful new algorithms.

References

1. Ray, J.F., *Time of Flight Generation for Constrained Ballistic Trajectories*, NWL TR-2955, Naval Weapons Laboratory, Dahlgren, VA, May 1973.

2. Lawson, C.L. and Hanson, R.J., *Solving Least Squares Problems*, Prentice-Hall, New Jersey, 1974.

THE AUTHORS

MS. SHAWNA M. DAVIS

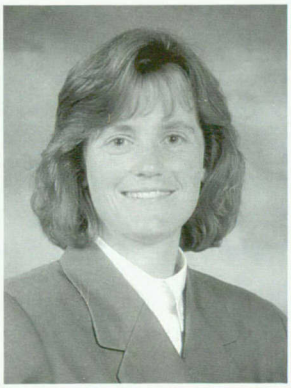

MS. SHAWNA M. DAVIS earned a B.S. with honors in aerospace engineering from the University of Cincinnati in 1994. Since arriving at the Naval Surface Warfare Center, Dahlgren Division (NSWCDD) in 1991 as a Cooperative Education Student, she has worked primarily on six degree-of-freedom missile simulations. She has identified and developed innovative trajectory modeling methodologies and applied them in the investigation of advanced system concepts and SLBM weapon system evaluation. Ms. Davis has coauthored an AIAA paper on high-angle-of-attack aerodynamics. In 1994, the Chief of Naval Operations recognized her as the Navy's Co-op of the Year in Science and Engineering. Ms. Davis is currently completing requirements toward an M.S. degree in aerospace engineering from the University of Colorado through NSWCDD's Academic Fellowship Program. She is a member of Sigma Gamma Tau and Tau Beta Pi honor societies, and the American Institute of Aeronautics and Astronautics.

MR. DAVIS L. OWEN

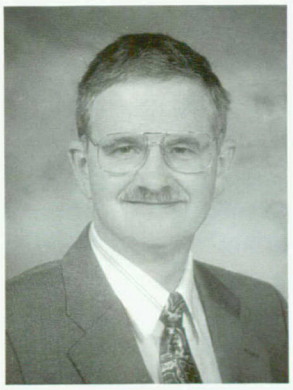

MR. DAVIS L. OWEN received a B.S. degree in mathematics from Millsaps College in May 1964 and an M.S. in mathematics from the University of Southwestern Louisiana in June 1966. Since then, he has been employed at NSWCDD, where he has been involved with various aspects of SLBM presetting and performance. His work has centered around trajectory simulation including gravity, reentry, and fuzing. In November 1986, Mr. Owen received the Navy Meritorious Civilian Award for his work on gravity modeling.

Fuzzy-Logic-Based Expert System Solutions to Sequencing and Grouping Problems

Mr. Patrick L. Godin

Determination of near optimal solutions to sequencing and grouping problems that have multiple optimization and constraining factors has been a challenge for even the most advanced computational methods. Sequencing and grouping problems can range from assigning children to school buses to assigning missions to reentry bodies on ballistic missiles. This article describes an approach to solving these problems that combines the benefits of expert systems and fuzzy logic. Expert systems provide for the systematic collection and integration of rule-based knowledge in an effort to apply the rules to new problems, and fuzzy logic allows variables and problems to be expressed in linguistic terms similar to what humans would use in making decisions. Methods for tuning or training the system may use other advanced computational methods such as neural networks, simulated annealing, or genetic algorithms. The steps in designing and maintaining a fuzzy-logic-based expert system will be discussed, as well as the benefits obtained from such an approach.

Introduction

The search for the smartest way to accomplish a task has always been a tradition of the U.S. military and, with recent cutbacks of manpower and resources, the need to obtain maximum capability from a system is greater than ever. The processes involved in allocating resources to achieve missions are being closely examined, and many of these processes include sequencing and grouping tasks. A sequencing and grouping task is defined to be any task that distributes assets in groups in a sequential manner. Any type of pickup or delivery system inherently requires a sequencing and grouping problem to be solved. Some examples of sequencing and grouping problems include delivering supplies to troops, bus routes, mail carrier routes, and mission planning. Due to the large number of permutations, it is not practical to sort through all possible assignments to find the best solution. This article will use a mission planning example to illustrate the difficulties associated with the sequencing and grouping problem, and how fuzzy-logic-based expert systems can ease these difficulties.

Many techniques have been used to solve the sequencing and grouping problem. The techniques range from the ever popular *educated guess* method to highly advanced computational methods, such as neural networks, genetic algorithms, and simulated annealing. Many of these advanced computational methods have failed to produce results that are better than the *educated guess* method in which a human expert examines the problem and constructs a solution by hand. One failing of the advanced computational methods is that they do not fully examine the cause and effect relationships between variables. Many sequencing and grouping problems require a large number of constraints to be satisfied. A well constructed fuzzy-logic-based expert system (also known as a fuzzy expert system) will account for relationships between variables in an intuitive fashion that is similar to what the human expert uses in the *educated guess* method. Fuzzy expert systems should be able to solve many sequencing and grouping problems.

Expert systems try to capture the thought processes used to make decisions. Conditional phrases are constructed to solve problems. Some decisions are easy to evaluate such as, "If the light is red, then stop." Other decisions may be more difficult such as, "If the light turns yellow while the car is going fast, and there is a long distance before the light, then stop." In this second example, *fast* and *long distance* are vague terms that can be represented by fuzzy variables. Fuzzy variables and fuzzy logic are mathematical constructs that capture the uncertainty in the data and qualifiers that are used to reach decisions. Using fuzzy logic with expert systems allows the thought processes to be expressed in linguistic terms, which makes the solution easier to construct and maintain.

PROBLEM DEFINITION

Figure 1 illustrates a mission planning sequencing and grouping problem that is being examined at the Naval Surface Warfare Center, Dahlgren Division (NSWCDD).

In the problem of grouping and sequencing, missiles will deliver Reentry Bodies (RBs) to multiple impact areas. The two aspects of the problem are defined as:

1. Grouping—Selecting the set of targets to be assigned to a specific missile.

2. Sequencing—Ordering the selected set and assigning them to individual RBs.

Both must be done in a way that satisfies specific constraints related to missile performance and targeting policy. Any problem of this magnitude requires clear and concise information management. A hierarchy of data structures has been established and is shown in Figure 2. The advantages of such a hierarchy are that each data element is stored in only one location and that it is easy to switch whole blocks of data. For example, since all the

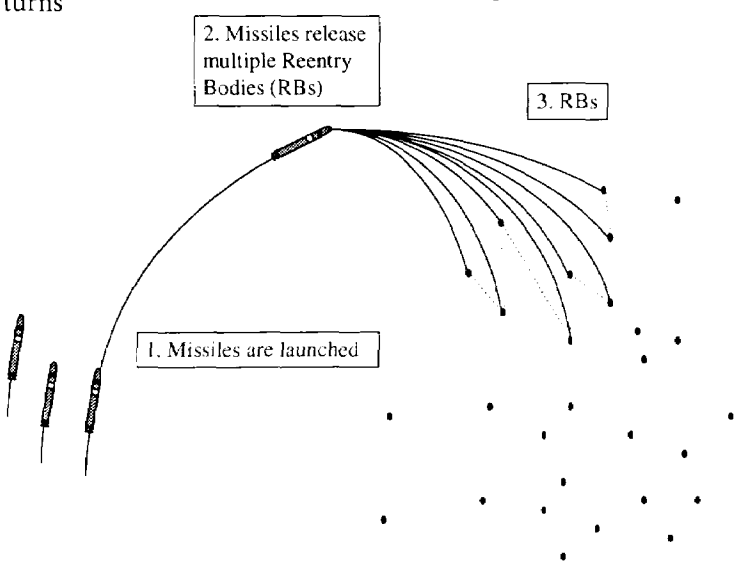

Figure 1—Example of Sequencing and Grouping Problem

information related to a single missile is contained within the missile data structure, it is easy to swap a missile from one launch facility to another. This requires only that the pointers to the launch facilities and missiles be exchanged, as opposed to copying all the missile information.

The following constraints are placed on the assignment of missions to missiles:

1. Each mission must be achievable; that is, each missile must have enough propellent to release all RBs so that each RB falls to the intended impact area.

2. Certain groups of missions must be assigned to the same missile. This is known as an impact selection constraint.

3. Mission activation may be constrained to occur before or after another mission. This is known as a mission activation constraint.

For a solution to be acceptable, all of these constraints must be satisfied.

BUILDING A FUZZY STRUCTURE

Before building the basis of the fuzzy framework, why use fuzzy terms at all? In most of the reasoning we do every day, we do not concern ourselves with the extent to which a characteristic exists but only that a characteristic does exist. For example, in deciding whether to take an umbrella, we ask ourselves if it looks like it is going to rain. If it is going to rain, we do not care whether it is going to rain one inch or two inches, because either way we are going to need the umbrella. In solving the sequencing and grouping problem, we are concerned that the distance traveled by each missile is within the achievable range, but usually we are not concerned with the extent to which it is achievable. By limiting ourselves to general characteristics, less time is spent measuring the characteristics, and more time is devoted to solving the problem.

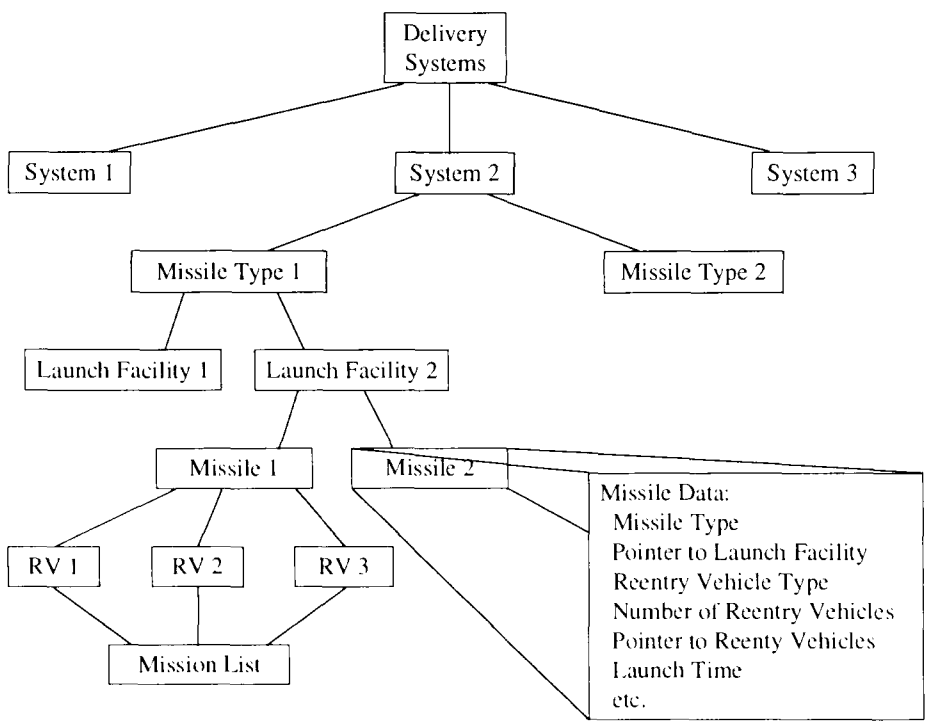

Figure 2—Data Hierarchy

The lowest level of fuzzy variables are those that can be directly measured. These will be referred to as *basic* or *building block* variables. For example, the distance between two impact areas is a basic variable. The basic fuzzy variable may be measured and characterized into several different categories, as is shown in Figure 3. Two specific fuzzy variables, **x** and **y**, are also shown. The value of the abscissa is the spacing between two impact areas, and the value of the ordinate is the extent to which a particular spacing is a member of the fuzzy categories *very small, small, medium, large*, and *very large*. Italics will be used to denote fuzzy categories and functions, while bold will be used to designate fuzzy variables. The distance **x** in Figure 3 fully belongs to the membership set *small*, but does not belong to any other membership set. The distance **y** is somewhere between a *medium* distance and a *large* distance. It belongs to the *medium* distance category to the extent of 0.4, and to the *large* category to the 0.6 extent. It is important to note that the extent to which a variable belongs to a particular category is not directly related to a probability. In the above example, the value of **y** is not 60 percent likely to be in the *large* category. The value is simultaneously in the *medium* and *large* categories. It is helpful to view this multiple membership in the sense that some experts would categorize this distance as *medium*, and some experts would categorize it as *large*. The process of defining categories is often subjective; however, these subjective categories are the basis for handling uncertainty in a rigorous manner. A nonsubjective method of defining the categories will be presented later.

The number of categories is related to the fidelity needed to solve the problem. If a fuzzy variable is used to characterize a switch as *on* or *off*, two categories might be sufficient. Three categories or more, for example, might be needed for characterizing wavelengths of light into colors. The choice of names for categories is left up to the developer, but the names should be chosen to make the code as easy to read as possible and to match the type of reasoning usually performed with the variable. One confusing factor that often creeps into fuzzy logic is the multiplicity of meaning that some names take on. For the sequencing and grouping of missions, two fuzzy variables that may be defined are the distance between impact areas, and the distance between the launch point and the first impact area. The categories for both of these variables may be *very short, short, medium, long*, and *very long*. In this case, the categories named *very long* have very different values. A *very long* distance between the launch point and the first impact area may be in the range of 3**x** miles, while a *very long* distance between two impact areas may be in the range of **x** miles. The other categories also have different values. To avoid confusion, care should be taken to ensure that the context in which a category name is used is clear.

In the development process, the boundaries of the categories of a basic fuzzy variable must be determined. This can be done in several ways. The fuzzy logic developer can ask several experts. For our example, the question may be, "At what distance do you consider the impact area to be a very long way away from the launch

Other basic fuzzy variables are given in Table 1. Since one of the primary advantages of fuzzy logic is the ease of creating and maintaining a program due to the linguistic nature, it is usually beneficial to name the fuzzy variables with full easy-to-read names.

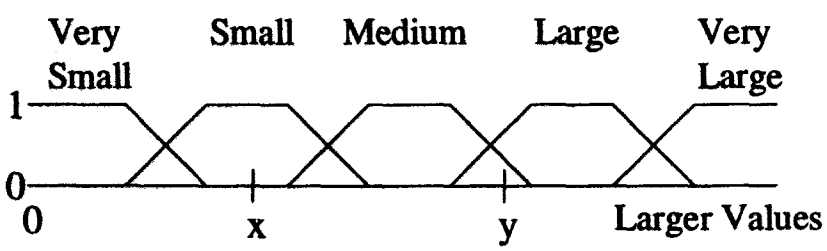

Figure 3—Impact Area Spacing as a Fuzzy Variable

Table 1—Basic Fuzzy Variables

VARIABLE	DESCRIPTION	CATEGORIES
mission length	combined length of line segments connecting the impact areas	very short, short, medium, long, very long
missile range	distance from launch point to first impact area	very short, short, medium, long, very long
impact time delta	time between impacts of two RBs	very soon, soon, medium, late, very late
mission spacing	distance between the center of two missions	close, medium, far

point?" After answers are collected from several experts, the lowest answer may be taken as the point where the distance is said to be *very long* with a strength of 0.0, and any distance greater than the highest answer is assigned a strength of 1.0. Between the lowest and highest answers, the strength of being *very long* may increase linearly, quadratically, or in some other manner. Usually the strength is assumed to increase linearly. Another way of setting the boundaries on the categories is to pull from a data base of past values and assume a certain percentage belong to a given category. Figure 4 shows an example in which distances are pulled from a data base that meets all the constraints. These distances are sorted into ascending order. The developer defines a certain percentile of the ascending list to be in a particular category. The choice of percentages that are assigned to each category is arbitrary but should reflect the nature of the categories.

From the basic fuzzy variables, more complex concepts can be determined. For example, a mission may be defined as *highly* achievable if the distance from the launch point to the first impact area is not *very large*, and if the spacing between impact areas are all *at most medium* distance. The terms distance and spacing are used to refer to two separate and distinct fuzzy variables. Since complex fuzzy variables such as achievability are not determined directly, but are determined by combining basic fuzzy variables, they usually have values that range from zero to one.

In determining achievability, several fuzzy functions have been used. They are: *not*, *and*, and *at most*. Each of these functions have definitions that are similar to their counterparts in classical logic. These fuzzy functions are defined in Figure 5. Each of these fuzzy functions return a value from zero to one that represents the truth of the function. In Figure 5, the *and* operation is defined as the product of the two fuzzy variables; while in other applications, the *and* function is defined as the minimum of two fuzzy variables. Each time an operation with more than one possible definition is used, care should be taken to ensure that there is no confusion about which definition is desired.

The value *at most medium* for x in Figure 5 is 1.0, while the value for y is assumed to be 0.4 for this example. If the spacing between impacts is y, and the distance from the launch point to the first impact area (d) is *very large* to the

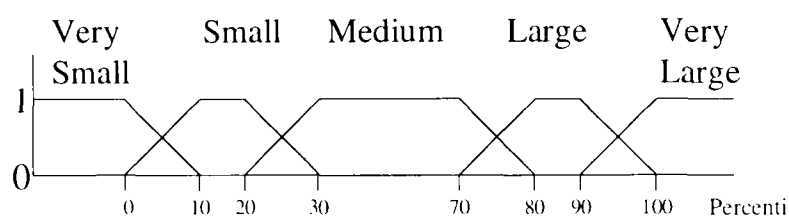

Figure 4—Categories Based on Percentile of Data Base Values

strength of 0.1, then the mission is *highly* achievable to the extent of:

Highly Achievable = [d *not very large*] *and* [y *at most medium*]
= [*not*(0.1)] *and* [0.4]
= [0.9] *and* [0.4]
= 0.36

Two very important benefits of fuzzy logic are illustrated by this example. The first benefit is that it is very easy to go from a verbal description of a calculation to the calculation itself. Typically, this will reduce the effort necessary for each part of a programming effort, from the design and formulation stage through checkout. The second benefit is that the end result provides a quantity that can easily be compared to other computations. If there is a second mission with d equal to 0.2 and y equal to 0.6, then it is easy to determine that the second mission is more *highly* achievable than the first mission since it has a strength of 0.48. Many traditional methods of computing achievability have determined only if a mission is achievable or not achievable. Other methods determine how achievable a mission is by doing complex calculations to find quantities, such as propellent remaining at the end of the mission.

Another aspect of fuzzy logic is the use of modifiers on fuzzy variables. For example, a statement can be said to be *very true* or *very false*. To achieve these degrees in fuzzy logic, the truth value is passed through a modifying function, such as the one shown in Figure 6.[1] This function lowers the truth value to the point where only values that are *true* to a large extent are considered to be *very true* to a moderate extent. There are many other modifiers, such as *often*, *somewhat*, and *never*, that can be used with fuzzy variables. To

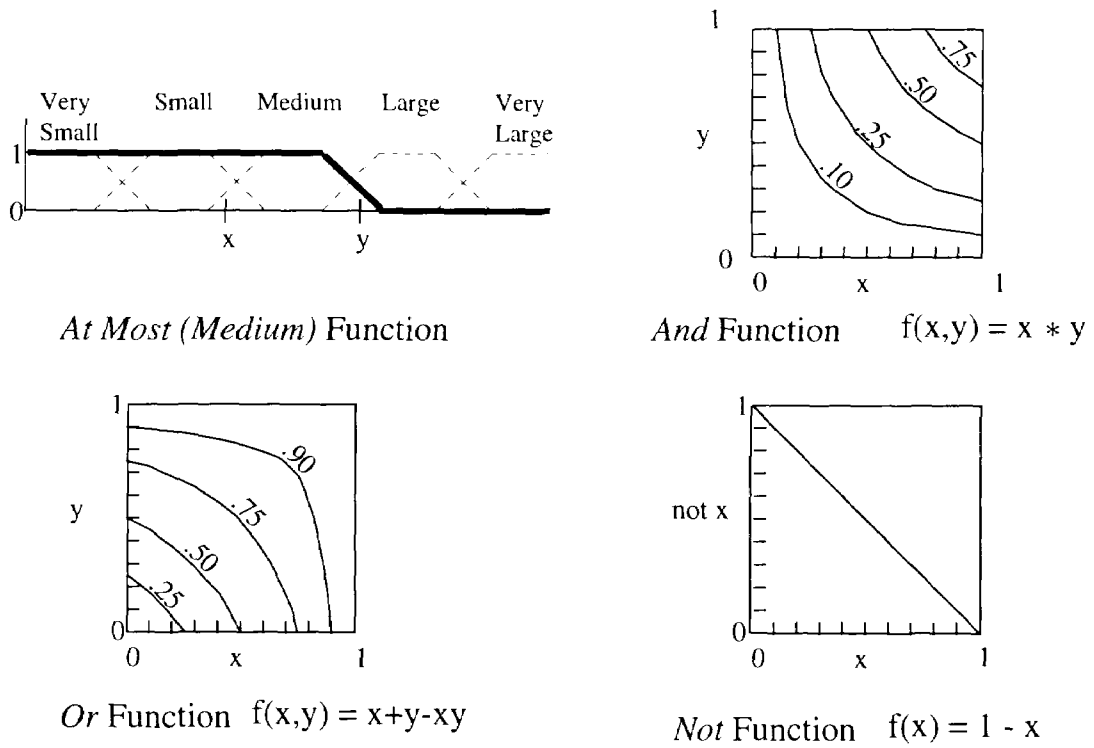

Figure 5—Several Fuzzy Functions

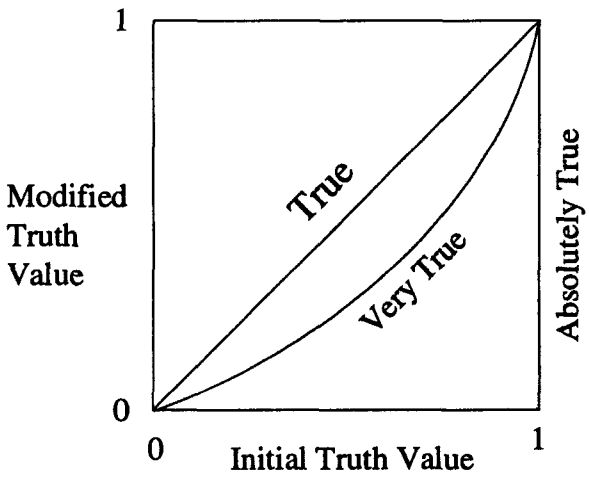

Figure 6—Fuzzy Modifier Example

illustrate the wide range of possible uses, consider that the category *very long* of the mission spacing fuzzy variable could be replaced with a *very* modifier on the *long* category.

BUILDING AN EXPERT SYSTEM

Expert systems use constructs of the form if-then-action to accomplish a task or reach a decision. The mission achievability comparison given above can become a natural part of an expert system. Since fuzzy logic provides a quick and easy way to compare values, expert systems can use fuzzy logic to evaluate conditional phrases. An action initiated by an expert system might be to exchange two impact areas in a mission to make the mission more achievable.

In designing an expert system, it is usually easiest to start with what already works. The human expert should be interviewed, and the methods used to accomplish the task should be studied. Before constructing an expert system, the following questions should be examined:

1. What criteria will be used to evaluate possible solutions? This may be an objective that is desired in the final solution, such as the criteria that all missions are achievable and satisfy the activation time and impact selection constraints. Or it may be an incremental objective, such as a criterion that each spacing between impact areas be of *medium* length.

2. How important is the optimum answer? What is the trade-off between the quality of the answer and the time the program takes in development and execution?

3. How robust should the program be? Should it be able to handle many different tasks, or should it be designed to do a very specific task?

4. What information is easily obtainable? The distances between impacts, launch points, or missions can be used to make decisions.

5. What actions, such as switching impact areas, will assist in achieving the goals?

6. Under what conditions should the actions be taken? This may be composed of the easily obtainable information and the criteria selected above.

All of these factors should be incorporated into an expert system.

Figure 7 illustrates the flow of an expert system. The process starts by the user defining the goals to be achieved. These goals are fed into a metaknowledge base that acts as a comprehensive controller for the expert system. The metaknowledge base contains rules that define what tasks need to be done to accomplish the goals.[2] For the sequencing and grouping problem, the metaknowledge base might solve the problem by dividing it into the following tasks:

1. Arbitrarily assign impact areas to missions while ensuring that all target selection constraints are satisfied.

2. Resolve achievability problems without concern for activation time constraints but without violating impact selection constraints.

3. Satisfy activation time constraints without reducing achievability or violating impact selection constraints.

Just as several experts may use very different approaches to solve the same problem, the metaknowledge base can be designed to approach a problem in many different ways.

After the metaknowledge base has partitioned the problem into smaller tasks, the knowledge base is searched for explicit rules that will help achieve a given task. For example, several rules that will help make the missions achievable are:

1. If one impact area is closer to the center of a mission than any other impact area, then replace the farthest impact area with the closer impact area.

2. If a mission has crossing segments, then resequence the mission to eliminate the crossing segments.

3. If the mission is a long way from the launch facility, then assign the mission to another launch facility that is closer to the mission.

These rules will contain both fuzzy evaluations (note the terms *closer*, *farthest*, and *long*) and traditional yes/no evaluations such as *if the mission has crossing segments*. The knowledge base not only contains the rules, but will also contain filters that can be used to disallow certain conditions. Filters are used to satisfy impact selection constraints.

A rule that is selected from the knowledge base is sent to an inference engine. The inference engine will search the data base to

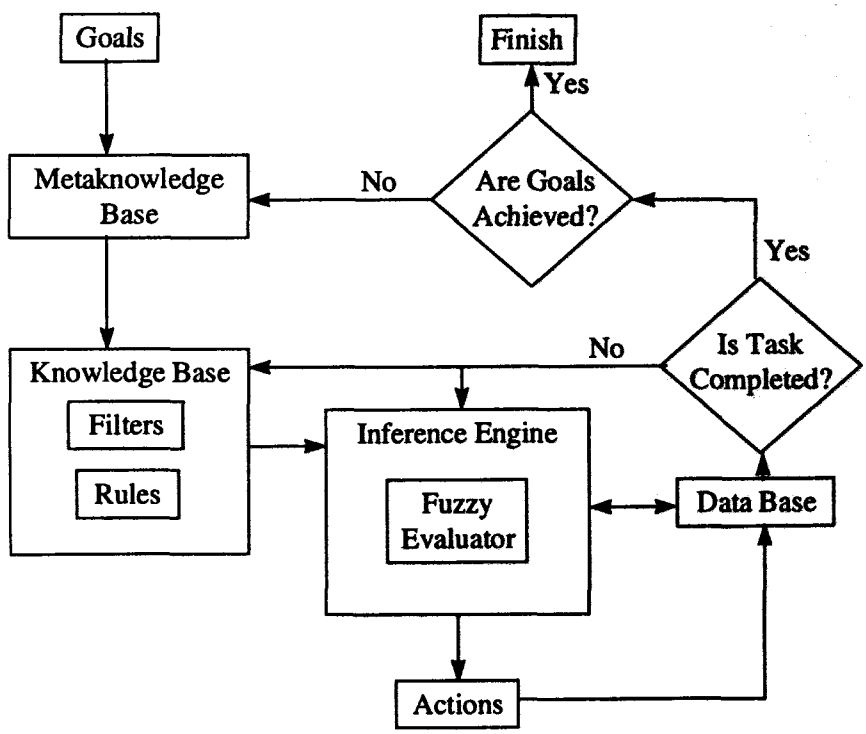

Figure 7—Expert System Flow Diagram

determine which elements (e.g., impacts, missions, launch facilities) match the conditional phrase that is in the rule. When a match is found, the appropriate action is taken, and the data base is updated accordingly. The rule is applied to other elements in the data base until no other elements match the conditional phrase of the rule. If the objective of the task is still not achieved, then another rule is selected from the knowledge base. After the task is achieved, or the task is determined to be unachievable, control returns to the metaknowledge base to determine which task should be worked on next.

An important factor to consider when building an expert system is to keep it as simple as possible. In everyday reasoning we do not perform complex calculations to reach decisions. Many complex problems can also be solved with a minimum of complex computations. A series of approximations or educated guesses should lead to a solution that meets most, if not all, of the criteria. At this point, it may be necessary to perform complex computations to verify that the solution works and to identify any areas that need improvement. For the sequencing and grouping problem, it is easy to visualize a human expert examining all the impact areas, launch facilities, and missiles. By drawing on experience, but not on complex models, he will assign missions to the missiles. A large number of factors may be used to decide which of many actions to take. After the expert feels confident in the solution, he will execute detailed simulations to verify the solution. If there are missions that need improvement, he will then attempt to refine them.

In addition to the above requirements, a well-designed fuzzy expert system should be able to quantify the goodness of the solution. For the mission planning problem, the fuzzy expert system should be able to specify which missions clearly satisfy all the goals, which clearly do not satisfy one or more of the goals, and which missions are in a gray area. The missions in the gray area are the only missions that need to be tested with detailed simulations. The goal of designing a fuzzy expert system is not to use fuzzy logic to reach an ambiguous solution, but to reach a solution that is clear and in which there is a high degree of confidence.

SUMMARY

Many of the advantages of fuzzy expert systems have been touched upon in this article. The work to design a fuzzy expert system to help solve the mission planning, sequencing, and grouping problems is just beginning. Tasks include identifying fuzzy variables and defining their categories, creating the tools to evaluate fuzzy logic, and deciding which rules work for this problem. There are many advanced concepts to fuzzy logic and expert systems that were not discussed in this article. Fuzzy expert systems have already been used in a wide range of applications from an automatic transmission system in the Saturn automobile[3] to traffic controllers in major cities.[4] This range of successful applications and the advantages that have been outlined indicate an excellent chance for a fuzzy expert system to help solve the mission planning problems.

REFERENCES

1. Klir, George J. and Yuan, Bo, *Fuzzy Sets and Fuzzy Logic, Theory and Applications*, Prentice Hall, Upper Saddle River, NJ, 1995, p. 222.

2. Parsaye, Kamran and Chignell, Mark, *Expert Systems For Experts*, John Wiley & Sons, New York, NY, 1988, p. 48.

3. Kosko, Bart and Isaka, Satoru, *Fuzzy Logic*, Scientific American, Jul 1993, p. 80.

4. McNeill, Daniel and Freiberger, Paul, *Fuzzy Logic*, Touchstone, New York, NY, 1993, p. 60.

THE AUTHOR

MR. PATRICK L. GODIN

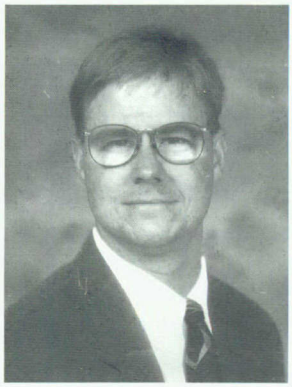

MR. PATRICK L. GODIN, an electronics engineer in the Strategic and Strike Systems Department since 1989, received a B.S. in physics in 1989 from Tennessee Technological University and an M.S. in electrical engineering in 1995 from Virginia Polytechnic Institute and State University. His career has focused on the fuzing systems and targeting aspects of ballistic missiles.

High-Altitude Electromagnetic Pulse (HEMP)

Dr. Ellen R. Brown and Dr. Barry Lee Bressler

High-altitude nuclear explosions produce, at lower altitudes, an intense pulse of radio-frequency radiation that is called a high-altitude electromagnetic pulse (HEMP). The Systems and Environment Analysis Branch has developed a fast first-principles code, called the Electromagnetic Pulse Generator (EMPGEN) code, that uses an exponential finite-difference technique to compute the electric fields due to HEMP. The purposes of this article are to discuss the reasons HEMP is of interest in military systems and to explain the physical concepts underlying the EMPGEN code.

Introduction

A nuclear explosion that occurs at a high altitude (generally specified in the literature as being above approximately 30 km) can produce gamma rays and X rays that interact with the atmosphere at lower altitudes.[1] At altitudes below the burst, such an interaction generates an intense pulse of radio-frequency radiation that is called a HEMP. HEMP, as opposed to other forms of electromagnetic pulse (EMP), is of particular interest because its associated electric fields cover a wide geographical area. HEMP is of very short duration and, like other forms of EMP, it can have negative effects on electrical equipment.

The military has been aware of the detrimental effect of EMP on equipment since the early nuclear testing, which began in 1945. In order to study these effects, the Systems and Environment Analysis Branch at the Naval Surface Warfare Center, Dahlgren Division (NSWCDD) tailored information available in the literature and developed the EMPGEN code, which calculates electric fields at user-selected altitudes below the burst. This code, and a collateral code that provides contour plots of the electric fields, have been used to support targeting studies at NSWCDD.

Code Verification

An excellent method of verifying any scientific applications code, such as EMPGEN, is to compare the output directly with experimental data. Unfortunately, it is not possible to use this method of verification directly on EMPGEN. Experimental EMP data from high-altitude bursts were collected before the Limited Test Ban Treaty

was adopted in 1963. The experimental tests that involved atmospheric nuclear explosions were few, the data collected were sparse, and the quality of this data is subject to question because considerable amounts of data were lost. One reason for this loss of data was that the correct theory of EMP was not developed until 1963, so most of the experimental equipment in the early tests was not properly shielded and was often driven off-scale by the high electric fields produced by the EMP. The Defense Special Weapons Agency (DSWA), which is the interface between the Department of Energy (DOE) and the Department of Defense (DoD) for nuclear-related matters, has studied these data extensively. DSWA and its contractors have developed HEMP codes that have been verified using these data. The overall uncertainty in the size of their computed electric fields is a factor of two.[2]

The best empirical method for checking EMPGEN is to compare the electric fields it computes against those from HEMP codes that have been verified against the experimental data. To accomplish this comparison, EMPGEN has been exercised with a variety of heights of burst, burst latitudes, and burst longitudes. Given the aforementioned uncertainty, the electric fields computed from EMPGEN compare very favorably with the corresponding electric fields from DSWA's HEMP codes.

OVERVIEW OF THE PHYSICS OF HEMP

When a photon is absorbed by an atom, the photon disappears, and its energy excites the atom by putting an electron into a higher energy state. The momentum of the photon transfers to the atom. A photon may be energetic enough to remove an electron from an atom, thereby ionizing the atom. This process is called photoionization. If the energy of the photon exceeds the ionization potential of the atom for an electron in a particular energy state, the excess energy can appear as kinetic energy of the ejected electron, which then also carries some of the momentum from the photon.

The more energetic a photon is, the more apparent its particulate characteristics are. A very energetic photon (such as a gamma-ray photon) may, in a sense, ricochet from an atom. The photon may ionize the atom and impart significant kinetic energy to the ejected electron without being completely absorbed. It loses only part of its energy and emerges from the interaction as a less energetic photon. The photon may go on to interact with other atoms. This process is called Compton scattering to distinguish it from ordinary photoionization.

A nuclear explosion produces gamma rays that can ionize the air below the burst. The physical mechanism responsible for this is the relativistic Compton collision (see Figure 1), resulting in Compton scattering. At a Compton source, a gamma-ray photon ionizes an atom or molecule by ejecting with some velocity an electron, called a Compton electron. The principles of conservation of energy and momentum determine possible velocities of the Compton electrons. Compton electrons ejected by energetic gamma-ray photons have large kinetic energies; therefore, they move at nearly the speed of light. On average, they move away from the burst. Because of their large kinetic energies, the Compton electrons are able to ionize many atoms or molecules in their paths by ejecting other electrons, which are called secondary electrons; however, the energy transferred from a Compton electron to any one of the secondary electrons is not very large, so the secondary electrons typically do not have large velocities. Because of this, the secondary electrons initially give rise to a secondary electron number density, but not a secondary current density, and initially are not subject to the influence of magnetic fields. The secondary electrons do give rise to a secondary current density when they move under the influence of ambient electric fields, such as those resulting from the ionization and those associated with the electromagnetic pulse.

The Compton collisions leave positive ions and free electrons. The moving electrons form, on average, a radial electron current. These

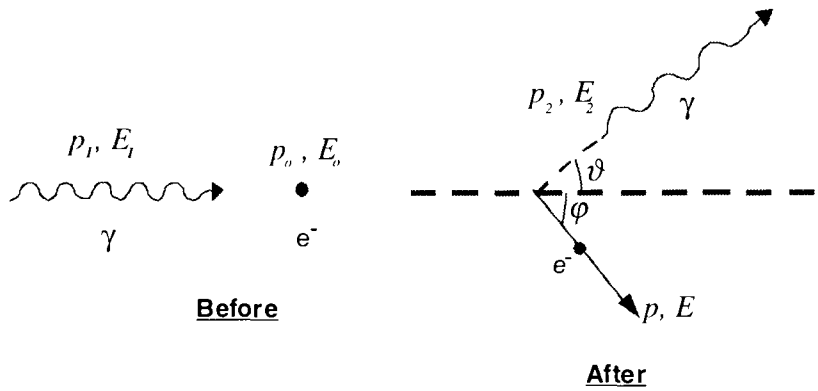

p_0 is the magnitude of the initial momentum of the electron
p_1 is the magnitude of the initial momentum of the gamma ray
p is the magnitude of the final momentum of the electron
p_2 is the magnitude of the final momentum of the gamma ray
E_0 is the initial energy of the electron
E_1 is the initial energy of the gamma ray
E is the final energy of the electron
E_2 is the final energy of the gamma ray

Figure 1—Relativistic Compton Effect

electrons travel at nearly the speed of light, so accurate modeling requires relativistic calculations. The Lorentz force describes the interaction of the electron current with the geomagnetic field. This interaction causes the electrons to begin to spiral about the imaginary geomagnetic lines of force, resulting in a current transverse to the radial direction from the burst (see Figure 2). Furthermore, an electric field produced by the separation between the electrons and the positive ions results in an opposing conduction current. The total current is the sum of the electron and conduction currents, which are functions of time and position. Maxwell's equations and the continuity equation determine the fields of the electromagnetic pulse in terms of the current density and the conductivity of the polarized air.

The forms of certain equations that describe these phenomena are dependent on the choice of a unit system. The mks unit system is presumed throughout the present document.

ENERGY SPECTRUM

There is a spectrum of quantum energies released during the burst. These energies are predominantly in the gamma-ray energy range. X rays are also produced. If the observed electric fields are below 30 km, the X rays are often ignored when computing HEMP because the EMP the X rays produce is attenuated before it reaches the observer.[3] X-ray photoionization is not accounted for in EMPGEN.

Practical considerations for a code such as EMPGEN require that the energy spectrum be represented by discrete energy values such that each has a weighting factor to indicate relative importance of the energy within the spectrum. This is accomplished by discretizing the spectrum into several bins, with each bin spanning a range of energies and containing some fraction of the total number of photons, and by using the average energy of each bin.

COORDINATE SYSTEM

The computations are performed in the burst-centered coordinate system shown in Figure 3. This coordinate system is defined by the position vector $\vec{r}$ from the burst to an observer; the vector $\vec{h}$, which is directed along a line from the center of the earth to the burst point, and which extends from the surface of the earth to the burst; the angle θ between $\vec{r}$ and $\vec{h}$; and the azimuthal angle ϕ about $\vec{h}$. In the Northern Hemisphere, $\phi = 0$ points to the geographic North Pole. Angles θ and ϕ are called line-of-sight (LOS) angles.

An LOS extends from the burst point to an observation point and, along the way, passes through source points that contribute to the electromagnetic pulse. The magnitude and orientation of the geomagnetic field at a source point are obviously important. The source points lie in a source region specified by upper and lower bounds on altitude.

It is assumed that computations along a single LOS ray from burst to observer are sufficient to determine the electric field at a specific point on the earth's surface; i.e., there are no contributions from fields along nearby rays.[4] The initial pulse ionizes the air, and any path except the shortest has fields that are attenuated with respect to those from the shortest path. Also, it is assumed that off-axis rays do not contribute to the leading edge of the electric field, and that this edge is the most important part of the contribution. Thus, in EMPGEN all integrations in position are along the direction of $\vec{r}$. Analysis of the problem over a large geographical area is based on examining what happens along each of many lines of sight.

HIGH-FREQUENCY APPROXIMATION

Karzas and Latter[5] derived equations that model the electric field resulting from high-altitude nuclear bursts. Their equations were programmed into EMPGEN. Since EMP is due

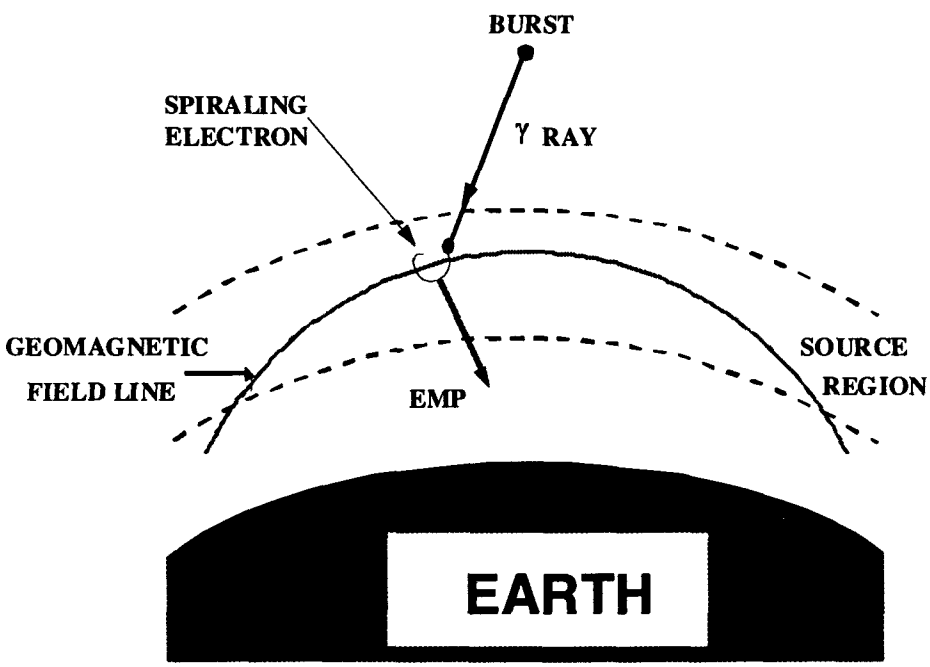

Figure 2—The Lorentz force causes electrons, ejected from atoms by gamma rays, to begin to spiral in the geomagnetic field, generating the EMP.

to the motion of Compton electrons, Karzas and Latter make the approximation that the EMP is produced by free charges, and that Maxwell's equations in a vacuum are appropriate. Their derivation combines Maxwell's equations in retarded time with the equation for the conservation of charge. An approximation is then made to eliminate terms that are small. This approximation is called the High-Frequency Approximation (HFA). It states that the spatial variation of the transverse currents (which are responsible for the radiation) is much slower than their variation with retarded time during the retarded times of interest. The HFA eliminates terms that require the evaluation of the Laplacian of the electric field $\vec{E}$ and the gradient of the atmospheric density ρ. The HFA is valid only for early-time EMP codes, such as EMPGEN, in which the time frame of interest is no longer than one microsecond. Other considerations apply at later times.[6]

MAXWELL'S EQUATIONS

In the burst-centered spherical polar coordinate system of Figure 3, the resulting equations for the components of the electric field $\vec{E}$ in the HFA are

$$\frac{\partial E_r}{\partial \tau} + \frac{\varsigma}{\varepsilon_o} E_r = -\frac{J_r}{\varepsilon_o},$$

$$\frac{\partial E_\theta'}{\partial r} + \frac{1}{2}\left(\frac{\mu_o}{\varepsilon_o}\right)^{1/2} \varsigma E_\theta' = -\frac{1}{2}\left(\frac{\mu_o}{\varepsilon_o}\right)^{1/2} J_\theta',$$

$$\frac{\partial E_\phi'}{\partial r} + \frac{1}{2}\left(\frac{\mu_o}{\varepsilon_o}\right)^{1/2} \varsigma E_\phi' = -\frac{1}{2}\left(\frac{\mu_o}{\varepsilon_o}\right)^{1/2} J_\phi',$$

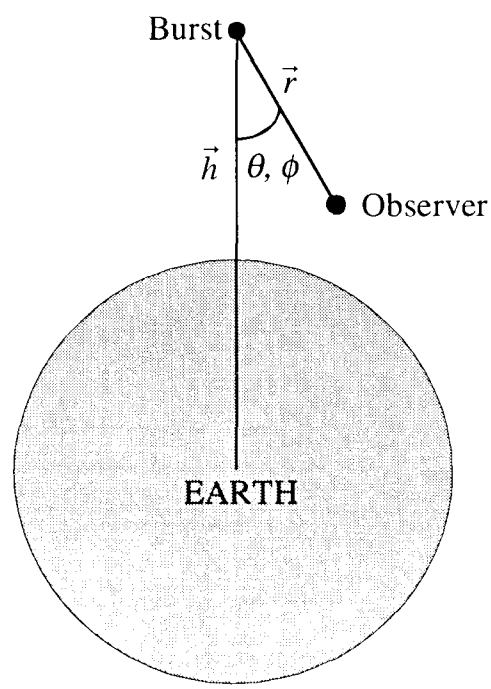

Figure 3—Burst-Centered Coordinate System Used in EMPGEN

where

$E_\theta' = r E_\theta$,

$E_\phi' = rE_\phi$,

E_r, E_θ, E_ϕ are components of the electric field $\vec{E}$ in the burst-centered coordinate system;

$J_\theta' = rJ_\theta$,

$J_\phi' = rJ_\phi$,

J_r, J_θ, J_ϕ are components of the Compton source current density $\vec{J}$ in the burst-centered coordinate system;

r is the distance from the burst to the electrons,

ς is the conductivity of air,

ε_o is the permittivity of free space,

μ_o is the permeability constant, and

τ is the relativistic retarded time $t - r/c$, where c is the vacuum speed of light.

METHOD OF SOLUTION

Before solving Maxwell's equations in the HFA, EMPGEN must determine the source current density $\vec{J}$ and conductivity ς (which is proportional to mobility μ and secondary electron number density N_e). The computation for $\vec{J}$ is more complicated than that for ς because different equations apply at the first time step than at subsequent time steps, as will be explained in the discussion below.

Solutions to the equations for $\vec{J}$ and ς require knowledge of the electric field $\vec{E}$ and electron velocity $\vec{v}$. Since the equations for $\vec{J}$, $\vec{E}$, and ς depend on time and position, there is indeed some circularity because the electric field must be known in order to compute the mobility, but mobility is required so the field equations can ultimately be solved for the electric field. Such equations are typically solved using self-consistent methods. To avoid that type of computation, the solution techniques used by EMPGEN substitute the electric field and velocity at the previous time step (for a fixed position) when computing $\vec{J}$, μ, and N_e at the current time step. EMPGEN computes $\vec{E}$ for all times at a single position before it begins computations at the next position along the LOS ray.

Computing the source current density involves two basic steps. First, EMPGEN presumes that there are Compton interactions at the first time step only, and that it must solve equations that relate source current density to physical quantities that can be measured and/or functionalized (e.g., energy and the geomagnetic field). EMPGEN performs the solutions using this assumption first. Then EMPGEN modifies the computed source current density to account for Compton interactions at time steps other than the first by using a mathematical technique called convolution. In the remainder of this article, the initial source current density is termed "unconvoluted source current density," and is symbolized by $\vec{j}$. The convoluted source current density required in Maxwell's equations is symbolized by $\vec{J}$.

The conductivity is dependent on an ionization rate, which is symbolized by Q. EMPGEN computes this rate in unconvoluted form first (symbolized by q), and then convolutes.

In the remainder of this article, if there is no reference to "convoluted" or "unconvoluted" when discussing source current density or ionization rate, the discussion applies to both.

Once $\vec{J}$ and ς have been computed, the equations for the components of the electric field are integrated using an exponential finite-difference technique to determine the maximum electric fields at a fixed position. The results can be plotted as contours. A sample

contour plot obtained using unclassified input data is provided in Figure 4.

PRESENTATION OF MATERIAL

The remainder of this article consists of two major sections that discuss equations used by EMPGEN to evaluate the source current density and the conductivity, respectively.

The evaluation of the source current density is discussed in the first major section. After several preliminary definitions are presented, the equation for the unconvoluted source current density $\vec{j}$ is given. The initial value for $\vec{j}$ is obtained by equations that are not used at time steps other than the first. An explanation of the initialization procedure is in a subsection titled "Special First Step." The second subsection presents the equation that must be integrated at time steps other than the first. Subsequent subsections explain how each term of that equation is evaluated, how the numerical solution is accomplished, and how the convolution is performed on $\vec{j}$ to obtain $\vec{J}$.

The discussion of the conductivity is in the second major section. That section presents the equation for the conductivity. Subsections explain the evaluation of the terms and of the convolution.

CURRENT DENSITY

Prior to computing $\vec{J}$, EMPGEN computes $\vec{j}$ at a particular position along the LOS ray for each time step. The expression for $\vec{j}$ is simpler in form if some preliminary definitions are made. First, define the so-called "penetration mass" as

$$M = \int_0^r \rho(r')\,dr',$$

where ρ is the density of air. The integral is evaluated from the top of the source region to the point where M is being computed. An approximate evaluation of this integral (as well as other details of HEMP physics) is available from Reference 7. The 1962 Standard Atmosphere is used for density computations.

If the burst produces isotropic radiation, the number density of Compton sources is

$$F = \frac{Y\rho\sigma_c \hat{e}^{-\sigma_t M}}{4\pi r^2 N_\vartheta N_\varphi},$$

where

- Y is gamma (g) yield in kilotons (input),
- σ_t is total cross section for gamma-ray scattering,
- σ_c is Compton cross section for gamma-ray scattering,
- ρ is air density,
- N_ϑ is the number of scattering angles formed by the radial axis and the electron path for which the differential Compton cross section is computed (input),
- N_φ is the number of azimuthal scattering angles for which the differential Compton cross section is computed (input), and
- r is the distance from the burst to the point at which $\vec{J}$ is computed.

In the equation for F, σ_t and σ_c are functions of these input gamma-ray energies. Numerical values can be obtained from References 8 through 11. The equation for F shows the inverse-square decrease with distance from the burst characteristic of isotropic radiation from a point source and the exponential decrease typical of propagation through a medium.

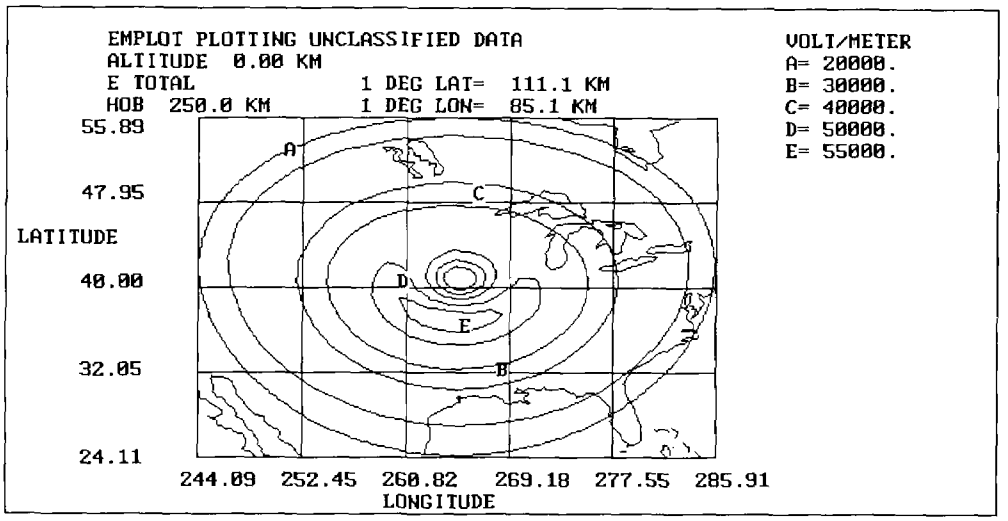

Figure 4—Sample Unclassified EMP Contours: outermost circle defines the earth's horizon as viewed from the burst point.

Next, define a variable

$$\left(\frac{dt}{d\tau}\right)_{ik} = \frac{1}{1 - \frac{\dot{r}_{ik}}{\eta c}},$$

where

c is the speed of light in a vacuum,

η is an obliquity factor to account for multiple scattering of Compton electrons along their trajectory, and

$\dot{r}_{ik}$ is the radial speed of the ith sample scattered electron in bin k.

The preceding definitions are used to express the unconvoluted current density at a particular location along the LOS ray as

$$\vec{j} = eF \sum_{k=1}^{N} W_k \sum_{i=1}^{N_\theta N_\varphi} \vec{v}_{ik} \left(\frac{dt}{d\tau}\right)_{ik}, \qquad (1)$$

where

N is the number of energy bins,

e is the electron charge,

$\vec{v}_{ik}$ is the velocity of the ith sample scattered electron in bin k, and

W_k is the weighting factor of the active electrons in energy bin k, determined by the fraction of total gamma-ray energy per kiloton that is in bin k.

Equation (1) is dependent on (retarded) time and position. None of the variables to the left of the second summation symbol depend on time. Within the second summation, the velocity and obliquity are dependent on time and position. The EMPGEN code performs computations at all time steps for a fixed position along the LOS ray. It then moves to the next position along the LOS ray and recomputes variables dependent on retarded time and position. Thus, values of $\vec{j}$ are obtained at each time step.

At a fixed position, the velocity $\vec{v}_{ik}$ in the summation of Equation (1) changes with time. The first time step is treated differently from the others. The first subsection that follows discusses the computation of $\vec{v}_{ik}$ at the first time step. The following several subsections discuss the propagation of that velocity in time and position. Since velocity is determined by dividing the electron momentum by the electron mass, the emphasis is on determining the applicable momentum. The final subsection in this group discusses convolution, which turns $\vec{j}$ into the $\vec{J}$ needed to solve Maxwell's Equations.

Special First Time Step

In early-time EMP codes, the electromagnetic radiation from Compton recoil electrons is considered to be coherent in the downward direction because the Compton current and associated field move together at nearly the speed of light. At the first time step, the obliquity factor η is set to unity. At this time step, the velocity of primary electrons is computed after evaluating relativistic equations for energy and momenta. The total relativistic momentum and its components in directions determined by r, θ, and ϕ are then computed. These computed momenta can be divided by the electron mass to get the initial values of velocity required to evaluate Equation (1).

There are many intermediate steps in the computational process for the momentum. Because the energy of a Compton electron is a function of scattering angle, the relativistic forms of the total Compton cross section for recoil electrons[12] must be computed. In addition, the Klein-Nishina equation,[13] which gives the relativistic differential Compton cross section for recoil electrons, must be integrated. All of these equations are independent of the position of the electrons along the LOS ray. Thus, EMPGEN uses the same velocity (and momentum) at the first time step for each position along the LOS ray.

Velocity

After the first time step, Compton electrons begin to spiral about the imaginary lines of the geomagnetic field. The velocity needed to evaluate Equation (1) is determined from integrating the Lorentz equation for the force on an electron in an electromagnetic field to get momentum, then dividing by mass to get velocity. The Lorentz equation is

$$\frac{d\vec{p}}{d\tau} = \left(\frac{dt}{d\tau}\right)\left\{e(\vec{v} \times \vec{B}_g) - \frac{d\varepsilon}{d\ell}\frac{\vec{p}}{p}\right\}, \qquad (2)$$

where

$\vec{p}$ is the scattered sample electron momentum,

p is the magnitude of the sample electron momentum,

e is the electron charge,

$\vec{v}$ is the sample electron velocity,

$\vec{B}_g$ is the geomagnetic field, and

$\frac{d\varepsilon}{d\ell}$ is the energy change per unit path length as the electrons travel through the air.

The gravitational force on a Compton electron is omitted from Equation (2) because this force has a negligible effect on the trajectory of an electron during the short interval of time in which the electron has significant motion. Any apparent forces that appear when the Compton process is described in a moving earth-fixed reference frame rather than in an inertial frame are also negligible for the same reason.

A more general form of Equation (2) could be implemented, but that would require a self-consistent calculation. Reference 4 confirms that

the effects of self-consistency are minor in calculations of this type. The neglected fields have little effect on the high-energy Compton electrons produced by gamma-ray photons. Fully self-consistent calculations would take account of the effects of these fields on the subsequent motion of the electrons. EMPGEN contains the form shown for Equation (2).

Before Equation (2) can be evaluated, $\frac{d\varepsilon}{d\ell}$, η, and $\vec{B}_g$ must first be determined, and decisions must be made about which time to use for $\vec{p}$ and $\vec{v}$ on the right-hand side of Equation (2). The following subsections address these issues.

Energy Loss Per Unit Path Length

The relativistic primary electrons that emanate from the burst lose energy as they travel through the atmosphere. The primary process responsible for this energy loss is collision with air molecules. The paths that the electrons follow are complicated because of the dynamics of the collisions. Another consideration is that linear penetration distance can be quite different from the distance along the electron's actual path. In addition, the mathematics involved is complicated by questions about energy transfer during collisions, and differentiating between incident and target electrons. The Nobel laureate Hans Bethe derived a formula that expresses the energy loss per unit path length $\frac{d\varepsilon}{d\ell}$ suffered due to collisions by relativistic electrons. This expression, which is discussed in more detail in References 14 through 17, is used in EMPGEN.

Obliquity Factor

In order to approximate mean electron velocities, the multiple scattering experienced by the Compton electrons along their trajectory is included. This effect, which is represented by the obliquity factor η, has been formulated by Longmire and Longley.[14, 18]

Geomagnetic Field

Evaluation of Equation (2) requires that the earth's magnetic field $\vec{B}_g$ be known. In EMPGEN, this field is computed using Legendre polynomials, as in Reference 19. Components of this field are initially computed in an Up, South, East coordinate frame. They are subsequently rotated to the burst-centered frame in which the electric field is computed.

Numerical Solution Technique for Velocity

The right-hand side of Equation (2) is nonlinear due to relativistic and obliquity corrections. To avoid computational problems that result from this nonlinearity, these corrections are treated as constant and are numerically evaluated by substituting momentum and energy at the previous time step into Equation (2) for $\frac{d\varepsilon}{d\ell}/p$. The initial value for η is 1. Thereafter, Equation (2) is integrated in time.

Two alternate methods have been implemented to solve Equation (2) numerically. One method is a finite-difference method. A second method uses a linearized version of the trapezoidal approximation. Both methods are described in detail in Reference 20. The method actually used by EMPGEN is chosen by the user on input. Most often, the finite-difference method is used when many points must be evaluated because of its relatively speedy execution time. More detail is available in Reference 21.

Convolution

The presumption inherent so far in the discussion about the computation of the source current at a fixed position has been that for each bin, there is only one Compton interaction, which occurs at the first time step, and that subsequent time evolution of the momentum depends only on $\vec{v}$ and η. This is

equivalent to presuming that no additional Compton interactions take place; i.e., that the current density is like a delta function.

It is more physically realistic to assume that additional Compton interactions can occur at time steps other than the first. Instead of computing each of these individually, they can be accounted for by performing a convolution of $\vec{j}(\tau)$ with a time-dependent weapon output rate $\dot{\gamma}$ (i.e., the rate of gamma-ray production). The weapon output rate $\dot{\gamma}(\tau)$ may be defined using an algebraic equation or tabular values that are functions of time. The convoluted current density is expressed as

$$\vec{J}(r,\tau) = \int_{-\infty}^{\infty} \vec{j}(r,\tau')\dot{\gamma}(\tau-\tau')\,d\tau'.$$

CONDUCTIVITY

The equation to compute the conductivity, ς, is given in Reference 22 as

$$\varsigma = e\mu_e N_e,$$

where

e is the electronic charge,

μ_e is the electron mobility, and

N_e is the secondary electron number density.

Electron Mobility

The mobility μ_e of the secondary electrons functionally depends on the ambient electric field.[18,23] Since the value of the electric field is not actually known at the time and position that μ_e is to be calculated (i.e., the calculation is not self-consistent), the electric field is approximated by using the value computed at the same position for the previous time step.

Secondary Electron Number Density

The secondary electron number density N_e can be determined by evaluating

$$\frac{dN_e}{d\tau} + \beta_a N_e = Q + \beta_c N_e, \qquad (3)$$

where

β_a is the attachment coefficient (electrons to neutrals),

Q is the ionization rate, and

β_c is the avalanche rate.

The coefficients β_a and β_c depend on the relative air density and the magnitude of the ambient electric field.[24,25] At a fixed position, relative air density is known. The differential equation governing N_e, Equation (3), is evaluated by using an exponential finite-difference technique. A nonzero initial N_e may exist as a result of previous ionization.

Convolution

The formula for the ionization rate Q in Equation (3), is very similar to that for $\vec{J}$. The unconvoluted q is evaluated according to

$$q(r,\tau) = F\sum_{k=1}^{N} W_k \sum_{i=1}^{N_\theta N_\varphi} v_{ik}\left(\frac{dt}{d\tau}\right)_{ik} K\left(\frac{d\varepsilon}{dl}\right)_{ik}, \qquad (4)$$

where variable definitions in Equations (1) and (2) are applicable, except that v_{ik} is the speed (not the vector velocity) of the ith sample scattered electron in bin k, and K converts joules to ion pairs. The time dependence of q is

handled precisely like that for $\vec{J}$; the discussion of the total q as involving a summation over the bins, the method of solving the first time step and subsequent time steps, and the convolution from q to Q, applies here as it did for $\vec{J}$.

SUMMARY

The HEMP produced by high-altitude nuclear explosions is important to the military because of the negative effects that the intense pulse of radio-frequency radiation produces on electrical equipment over a wide geographical area. To calculate the electric fields due to HEMP, the Systems and Analysis Branch at NSWCDD developed the EMPGEN code.

EMPGEN uses a special approximation to Maxwell's equations, known as the HFA, to compute the electric field caused by the HEMP. Computations are performed in a spherical polar coordinate system, and require that the Compton source current density and the conductivity of air be computed. The computations are dependent on time and position. The physical mechanisms that cause EMP occur so rapidly that Einstein's theory of special relativity is used in EMPGEN. In addition, physical phenomena such as the geomagnetic field, electron mobility, and secondary electron number density are calculated. Convolution with the time-dependent weapons output rate is performed to increase the realism of the calculations.

EMPGEN calculates electric fields at user-selected altitudes below the burst. The results may be output either in the form of electric field strengths at specific locations or in the form of contour plots. Electric field strengths computed from EMPGEN compare favorably with those computed from other HEMP codes.

REFERENCES

1. *Effects of Nuclear Weapons*, edited by S. Glasstone and P. Dolan, U.S. Department of Defense and U.S. Department of Energy, 3rd ed., 1977.

2. Makoff, G. and Tsipis, K., *The Nuclear Electromagnetic Pulse*, M.I.T. Report #19, Mar 1988.

3. Higgins, D.F. et al., *A Method for Estimating the X-Ray Produced Electromagnetic Pulse Observed in the Source Region of a High Altitude Burst*, written for Defense Nuclear Agency by Mission Research Corporation, AD-774 152, 29 Nov 1973.

4. *EMP Interaction: Principles, Techniques, and Reference Data*, edited by K.S.H. Lee, Springer Verlag, 1986.

5. Karzas, W.J. and Latter, R., *Phys. Rev.* B137(5B), p. B1369.

6. Cottage, K.S.; Simpson, L.T.; and Page, W.E., *Early to Intermediate Time High-Altitude Electromagnetic Pulse Calibrations*, written for Air Force Materiel Command by Mission Research Corporation, Oct 1993.

7. Bressler, Barry Lee, *HEMP Concepts: An Analysts's Guide to a Formulation Describing the High-Altitude Electromagnetic Pulse*, prepared for NSWCDD by EG&G WASC, revised Sep 1997.

8. Hubbell, John H. et al., *J. Phys. Chem. Ref. Data*, Vol. 9, No. 4, 1980.

9. Hubbell, John H. et al., *J. Phys. Chem. Ref. Data*, Vol. 4, No. 3, 1975.

10. Hubbell, J.H., *Int. J. Appl. Radiat. Isot.*, Vol. 33, 1982.

11. Berger, M.J. and Hubbell, J.H., *XCOM: Photon Cross Sections on a Personal Computer*, Jul 1987.

12. Segre, E., *Nuclei and Particles*, 2nd ed., Benjamin/Cummings Publication Company, 1977.

13. Heitler, W., *The Quantum Theory of Radiation*, 3rd ed., Oxford University Press, Oxford, 1954.

14. Longmire, Conrad L., *Improvements in the Treatment of Compton Current and Air Conductivity in EMP Problems*, written for Defense Nuclear Agency by Mission Research Corporation, AD-769 914, 25 Sep 1973.

15. Bethe, H.A. and Ashkin, J., "Passage of Radiation Through Matter," *Experimental Nuclear Physics*, Vol. I, edited by E. Segre, Wiley, 1953.

16. Krane, Kenneth S., *Introductory Nuclear Physics*, John Wiley and Sons, NY, 1988.

17. Arya, Atam P., *Fundamentals of Nuclear Physics*, Allyn and Bacon, Inc., Boston, 1966.

18. Longley, H.J. and Longmire, C.L., *Development of the CHAP EMP Code*, Mission Research Corporation, MRC-R-3, DNA 3150T, 7 Nov 1973.

19. *Air Force Geophysical Laboratory Handbook*, Chapter 4.

20. Brown, E., "Notes on EMPGEN and EMPLOT," informal notes provided to NSWCDD by EG&G, Dahlgren, VA.

21. Brown, E., *User's Manual for EMPGEN, EMPLOT and EMPMENU (Version 3.0), and EMPET (Version 2.0)*, EG&G, Dahlgren, VA, Sep 1992.

22. Karzas, W.J. and Latter, R., "The Electromagnetic Signal Due to The Interaction of Nuclear Explosions with the Earth's Magnetic Field," *Journal of Geophysical Research*, Vol. 67, No. 12, 1962.

23. Baum, C.E., *Electron Thermalization and Mobility in Air*, Air Force Weapons Lab, EMP Theoretical Note 12, Kirtland AFB, NM, 1965.

24. Longley, H.J. and Longmire, C.L., *Electron Mobility and Attachment Rate in Moist Air*, Mission Research Corp., MRC-N-222, 1975.

25. Jones, C.W., *Electron-Ion and Ion-Ion Recombination Coefficients for Use in EMP Radiation Codes*, Air Force Weapons Lab, AFWL-TR-78-221, Kirtland AFB, NM, 1977.

THE AUTHORS

DR. ELLEN R. BROWN

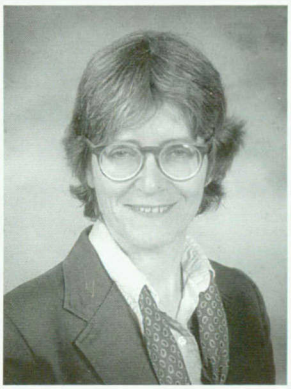

DR. ELLEN R. BROWN received a B.S. in physics from Mary Washington College in 1969, an M.S. in physics from the Pennsylvania State University in 1971, and a Ph.D. in physics from the University of Virginia in 1981. Several articles based on her academic research on energy-band bending in semiconductors and on photoionization of open-shell atoms were published in respected peer-reviewed physics journals such as *Surface Science*, *Physical Review*, and *Physics Letters B*. She has supported the Submarine Launched Ballistic Missile (SLBM) program since 1979 as an employee of EG&G and, more recently, NSWCDD. During that time she has performed technical and liaison efforts in support of studies on atmospheric dispersion of starlight, SLBM fuzing, effects of weather on reentry (including erosion and ablation of reentry vehicles), EMP simulation, energy technology transfer, and missile engagement analysis. For several years she also served as the Head of the Analysis and Evaluation Department at EG&G. She is a member of The American Physical Society and the International Radiation Physics Society, and an elected member of Sigma Xi, the Honorary Science Fraternity.

DR. BARRY LEE BRESSLER

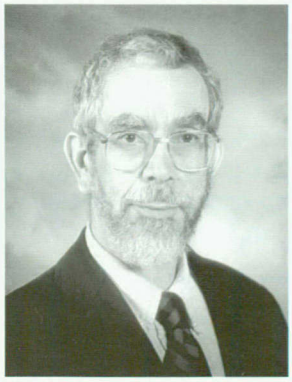

DR. BARRY LEE BRESSLER received a B.S. in physics in 1957 from Ursinus College, and an M.S. and a Ph.D. in physics, in 1979 and 1986, respectively, from Virginia Polytechnic Institute and State University, where he is an adjunct professor. He completed the required residency with the support of the NSWCDD full-time, advanced-study program. After joining NSWCDD in 1958, he participated primarily in the SLBM program by working on the modeling of ballistic missiles, the simulation of maneuvering reentry vehicles, threat analysis, and the physics of weapons effects. He also served for several years as a group leader for the analysis of advanced strategic systems. Since his retirement from NSWCDD in 1994, he has continued to contribute to the SLBM program as a part-time employee of EG&G WASC. He is a member of the American Physical Society, and an elected member of Sigma Pi Sigma and Sigma Xi.

Developing Software for a Distributed, Synchronous, Real-Time System

Mr. E. Augustus Cooper, Jr., and Mr. A. Lee Philpott, Jr.

The submarine launched ballistic missile (SLBM) system has been a key element in U.S. national defense for nearly 40 years, and the Naval Surface Warfare Center, Dahlgren Division (NSWCDD) has been a major contributor to its success from the beginning of the program. The SLBM Program, like all defense programs, is evolving in an environment that includes budget constraints and changes in world situation and system design. To meet the demands of the 21st century, the SLBM Fire-Control Life-Cycle Cost Control (LCCC) Program is changing the fire-control system (FCS) from a centralized, point-to-point system of SLBM-developed hardware and software to a distributed, networked system containing a mixture of nondevelopmental items (NDI), commercial off-the-shelf (COTS), and SLBM-developed hardware and software. This article describes the architecture of the SLBM fire-control, real-time software and its evolution to a distributed system.

Introduction

The SLBM system has been an important cog in U.S. national defense for nearly 40 years, and NSWCDD has been a major contributor to its success from the beginning of the program.[1] NSWCDD has experienced the evolution of the SLBM system from its initial capabilities to its current features and is part of a program that will prepare the SLBM system for the 21st century. The SLBM Fire-Control LCCC Program is changing the FCS from a centralized, point-to-point system of SLBM-developed hardware and software to a distributed, networked system containing a mixture of NDI, COTS, and SLBM-developed hardware and software.

This article describes the architecture of the SLBM fire-control prelaunch software and its evolution from a centralized system to a distributed system. The fire-control prelaunch software satisfies the same real-time requirements in both the centralized and distributed systems; yet communication in the distributed system is designed over a commercial operating system (OS) using standard internet protocols. This article shows how the incorporation of a commercial OS supporting network access can be used to solve a distributed, real-time problem.

The FCS, as described in this article, has been simplified in places for brevity and simplicity. For example, redundant equipment and multiple missile communications are omitted.

PROBLEM DEFINITION

The SLBM shipboard subsystems prepare and launch missiles that contain a guidance system, a flight-control system, and multiple independently targeted reentry bodies. Once the missile is launched, the guidance and flight-control systems steer the missile so that it releases the reentry bodies at the position and velocity required to fly on a ballistic trajectory to the desired impact points. The FCS participates in the preparation of the missiles before launch. It performs three major tasks: system maintenance, targeting, and launch sequence-related computations and control. System maintenance is ongoing, non-real-time work prior to the launch sequence. It is intended to ensure that the system is operational. Targeting tasks, which are also non-real-time, include the updating of targeting information in the mission data base by FCS operators and the assignment of targets to missiles. The prelaunch FCS software, under operator control,

- Computes missile targeting and steering data.
- Prepares the missile inertial guidance system for flight through a process that includes the continuous exchange of information among the guidance system, the FCS, and other weapon-system components.
- Coordinates the events associated with launching the missile.

The FCS is being modernized to prepare it to meet future requirements and to reduce life-cycle costs by replacing expensive obsolete components. The prelaunch software, however, must satisfy the same communication requirements in the distributed system as it does in the centralized one. Figure 1 depicts the major components that participate in prelaunch communication. The periodic communication between these components is synchronous since they all receive 1-pulse-per-second (1PPS) signals that allow the coordination of the exchange of information at timing marks within the 1PPS interval. The guidance system, for example, can require that the FCS transmit a specific data list at a defined mark after the 1PPS signal. The 8PPS (one pulse per 0.125 seconds) and the 2PPS (one pulse every half second) periods exist synchronously with the 1PPS for the purpose of computing prelaunch communication (see Figure 2). Within each period, the FCS software establishes timing marks as reference points for performing computations and communication.

Several examples of communications performed by the FCS are developed in order to allow comparison of the centralized and distributed architectures. These examples are communication with the Operators Control Panel (OCP), the submarine navigation system, and the missile guidance system.

Example 1: OCP Communication

The OCP reads operator selections, provides the status of various systems, and maintains important system-state information. It receives and displays this information using a collection of color-coded actuator/indicators (*buttons*) and lights. The OCP receives information from the operator, FCS applications, and other weapon-system elements. All operator input and output are predefined. This allows the input and output lists to be of a fixed length, and sent and received synchronously on a specified timing mark. System-state information is a set of variables (*state terms*), some of which are examined by applications to determine the current state (*state input terms*), while some are assigned values by applications to indicate their state (*state output terms*). OCP communication requires reading input associated with operator selections, determining system state by executing logical equations, and updating operator display status using the output of these equations.

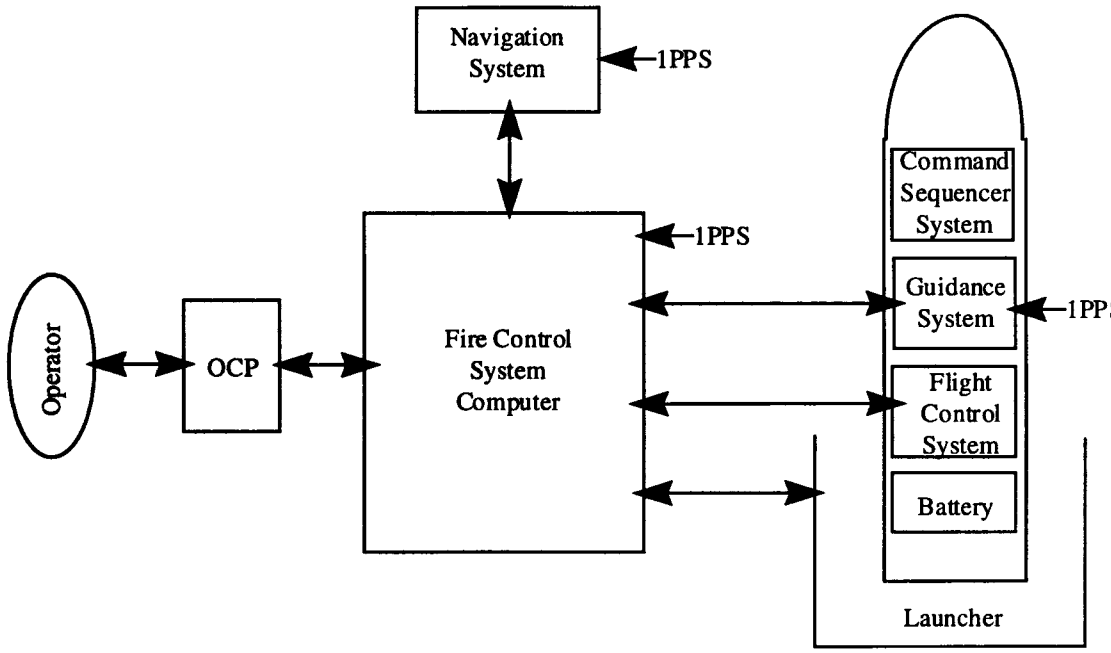

Figure 1—Major Components of a Prelaunch Sequence

Example 2: Navigation Communication

Navigation communication requires the reading of information from the ship's navigation system (e.g., position and velocity) and conversion to FCS formats. This is done at a specified interval.

Example 3: Guidance Communication

There are many types of communication between fire control and guidance. This article specifically considers two: communication of position data to guidance and status communication from guidance. These are performed at a specified interval and require computing guidance position data based on navigation inputs, writing these data to guidance, reading status data from guidance, and computing guidance status as required for the OCP logical equations.

CENTRALIZED AND DISTRIBUTED FCS

In a centralized system, the FCS computer is connected to the other systems by point-to-point connections, as shown in Figure 3. All of the launch-sequence-related, targeting, and system-maintenance software executes on the FCS computer. The current computer, which is of 1970s vintage, was designed specifically for the FCS and includes one megabyte of main memory; 32-bit, fixed-length instructions; 16-bit virtual addresses, specialized real-number support for computations, several Programmable Interrupt Generators (PIG), and a programmable Direct Memory Access (DMA) input/output controller for interfacing the FCS to other systems.

In a distributed system, the FCS software executes in multiple computational nodes connected by a network (see Figure 4). The FCS

in this figure includes the OCP for controlling the launch sequence; the Display and Control Subsystem (DCSS), the Enhanced Guidance Interface Subsystem (EGISS), the Navigation/ Missile Interface Subsystem (NMISS), and the Data Entry Subsystem (DESS) for controlling targeting and system maintenance software; and the Fiber-Distributed Data Interface (FDDI) network. What was previously computed in one computer is now computed in a networked environment. The primary computing nodes for the three examples are the DCSS, the EGISS, and the NMISS. Each node is Versa Module Eurocard (VME)-based and has components as shown in Figure 5. The fire-control software executes in the commercial PowerPC module; the commercial FDDI module provides access to the network; and the specialized Input/ Output (I/O) module provides access to SLBM components, such as the guidance and navigation systems, and the OCP.

Both the centralized and distributed FCS establish the timing marks discussed previously; however, each does it differently. The reason for the difference can be discovered by examining the communication of each FCS architecture.

Communication in the centralized FCS is performed by software executing in the one computer using its DMA controller. The DMA is programmable in a simplistic, but powerful way. Each port can have a "chain" of operations ongoing, where each operation in the chain is an output of data or commands, an input of data or commands, or a skip of the next operation. Beginning the chain requires a single Central Processing Unit (CPU) instruction to start I/O with the address of the chain. Starting I/O requires so little overhead from the CPU that it can be performed at the interrupt level. Thus, the OS of the centralized FCS establishes a system-wide set of timing marks, each with a corresponding connect point for an interrupt handler. This allows applications to connect interrupt handlers to the timing marks. The timing marks are established by using a PIG in conjunction with the 1PPS signal. When a 1PPS interrupt is received, a PIG is set up to generate an interrupt—for example, 65 milliseconds later and every 125 milliseconds thereafter. This sequence would result in interrupts at the 65-, 190-, 315-, 440-, 565-, 690-, 815-, and 940-millisecond marks. At each of these points, the OS would call the connected interrupt handler to consider sending position data to the guidance system. The prelaunch software builds the chain prior to the timing mark, and the interrupt handler starts the I/O at the proper time.

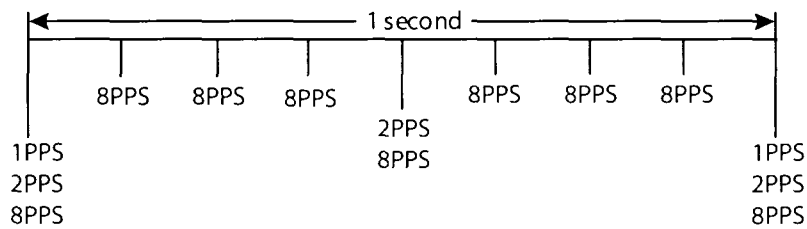

Figure 2—Timing Marks

Communication in the distributed FCS is performed by software executing in the various nodes on the network. This communication is a

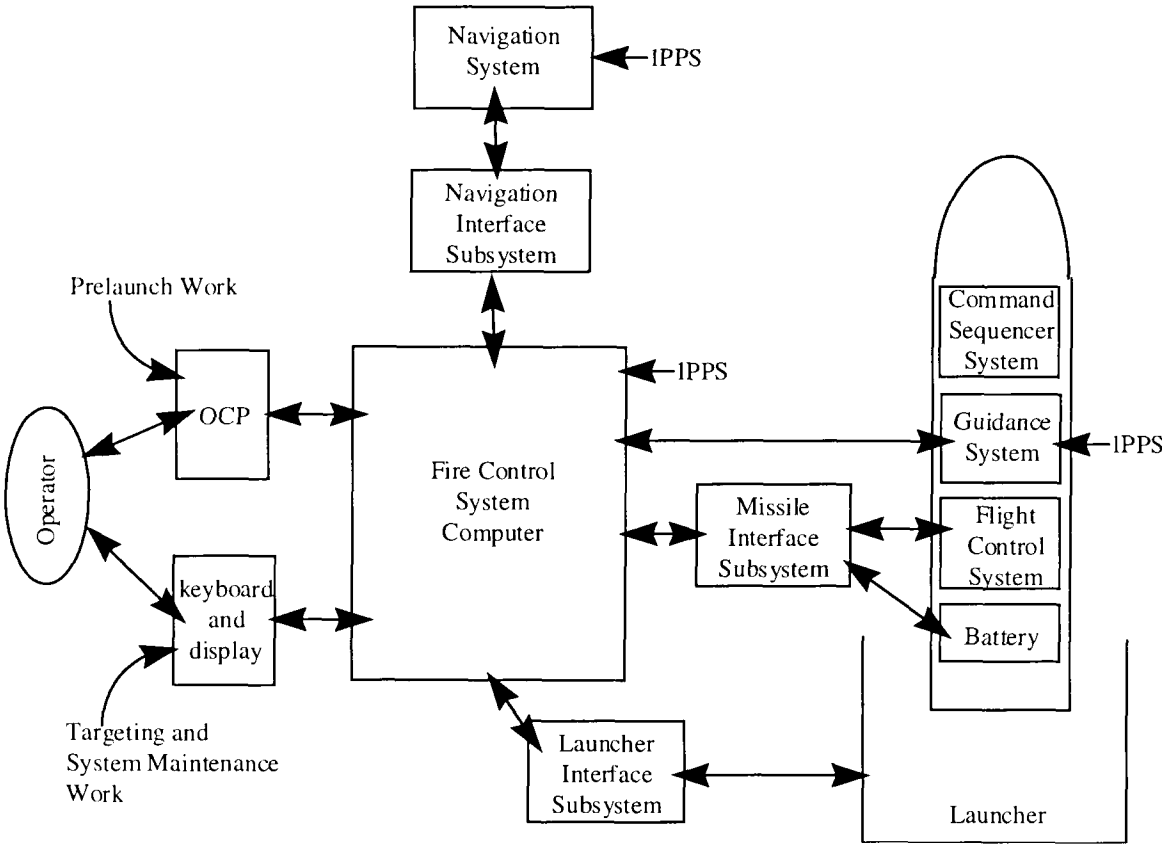

Figure 3—Centralized SLBM System

combination of network I/O and I/O using specialized ports. The commercial OS has changed the nature of I/O. The Berkeley Networking functions,[2] as well as the manner in which the specialized I/O device drivers are added to the commercial OS, require tasks (or processes) to initiate the I/O. It cannot be initiated at the interrupt level. Thus, the OS of the distributed FCS must establish a mechanism for providing timing marks to tasks. Additionally, it is not known which set of timing marks each node requires, and as a consequence, a more general mechanism is established for defining the timing marks.

For example, when a 1PPS interrupt is received in a node, a PIG is set up to generate an interrupt every 125 milliseconds thereafter (that is, at the 0-, 125-, 250-, 375-, 500-, 625-, 750-, and 875-millisecond marks). These interrupts are handled by the OS and are not passed on to application interrupt handlers. Instead, the OS allows tasks to be awakened at any millisecond marks within a 125-millisecond interval. The OS in a node maintains a data structure that describes all timing mark events established within that node. When the 125-millisecond interrupt occurs, the OS consults the data structure to determine whether any task must be awakened in the interval and, if so, when. For example, assume two tasks are to be awakened in a given interval—the first at 40 milliseconds after the interrupt and the second at 82 milliseconds. The OS establishes a second PIG to count 40 milliseconds and generate an interrupt. After the interrupt is handled by the

OS, it establishes the same second PIG to count 42 seconds, and then performs the processing for the second task.

COMPARISON OF COMMUNICATION EXAMPLES

Four examples of FCS communications were selected for specific discussion. They serve to further highlight the differences between the centralized and distributed FCS architectures. The OCP and navigation examples address the provision of system services; the guidance example considers continuous communication with a system outside of fire control.

Example 1: OCP Communication

In both the centralized and distributed FCS, the OS provides OCP communication and system-state computation as a service. In the centralized FCS, OCP communication provides one of the system timing marks. For example, the 1PPS and a PIG are used, as previously described, to establish a timing mark. The OS uses the DMA to write and read values to and from the OCP. The initial DMA program outputs a default set of values for the OCP and reads the results from the OCP. This read, which should be complete by the timing mark, is followed by the execution (by the OS) of the system-state logical equations using the input data to generate OCP output data and the

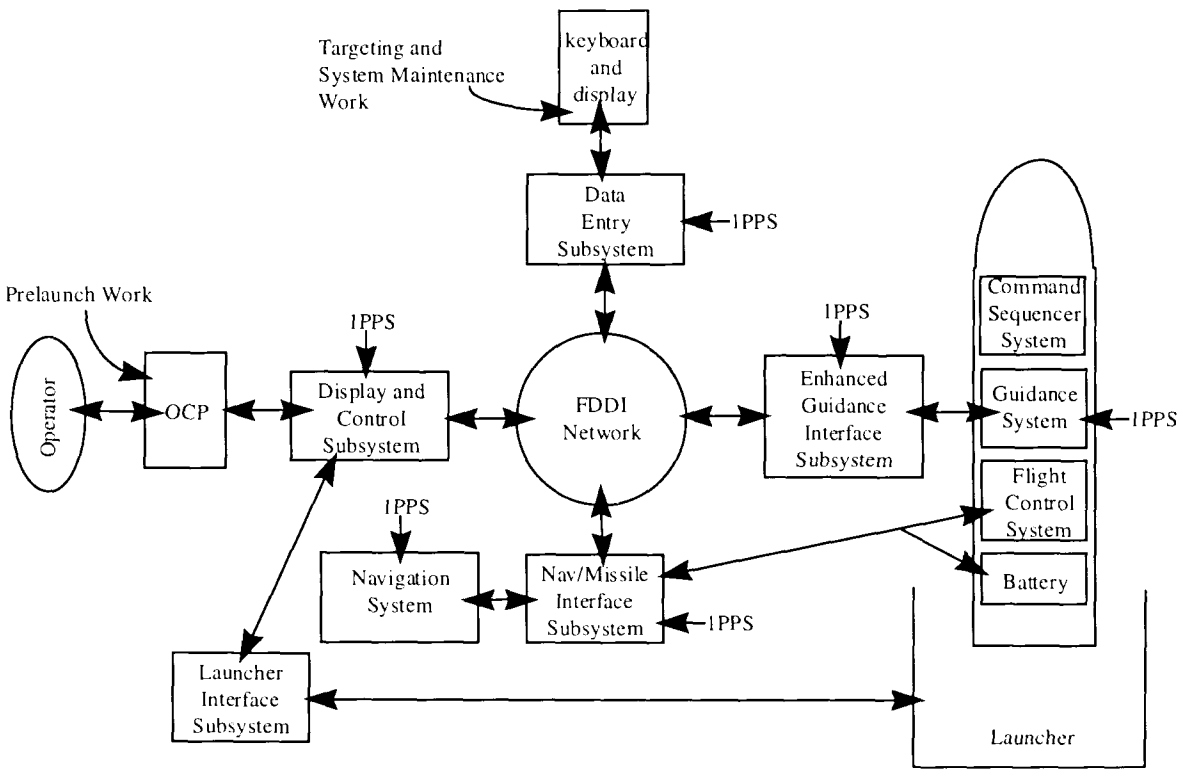

Figure 4—Distributed SLBM System

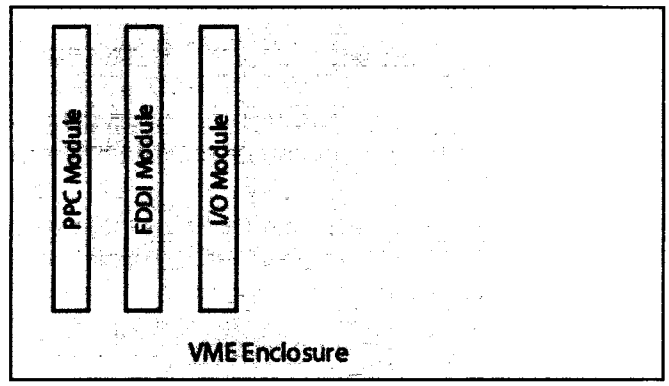

Figure 5—Fire Control Computing Node

restarting of the DMA program. This process is repeated at the remaining millisecond marks.

Since OCP communication involves the computation of system-state information, the OS provides two interrupt-level connect points that allow applications immediate access to the system-state information and precise timing marks. At the first connect point, the OS calls an application interrupt handler just prior to the computation of the system-state logical equations. The OS calls an application interrupt handler, at the second connect point, just after the system-state logical equation computation. The system-state information is contained in memory that is accessible to applications.

In the distributed FCS, the OCP communication provides one of the system timing marks, but it does it in a different manner. OCP communication and system-state computation are done in the DCSS node; applications execute in other nodes. Targeting applications, for example, execute in a DESS node, and the launch-sequence computations and control execute in the EGISS nodes. These applications require access to fire-control information. For example, the prelaunch software needs to know when a launch has been commanded and requires the ability to change system status information when elements (such as guidance) are bad or not available.

Fire-control information is computed in the DCSS node and broadcast on the FDDI network to all other nodes. Each node computes its own system status information and sends it on the FDDI network to the DCSS node. Thus, the OCP communication timing marks provided in the distributed FCS are those used when the fire-control information is received in a node. The OS in a given node uses its own timing mark mechanisms to establish the mark at which broadcast fire-control information is required in the node. An OS task is awakened at that point to perform a nonblocking network read to receive the broadcast fire-control information. The OS task then calls an application connect handler in the context of the task that performed the read, not as an interrupt.

Example 2: Navigation Communication

In both the centralized and distributed FCS, the OS provides the navigation communication and data computation as a service. They are provided in a manner similar to that of OCP communication and fire-control computation.

Navigation communication provides one of the system timing marks in the centralized system. The 1PPS interrupt and a PIG are used to establish two timing marks (different from

those provided by OCP communication). The OS interrupt handler, operating at these times, reads navigation data, converts it to fire-control format, and provides a connect point that allows an application interrupt handler to be called. The navigation data are contained in memory that is accessible to applications. The prelaunch sequence application uses this connect point to be notified when navigation data are available.

In the distributed FCS, navigation communication again provides one of the system timing marks. Navigation communication and data computation are performed in the NMISS node. The NMISS software broadcasts navigation data on the FDDI network to make it available to other nodes. Analogously to the OCP case, the timing marks provided by the distributed FCS are those used when the data are received in a node. The OS in a particular node uses it own timing mark mechanisms to establish the mark at which broadcast navigation data are needed within the node. A nonblocking network-read OS task is awakened at the appropriate time.

Example 3: Guidance Communication

This example shows how the prelaunch application software uses the timing marks provided by the OS to perform the required communication with the guidance system. The discussion will consider the communication of position data to guidance and the receipt of status data from guidance. These are only two of many guidance communications; however, all are handled similarly.

Position data are continuously provided to guidance throughout the prelaunch sequence. The data generated in the navigation system are read into the FCS, converted into guidance formats, and written to the guidance system. Guidance requires that this be performed in an interval following the 2PPS mark established in navigation communications. In the centralized FCS, the prelaunch software and the OS software, which reads from the navigation system, are in the same computer. In the distributed system, the prelaunch software is in the EGISS node, and navigation data are read by the OS in the NMISS node. In spite of this, the prelaunch software has the same design in both the centralized and distributed FCS. The difference is the level at which the guidance position processing connect point is called. In the centralized system, it is called at the interrupt level; in the distributed FCS, it is called at the task level.

Collecting guidance status also occurs continuously throughout the prelaunch sequence. The prelaunch software uses the OCP connect point in the EGISS to perform all guidance communication except for position data. Guidance status communication occurs at the OCP connect point prior to the end of the 2PPS interval.

SUMMARY

The SLBM FCS prelaunch real-time software provides position data to missile guidance systems, computes missile mission parameters and provides them to the guidance systems, and coordinates the final events in the launch sequence. The prelaunch real-time software executes in a synchronous system that uses a 1PPS signal to allow subsystems to exchange information on coordinated timing marks.

The prelaunch software was originally designed to execute in an FCS with a centralized architecture. The OS in the centralized system provides two synchronous timing marks using interrupt-level connect points. One of these marks is established by the availability of navigation data, the other by the availability of OCP and fire-control information. The prelaunch software uses these timing marks in its guidance communications design. A key element of this design is that guidance communication is performed by DMA access, thus allowing the prelaunch interrupt connect

points to start I/O and check it for completion at a subsequent connect point.

As the prelaunch software is moved to a distributed FCS, similar design concepts are being developed in the context of a commercial OS with network access. The prelaunch software is not distributed across the nodes of the FCS; however, the supporting infrastructure is. The same two timing marks available in the centralized FCS are present in the node where the prelaunch software executes. The navigation data and fire-control information are available in that node when they are received by broadcast transmission on the FDDI network from the NMISS and DCSS, respectively. The timing-mark connect points are provided within the context of the OS tasks that receive the broadcast information.

The shift from interrupt-level timing marks to task-level timing marks is necessary because the commercial OS requires network access through task context. Guidance communication must also be performed at the task level. In order to support task-level timing marks that may be different in the various FCS nodes, a generalized timing mark package has been developed.

REFERENCES

1. Gates, Robert V., "Strategic Systems Fire Control," *Naval Surface Warfare Center, Dahlgren Division Technical Digest*, 1995.
2. Stevens, W. Richard, *UNIX Network Programming*, Prentice Hall, Englewood Cliffs, New Jersey, 1990.

THE AUTHORS

MR. E. AUGUSTUS COOPER, JR.

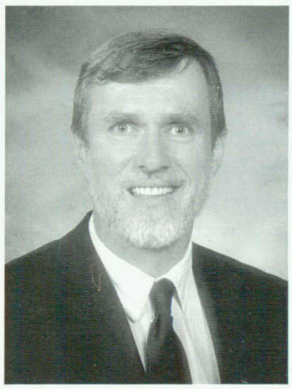

MR. E. AUGUSTUS COOPER, JR., is a computer scientist in the Operational Systems Branch of the Strategic and Strike Systems Department. He has developed compilers, linkers, operating systems, disk file systems, networking software, and various tools. He is currently developing the real-time prelaunch software for the SLBM Fire Control modernization effort. He has a B.S. in mathematics from Randolph-Macon College and an M.S. in computer science from Virginia Tech.

MR. A. LEE PHILPOTT, JR.

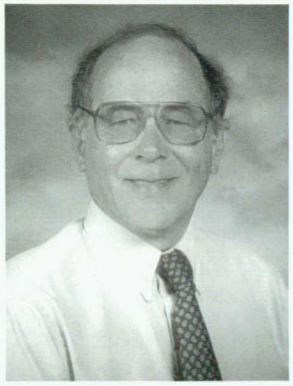

MR. A. LEE PHILPOTT, JR., is a mathematician in the Operational Systems Branch of the Strategic and Strike Systems Department. He has developed operating systems and real-time software for the SLBM Program since the early 1970s, spanning Poseidon, TRIDENT, TRIDENT II, and now the SLBM modernization effort. He has a B.S. in mathematics from the University of Richmond.

Point Mass, Dipole, and Quadrupole Gravity Modeling for FBM Systems Support

Mr. Alan E. Rufty

Theoretical techniques developed at the Naval Surface Warfare Center, Dahlgren Division (NSWCDD) in the early 1980s allow for the construction of accurate and efficient "point source" gravity models. These models comprise various combinations of point masses, point dipoles, and point quadrupoles. The underpinning theory minimizes closed-form expressions related to Dirichlet's integral. In practice, this directly diminishes gravity modeling errors along missile trajectories. In the early '80s, combined point dipole/point mass tesseral gravity nonlinear least-squares fits were developed. In the '80s, these techniques were used in various ways, such as in airborne gravity gradiometer surveying analysis and in developing a Submarine Launched Ballistic Missile (SLBM) gradiometer-based gravity compensation algorithm. Over the past six years, on a per-request basis, regional trajectory gravity models have been developed as a service to other members of the fleet ballistic missile (FBM) community. The underlying theory and the means by which it was applied to these various applications will be discussed.

Introduction

The need for gravitational modeling of a Trident FBM arises from the fact that the accelerometer package used to keep track of the missile position and velocity cannot directly measure gravitational acceleration (G). So the best available way of accurately compensating for G has been direct FBM modeling. G computations can roughly be divided into two parts:[1]

1. Inverse square, oblateness, and low-order tesseral gravitational effects, which are obtained from a degree and order nine spherical harmonic fit.

2. The remaining high-frequency gravity (HFG) part of the G field, which is computed from stored global gravity anomaly data sets.

In theory, the physical description and mathematical modeling of both parts of the field are well understood,[2] but FBM applications must meet stringent efficiency and accuracy requirements. To lessen the computational burden caused by the frequent evaluation of spherical harmonic fields, a replacement model consisting of combined dipole and point masses is used. (This will be the focus of the next three sections.) Combined point mass/point dipoles (PM/DPs) are currently not used directly in the HFG part of FBM computations, but two studies suggest they could play a unique role if certain capabilities are desired in the future. These studies and other potential applications will be briefly addressed in the final section of this article. One other application arises because the global HFG anomaly data contains a mix of commercial proprietary data that nongovernment members of the FBM team involved in flight testing cannot use to simulate HFG effects. To circumvent this and other problems, appropriate launch areas have been modeled with localized regional PM/DP HFG models. This effort is discussed in the section on Regional PM/DP HFG Evaluators.

HISTORICAL OVERVIEW OF PM/DP TESSERAL FITS

A precise, well-founded theoretical approach is undoubtedly necessary to obtain the near-optimal results desired of an FBM point mass (PM) tesseral evaluator. However, while various governmental researchers, including several at NSWCDD, obtained PM tesseral gravity fits prior to 1980, and various PM fits have been published before and since in journals, all of these other efforts seem to be somewhat off the mark. An effort directed by Davis Owen led to a satisfactory theoretical underpinning in the early 1980s. First Dr. John Shebalin,[3] following the lead of other researchers, suggested that a general inner product setting be adopted and that Dirichlet's integral be minimized. Dr. Shebalin did not, however, seriously attempt any actual point-mass fits. After Dr. Shebalin left NSWCDD, the author began working for Davis Owen in this area. First, the physics of the problem was carefully examined, and it was determined that Dr. Shebalin was essentially correct, in that either Dirichlet's integral or something very close to it should be minimized.[4] Next, the mathematical underpinnings were examined, and it was determined that another mathematical basis was needed.[4]

When the PM positions are predetermined, a linear least-squares (LLSQ) problem results. In general, the problem of finding point source strengths with given source positions is linear and is thus called the LLSQ problem. Dirichlet's integral was quite adequate for solving the LLSQ problem in the case of tesseral fits; however, to obtain good quality fits, it is necessary to also regard the PM locations as parameters to be fit, and this is a nonlinear least-squares (NLLSQ) problem. In fact, the NLLSQ problem is a very badly behaved large-scale problem with local numerical instabilities. This almost necessitates the use of a customized algorithm that utilizes various closed-form partial derivatives of the cost function, which would be far too cumbersome for a Dirichlet integral implementation.

A new minimization criterion was developed that retained the most desirable fitting aspects of the Dirichlet integral, while simultaneously providing closed-form exact equations for the LLSQ problem and closed-form partials required in the NLLSQ problem.[4] With a considerable application of time and effort, this theoretical basis allowed for the development of good PM fits. After the PM fits were obtained, it was found that even more efficient evaluators could be obtained by using point dipoles (DP) as well as PMs.[5] That is, if a DP is placed at the same location as a PM, then little extra execution time is incurred at the time of evaluation, and yet there are three extra degrees of freedom per point source location (whereas a PM has a scalar point source strength, a DP has directionality as well as an overall source magnitude). Again, after considerable time and effort were expended, good fits were obtained.

THEORY AND APPLICATION OF POINT MASS FITS

First, consider the coordinate frame to be used. Since all rotational effects can be easily accounted for after the fact, the earth's gravity will be modeled at an instant where an inertial and earth-fixed frame coincide and have their origin at the earth's center, their z-axis is along the north pole, their x-axis is through the Greenwich meridian, and their y-axis is chosen to complete a right-handed coordinate system. With this convention, we need not distinguish between gravity and gravitation.[2] Next, it is useful to introduce the tesseral model that is to be fit. For this model, consider the following definition for the gravitational potential, W:

$$W(\boldsymbol{x}) \equiv \frac{1}{R_E}\sum_{n=0}^{N_T}\left(\frac{R_E}{r}\right)^{n+1}\sum_{n=0}^{N_T}[a_{nm}R_{nm}(\theta,\lambda) + b_{nm}S_{nm}(\theta,\lambda)] \quad (1)$$

In Equation (1), $\boldsymbol{x} = (x, y, z)^T$, where T denotes a transpose, $r = |\boldsymbol{x}|$, $\theta = \tan^{-1}([x^2 + y^2]^{1/2} / z)$, and $\lambda = \tan^{-1}(y / x)$. Also, $R_{nm} = P_{nm}(\cos\theta)\cos m\lambda$ and $S_{nm} = P_{nm}(\cos\theta)\sin m\lambda$, where P_{nm} is the associated Legendre function of degree n and order m. The upper summation limit N_T specifies the degree and order of the tesseral field. Also, a_{nm} and b_{nm} are expansion coefficients, and R_E is the radius of the earth (a_{nm}, b_{nm} and R_E are data-related constants). The tesseral gravity field $\boldsymbol{G}_{Tess}$ to the specified degree and order can then be found by taking the gradient of the potential:

$$\boldsymbol{G}_{Tess} = GM_E\nabla W \equiv GM_E\left(\frac{\partial W}{\partial x}, \frac{\partial W}{\partial y}, \frac{\partial W}{\partial z}\right)^T \quad (2)$$

Here, for convenience, the data factor GM_E was transferred from Equation (1) to Equation (2) and, in keeping with the sign conventions of physical geodesy, a positive gradient was taken.[2] Next, consider a PM model corresponding to Equations (1) and (2) with a general potential form specified by

$$V(\boldsymbol{x}) = \sum_{k=1}^{N_P}\frac{m_k}{|\boldsymbol{x} - \boldsymbol{x}_k|} = \sum_{k=1}^{N_P}\frac{m_k}{\sqrt{(x - x_k)^2 + (y - y_k)^2 + (z - z_k)^2}} \quad (3)$$

and a corresponding gravity acceleration of

$$\boldsymbol{G}_{PM} = GM_E\nabla V \quad (4)$$

The problem at hand, then, is to determine a fixed number (N_p) of PM strengths (m_k) and locations ($\boldsymbol{x}_k$) so that $\boldsymbol{G}_{PM}$ accurately matches $\boldsymbol{G}_{Tess}$.

The error in the gravity fit is $\delta\boldsymbol{G}(\boldsymbol{x}) = \boldsymbol{G}_{Tess}(\boldsymbol{x}) - \boldsymbol{G}_{PM}(\boldsymbol{x})$, and it has components $\delta\boldsymbol{G}(\boldsymbol{x}) = (\delta G_x, \delta G_y, \delta G_z)^T$. It is assumed that the $\boldsymbol{x}$'s are outside, or on the boundary of, a given sphere of radius R, which is here taken to be R_E. This region of space is denoted Ω so that $\boldsymbol{x} \in \Omega$ implies $|\boldsymbol{x}| \geq R_E$. All the point sources are thus outside Ω or inside the same sphere: $|\boldsymbol{x}_k| < R_E$. Perhaps the first idea that comes to mind is simply to apply a least-squares criteria to each of the components of the gravity errors at a number of specified *sample points* $\{\boldsymbol{x}'_j \in \Omega, \quad j = 1,2,3,\cdots,J\}$:

Minimize Φ, where

$$\Phi = \sum_{j=1}^{J}[\delta G_x(\boldsymbol{x}'_j)]^2 + \sum_{j=1}^{J}[\delta G_y(\boldsymbol{x}'_j)]^2 + \sum_{j=1}^{J}[\delta G_z(\boldsymbol{x}'_j)]^2 = \sum_{j=1}^{J}|\delta G(\boldsymbol{x}'_j)|^2 \quad (5)$$

This minimization condition has one big advantage: since the fits will most often be used to predict the effects of G on some physical system, the errors at the time of use will be minimized since the least-squares process

controls these gravity errors directly (provided the points $\boldsymbol{x}'_j$ are well chosen). There are still theoretical and practical difficulties with the approach depicted in Equation (5), however, and sampling at a fixed finite set of points (i.e., discretization) can be expected to greatly exacerbate them.[4] It is thus desirable to take the sample points in Equation (5) to be very dense everywhere inside Ω, which entails a continuous sampling limit. This limit yields the following optimization process, which will serve as a basis for our subsequent discussion:

$$\text{Minimize } \Phi, \text{ where}$$
$$\Phi \equiv \iiint_{\Omega} |\delta \boldsymbol{G}(\boldsymbol{x})|^2 d^3 x \tag{6}$$

In Equation (6) it is more mathematically convenient to deal with potentials rather than vector field quantities directly, so the potentials, W and V of Equations (1) and (3), will be used with Equations (2) and (4) understood. It is especially convenient to introduce the general norm and inner product structure of functional analysis,[6] which will be briefly explained below. Towards that end, consider the following definitions that hold for any harmonic functions f and g in Ω that drop off at least as fast as $1/r$ for $r \equiv |\boldsymbol{x}| \geq R \equiv R_E$:

$$\|f\|_E^2 \equiv \tfrac{1}{8\pi} \iiint_{\Omega} \nabla f \bullet \nabla f \; d^3 \boldsymbol{x} \tag{7}$$

and

$$(f, g)_E^2 \equiv \tfrac{1}{8\pi} \iiint_{\Omega} \nabla f \bullet \nabla g \; d^3 \boldsymbol{x} \tag{8}$$

First, observe that the norm defined by Equation (7) follows immediately from the inner product defined by Equation (8). Each of these definitions can be viewed as a shorthand expression for their respective integrals on the right-hand side (RHS) with f and g as arguments. The norm and inner product defined here are a direct generalization of the usual magnitude of a vector and vector dot product from elementary vector analysis except that *vectors* in the new space, f and g for example, are admissible functions. Also, the inner product is no longer unique, so a subscript is commonly used. For example, the RHS of Equation (7) is proportional to the energy contained in the field, so the resulting norm is called the energy norm and is denoted $\|\cdot\|_E$. The integral on the RHS of Equation (7) without the factor of $1/(8\pi)$ is the well known Dirichlet integral.

Given the definition of $\|\cdot\|_E$, optimization Equation (6) can be compactly rewritten as

$$\text{Minimize } \Phi_E \text{ where}$$
$$\Phi_E = \Phi_E(m_k, x_k)$$
$$\equiv \tfrac{1}{2}\|W - V\|_E^{\,2} \tag{9}$$

since the minimization of $c\,\Phi$ is equivalent to the minimization of Φ for any constant c. A factor of 1/2 appears here to conform to the usual conventions of NLLSQ optimization. Equation (9) must still be subjected to further analysis in order to determine if it is suitable for NLLSQ applications.

The real advantage of the norm and inner product notation is that generalized least-squares or optimization processes can be efficiently stated and handled. Given that the final form of the optimization condition chosen may entail some other norm, it is natural to briefly analyze minimization conditions within the general context of a "generic" inner product $(\cdot\,,\cdot)$ and associated norm $\|\cdot\|$. Here, and in the sequel, we restrict ourselves to well-behaved real valued functions that are harmonic in Ω and fall off at least as fast as $1/r$. These functions are, of course, subjected to the usual rules of scalar multiplication and addition (i.e., $a\,f(\boldsymbol{x}) + bg(\boldsymbol{x})$ is always a well-behaved function) that allow us to view this class of functions as a vector space. Thus, given that a and b are ordinary real numbers and h is a function, the inner product and norm must satisfy the following main conditions:

$(f,g)=(g,f)$, $(af+bg,h)=a(f,h)+b(g,h)$, $\|f\|^2 \equiv (f,f)$, and $\|f\|>0$ for $f \neq 0$.

Notice that if $\Phi = \frac{1}{2}\|W-V\|^2 = \frac{1}{2}\|W\|^2 + (W,V) + \frac{1}{2}\|V\|^2$ and if $\ell_k(\boldsymbol{x}) \equiv |\boldsymbol{x} - \boldsymbol{x}_k|$, then the (general) cost function can be written

$$\Phi(m_k, x_k) = \frac{1}{2}\|W\|^2 + \sum_{k=1}^{N_P} m_k A_k + \frac{1}{2}\sum_{k=1}^{N_P}\sum_{k'=1}^{N_P} m_k m_{k'} T_{k,k'} \quad (10)$$

where $A_k \equiv (W, \ell_k^{-1})$ and $T_{k,k'} \equiv (\ell_k^{-1}, \ell_k^{-1})$. To minimize this expression with regards to the various point source strengths (m_k), first take the various partials of Φ with respect to those source parameters and set the result to zero to obtain

$$\sum_{k'=1}^{N_P} T_{k,k'} m_{k'} = A_k \quad (11)$$

where $k = 1, 2, 3, \cdots, N_p$. Provided that A_k and $T_{k,k'}$ can be accurately evaluated, the source strengths can then be determined in a fairly straightforward fashion by numerically solving this linear equation. For spherical harmonic reference potentials W with a low to moderate degree and order [$N_T \leq 15$, say, in Equation (1)] computable expressions for A_k and $T_{k,k'}$ can be found for various norms.[4,5] It is thus possible to try out various norms in the LLSQ case and see how the results compare, but if efficient good quality fits are necessary, then the source locations must be determined also. First-order partials, and possibly second-order partials, with respect to $\boldsymbol{x}_k$ of Φ, and thus of A_k and $T_{k,k'}$, will then be required. For this NLLSQ problem, it is clearly desirable, if not necessary, to find a norm that provides simple closed-form mathematical expressions for A_k and $T_{k,k'}$. (To use optimization procedures that rely on the numerical evaluation of partials is clearly asking too much for this particular problem.)

A new norm exists that satisfies these mathematical requirements, and it is called the "integral norm"[4] since the required integrals can be evaluated in simple closed form, and there is no simple physical minimization criterion to serve as a label as there was for the energy norm. The integral norm and its associated inner product are defined as follows[4]:

$$\|f\|_I^2 \equiv \frac{R^2}{4\pi}\iint_\sigma \left[-\frac{\partial}{\partial r}(r f^2)\right]\Big|_{r=R} d\sigma \quad (12)$$

$$(f,g)_I^2 \equiv \frac{R^2}{4\pi}\iint_\sigma \left[-\frac{\partial}{\partial r}(frg)\right]\Big|_{r=R} d\sigma \quad (13)$$

where, as in Heiskanen and Moritz,[2] σ and $d\sigma = \sin\theta\, d\theta\, d\lambda$ have the following meaning when associated with an integral of $f(\boldsymbol{x})$:

$$\iint_\sigma f(r,\theta,\lambda)\, d\sigma \equiv \int_{\theta=0}^{\theta=\pi}\int_{\lambda=0}^{\lambda=\pi} f(R,\theta,\lambda)\sin\theta d\theta d\lambda$$

The integral norm is closely related to the energy norm both physically and mathematically. For example, by applying Green's first identity to the RHS of Equation (8), one can show that[4] $(f,g)_I = 4R(f,g)_E - R^2\iint_\sigma fg\, d\sigma$. Finally, by other means one can show, as required, that[4] $\|f\|_I > 0$ for an admissible f, such that $f \neq 0$.

It can be shown by various ways that[4,5] for $\boldsymbol{x}_k \neq 0$,

$$\left(W, \frac{1}{\ell_k}\right)_I = \frac{R^2}{r_k} W\left(\frac{R^2}{r_k}\boldsymbol{x}_k\right) \quad (14)$$

while for $\boldsymbol{x}_k = 0$, $(W, \ell_k^{-1})_I = a_{00}$. In Equation (14), $r_k = |\boldsymbol{x}_k|$. Thus, the integral norm yields simple closed-form expressions for A_k and $T_{k,k'}$. These expressions can then be used in Equation (11) to find m_k. Equation (14) also clearly allows for a full NLLSQ implementation. It is possible to mathematically predict the relative spherical harmonic degree weights that the energy norm, the integral norm, and other

norms are likely to produce in fits without actually doing any fits.[4] After this and much other preliminary analysis was carried out, including LLSQ fitting tests with the energy norm, the integral norm, and one other norm, all of the analysis and tests indicated that the integral norm is the most suitable one to use for both LLSQ and NLLSQ fitting to any gravity field. Hence, the decision of which norm to use was easy since the integral norm is probably the only one sufficiently tractable enough to produce actual NLLSQ fits of acceptable quality.

The techniques used to produce NLLSQ fits will be discussed next. First, observe that Equation (11) always determines a solution for the m_k's once the x_k's are specified, so if Equation (11) is always assumed to hold, one can set up a new optimization process:

$$\text{Minimize } \Phi_I(\boldsymbol{x}_k) = \Phi_I(m_k(\boldsymbol{x}_k), \boldsymbol{x}_k) \text{ where}$$

$$\Phi_I(\boldsymbol{x}_k) = \tfrac{1}{2}\|W\|_I^{\,2} + (W,V)_I + \tfrac{1}{2}\|W-V\|_I^{\,2} \qquad (15)$$

$$\text{with } \sum_{k'=1}^{N_P} T_{k,k'} m_{k'} = A_k$$

In Equation (15), $k = 1, 2, 3, \cdots, N_p$. Let $\vec{\alpha}$ denote the $3N_P$ dimensional vector whose components consist of all the components of all the $\boldsymbol{x}_k$'s arranged in some order. It is then possible to rewrite $\Phi_I(\boldsymbol{x}_k)$ as $\Phi_I(\vec{\alpha}) = \Phi_I(\alpha_j)$, where $j = 1, 2, 3, \cdots, 3N_P$. It is possible to find "closed-form" expressions for the gradient, whose components are $\partial\Phi_I(\vec{\alpha})/\partial\alpha_j$, as well as the Hessian, whose components are $\partial^2\Phi_I(\vec{\alpha})/\partial\alpha_j\partial\alpha_{j'}$, where j and j' also range from 1 to $3N_P$. After the Hessian and gradient were implemented and checked out, various standard NLLSQ algorithms were tried,[7,8] but could not be made to work even after extensive and repeated efforts. A well-respected commercial library conjugate gradient descent algorithm also failed. The structure of the Hessian and cost function were then analyzed thoroughly, and it was determined that many "saddle points" and false local minima existed due to the initial conditions or the nature of the optimization problem itself (there also appeared to be false small-scale minima associated with numerical ill-conditioning). It then became obvious that a customized NLLSQ algorithm was required.

At this point, as an experiment, a simple "steepest-descent" algorithm was implemented, which showed some signs of working. Taking a clue from this, a conjugate gradient algorithm with restarts was implemented which, in the end, proved to be suitable after a sufficient number of modifications were made in the way the algorithm was used. The two most important factors in its success are thought to be the use of momentum in the line-search algorithm and the use of an analog of simulated annealing in the basic optimization procedure itself.

Two good NLLSQ PM fits were obtained.[4] The first consisted of 50 PMs used to model the WGS-72 tesseral field[4] truncated at degree and order 9 (WGS-72 9×9). The root-mean-square (RMS) difference between surface anomalies of this PM model and the WGS-72 9×9 field was found to be 0.79 mgal by direct surface evaluation. Here a milligal is a commonly used measure of gravity anomaly error with the value of $1. \times 10^{-5}$ meters per second squared. From error degree variances,[4] this RMS anomaly modeling difference was computed to be 0.68 mgal. The second fit consisted of 80 PMs developed to model the WGS-72 tesseral field truncated at degree and order 12 (WGS-72 12×12). For this second fit, the computed RMS surface anomaly error was 0.65 mgal, while computation from the RMS of anomaly degree variances gave 0.53 mgal.

COMBINED DIPOLE AND POINT MASS FITS

The preceding PM fitting technique can be easily generalized to handle combined PM/DP fits. First, Equation (3) for the PM potential is replaced by the expression for the potential of a combined PM/DP set:

$$V(\boldsymbol{x}) = \sum_{k=1}^{N_p} \left\{ \frac{m_k}{|\boldsymbol{x} - \boldsymbol{x}_k|} + \frac{\boldsymbol{D}_k \cdot (\boldsymbol{x} - \boldsymbol{x}_k)}{|\boldsymbol{x} - \boldsymbol{x}_k|^3} \right\} \tag{16}$$

Here, $\boldsymbol{D}_k$ is the vector strength of the k'th DP. Let $\boldsymbol{x} = (x, y, z)^T = (x^1, x^2, x^3)^T$, $\boldsymbol{x}_k = (x_k, y_k, z_k)^T = (x_k^1, x_k^2, x_k^3)^T$, and $\boldsymbol{D}_k = (D_k^1, D_k^2, D_k^3)^T$. When Equation (16) is used in Equation (10), and Equation (11) is generalized to determine the values of m_k and $\boldsymbol{D}_k$, inner products of the previously evaluated form $(W, \ell_k^{-1})_I$ and of the form $(W, \ell_k^{-3}\{x^i - x_k^i\})_I$, $i = 1, 2, 3$, are required to determine the components of the new A_j for $j = 1, 2, 3, \cdots, 4N_p$. Observe that

$$-\frac{(x^i - x_k^i)}{|\boldsymbol{x} - \boldsymbol{x}_k|^3} = \frac{\partial}{\partial x^i}\frac{1}{\ell_k} = -\frac{\partial}{\partial x_k^i}\frac{1}{\ell_k} \tag{17}$$

so

$$\left(W, \frac{(x^i - x_k^i)}{|\boldsymbol{x} - \boldsymbol{x}_k|^3}\right)_I = \left(W, \frac{\partial}{\partial x_k^i}\frac{1}{\ell_k}\right)_I$$
$$= \frac{\partial}{\partial x_k^i}\left(W, \frac{1}{\ell_k}\right)_I = \frac{\partial}{\partial x_k^i}\left[\frac{R^2}{r_k} W\left(\frac{R^2}{r_k^2}\boldsymbol{x}_k\right)\right] \tag{18}$$

The same approach employed in obtaining Equation (18) can be used to find the elements of the associated $T_{j,j'}$, which is the natural generalization of the $T_{k,k'}$ found in Equation (11) and where $j = 1, 2, 3, \cdots, 4N_p$ and $j' = 1, 2, 3, \cdots, 4N_p$, although some care must be exercised in evaluating terms of the form $(\ell_k^{-1}, \ell_k^{-3}\{x^i - x_k^i\})_I$ or $(\ell_k^{-3}\{x^i - x_k^i\}, \ell_k^{-3}\{x^i - x_k^i\})_I$. If M denotes the vector of length $4N_p$ made up of the components of m_k and D_k, and if A and T denote the vector and matrix with components A_j and $T_{j,j'}$, respectively (as discussed above), then Equation (11) is replaced by

$$\boldsymbol{T}\,\boldsymbol{M} = \boldsymbol{A}, \tag{19}$$

which solves the LLSQ combined PM/DP problem. The NLLSQ optimization then can be stated in a form similar to Equation (15):

$$\text{Minimize } \Phi_I(\boldsymbol{x}_k) = \Phi_I(M(\boldsymbol{x}_k), \boldsymbol{x}_k) \text{ where}$$
$$\Phi_I(\boldsymbol{x}_k) = \tfrac{1}{2}\|W\|_I^2 + (W, V)_I + \tfrac{1}{2}\|W - V\|_I^2 \tag{20}$$
$$\text{with } \boldsymbol{T}\,\boldsymbol{M} = \boldsymbol{A}$$

Here, $k = 1, 2, 3, \cdots, N_p$. The solutions to Equation (20) can then be found the same way as before for Equation (15), but the implementation details are more complicated.

Again, two good NLLSQ fits were obtained: a 22 combined PM/DP gravity model of the WGS-72 9×9 field and a 35 combined PM/DP model of the WGS-72 12×12 field. The RMS differences between surface anomalies of the combined PM/DP models and the original tesseral fields were found by direct surface evaluations to be 0.43 mgal for the WGS-72 9×9 fit and 0.45 mgal for the WGS-72 12×12 fit. From error degree variances, the RMS difference between surface anomalies of the combined PM/DP model and the original tesseral surface anomalies was found to be 0.33 mgal for the WGS-72 9×9 fit and 0.37 mgal for the WGS-72 12×12 fit. Subsequent DP fits have been performed, and the errors of the fits have been reduced after every fit. For example, fits to the unclassified part of the WGS-84 tesseral field currently have RMS errors of less than 1/4 mgal, and the overall error is less than 1 mgal at every point.

REGIONAL PM/DP HFG EVALUATORS

The same techniques used to do combined PM/DP modeling can be used to model HFG effects for various launch regions and target regions of interest. These gravity models are required by other facilities involved in FBM systems support that need compact, accurate,

and efficient nonproprietary HFG evaluation schemes for both post- and preflight analysis of test flights. So far, each gravity model is tied to a particular launch region and to one or two nearby target regions of interest (when more than one general launch region is required, or the target regions are separated, then independent fits must be done for each case). The launch regions are specific test-flight or calibration areas. Generally, each HFG evaluator consists of 32 or fewer combined PM/DPs that serve to model HFG effects for all phases of missile flight. These HFG evaluators take orders of magnitude less time than a standard HFG evaluator.

Equation (19) is the basic equation used to develop these fits. The same number of HFG values were used as there were combined PM/DPs in the fit. The positions P_k of the HFG evaluations were fixed first, and then the point source locations were specified using $\boldsymbol{x}_k = R^2 |\boldsymbol{P}_k|^{-2} \boldsymbol{P}_k$, which follows directly from the condition $\boldsymbol{P}_k = \frac{R^2}{r_k^2} \boldsymbol{x}_k$, as required by Equation (14). Typically 25 HFG values were required, with 9 of them spread out over the surface of the launch region. The rest of the values were typically split between grid points at altitude, which were used to model gravity right above the local launch region, and points spread out all along various sample trajectory paths.

There were three complications associated with these fits. First, Equation (19) also requires that the potential be available, and the HFG potential (which is again denoted W) was not generally available. To overcome this problem the equation $W(\boldsymbol{P}_k) = W_0 + \int_{x_0}^{P_k} \boldsymbol{G}_{HFG} \bullet dx$ was used, where $\boldsymbol{x}_0$ is the center of the surface launch region, and $W_0 \equiv W(\boldsymbol{x}_0)$. Thus, given a value of W_0, all of the required potential values can be obtained by numerically integrating HFG values along some path from $\boldsymbol{x}_0$ to $\boldsymbol{P}_k$. This leaves W_0 as a parameter to be determined. The second complication arises from the fact that the equation $\boldsymbol{P}_k = \frac{R^2}{r_k^2} \boldsymbol{x}_k$ must be maintained even though some of the points P_k are on the earth's surface, and it is generally desirable to have the PM/DPs far below the earth's surface. Thus R also becomes a variable parameter that must be determined each time prior to invoking Equation (19). This leaves the third complication. Since these fits contain a very small number of PM/DPs spread out over a large geographic region, the requirements of a simultaneous high-quality match at low altitudes and at high altitudes may not be compatible with the basic attenuation properties of the HFG field itself. (In fact, along a single missile trajectory, it is not at all unusual for some of the components of an HFG history to actually increase markedly with altitude before finally tailing off.) For launch regions where the attenuation properties had these undesirable qualities, a layered fitting technique was employed to improve the quality of the fit. The total number of PM/DPs needed for all the layers together never exceeded 32.

It is not possible to directly determine the values of R and W_0 from a process like Equations (19) or (20), so a second "outer-loop" optimization process is required to find them. First, notice that when particular values of R and W_0 are assumed, and the 25 or so positions of the P_k's are selected, one can carry through with an LLSQ fitting process using Equation (19) and obtain an associated trial HFG evaluator. The error of this fit, $\delta \boldsymbol{G}$, can then be taken as the difference between the HFG reference field and this trial HFG evaluator. With this $\delta \boldsymbol{G}$, an outer-loop cost function can be set up based on Equation (5). The points $\boldsymbol{x}_j'$ in Equation (5) were taken to be along various possible trajectories flown from the launch area of interest to the target area(s) of interest. Point weighting factors were also inserted into Equation (5) to give a more representative cost function, $\Phi = \Phi(R, W)$. A non-gradient-based NLLSQ optimization was used to determine the optimal R and W_0. When the layered fitting technique was used, the optimum values of R and W_0 were obtained for each layer. The PM/DP values of the fit were then the ones associated with the optimal values of R and W_0. The overall quality of the fits was very dependent on the relative positions of the DPs, so the selection of the correct P_k locations,

which had to be done essentially "by hand," was critical. The fits were thus frequently time-consuming to develop.

EXTENSIONS OF THE THEORY AND OTHER APPLICATIONS

Generalizations to fits involving parameterized line sources, surface distributions, and volume distributions, as well as connections to survey applications, were developed.[5] The rather extensive links of PM/DP theory to geophysical collocation were also mapped out.[5] It was determined that PM/DP techniques also have a diversity of other potential applications. One application associated with the acquisition of gravity data itself will be mentioned first. Although G cannot be measured intrinsically (i.e., without, say, external position information), if extraordinary accuracy is maintained, a fixed arrangement of accelerometers can detect variations in G over the extent of the arrangement itself. Such variations of gravity are called gravity gradients, and the associated accelerometer arrangements are at the heart of an instrument called a gravity gradiometer. Gravity gradiometers were tested several years ago by the Defense Mapping Agency as a survey tool to be used aboard low-flying aircraft traversing a gridded pattern. DPs, PMs, and point quadrupoles were successfully tested in this connection; however, the overall data processing techniques were fairly complex and would require more space than is available here to properly discuss.

Finally, two other applications were successfully tested that are not now used in FBM. When applied, the first one would allow for a significant speedup of the FBM HFG implementation by doing an "on-the-fly" PM/DP fit, which would significantly lower the number of HFG evaluations required in certain situations. Unfortunately, this application would require a modification to the existing FBM HFG evaluator in order to obtain HFG potential values, which are not currently available. The second tested FBM application addressed the issue of whether a gravity and gravity gradient history obtained from a shipborne gravity gradiometer could be used to accurately compensate for in-flight HFG effects in regions where gravity anomaly information was inadequate or nonexistent. This algorithm utilized a point gravity and gravity gradient value at the launch point, as well as available gravity information at altitude. Testing indicated that, when properly implemented, this algorithm would work quite well with an accurate gradiometer.

REFERENCES

1. Gates, Robert V., "Strategic Systems Fire Control," *Naval Surface Warfare, Dahlgren Division Technical Digest 1995 Issue.*

2. Heiskanen, Weikko A. and Moritz, Helmut, *Physical Geodesy*, W.H. Freeman and Co., San Francisco, CA, 1967.

3. Shebalin, John V., *On the Theory and Optimization of Global Point-Mass Expansions of Anomalous Gravity*, NSWC TR 79-170, Jun 1979.

4. Rufty, Alan E., *A Mathematical Basis for the Determination of Optimal Point Mass Gravity Fits*, NSWC TR 82-487, Mar 1983.

5. Rufty, Alan E., *Techniques for Utilizing Point, Point Dipole, Point Quadrupole, and Continuous Mass Distributions for Gravity Reduction, Estimation, and Modeling*, NSWC TR 83-341, Dec 1983.

6. Kreyszig, Erwin, *Introductory Functional Analysis with Applications*, John Wiley and Sons, New York, NY, 1978.

7. Dennis, J.E. and Schnabel, R.B., *Numerical Methods for Unconstrained Optimization and Nonlinear Equations*, Prentice Hall, NJ, 1983.

8. Gill P.E., Murray, W., and Wright, M.H., *Practical Optimization*, Academic Press, New York, NY, 1981.

THE AUTHOR

MR. ALAN E. RUFTY

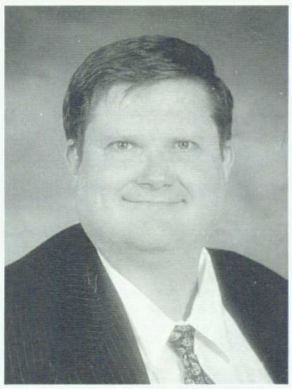

MR. ALAN E. RUFTY is a physicist in the Fire Control Formulation Branch of the Strategic and Space Systems Department. After receiving his B.S. in applied mathematics from North Carolina State University (NCSU) with a minor in economics he took a year to switch from math to physics and then spent three years in graduate school at NCSU specializing in general relativity. Since then, he has worked at NSWCDD. He has over 20 years experience in various facets of trajectory modeling and gravity applications. He has also worked in other diverse disciplines, such as neural networks, coding theory, control theory, numerical analysis, digital signal processing, optimization theory, and approximation and interpolation theory. He has received several Strategic and Space Systems Department technical excellence awards. He is a member of the American Physical Society, the American Mathematical Society, and the American Association of Physics Teachers.

Computation of Ballistic Parameters for SLBM

Ms. Kimberly A. Wright

The trajectory of a ballistic missile is affected by several factors during the course of reentry. These effects cannot be corrected during reentry and, hence, must be accounted for in the targeting data computed prelaunch. Atmospheric density and wind values are among these factors. In order to compensate for these effects, environmental data must be sent to the fleet ballistic missile submarines (SSBNs). Due to the amount of data needed for support and data transmission bandwidth limitations, the wind and density data are condensed into ballistic parameters (BALPARs). This article describes the process by which these values are determined and made available for TRIDENT I and TRIDENT II system usage. This methodology has been used for several years and is currently being examined for various improvements. Some of the avenues being researched in order to improve atmospheric compensation techniques are also presented within this article.

Introduction

Once released from the Submarine Launched Ballistic Missile (SLBM), the reentry body (RB) is ballistic and subject to the forces related to freefalling. To achieve the designated target, the effects of these forces encountered during reentry must be included within the RB release parameters. The onboard fire-control system contains a reentry model to approximate the effects of these forces and computes an offset to the target position used by the missile guidance system in its steering computations. Embedded within this model is the 1962 version of the U.S. Standard Atmosphere consisting of mean air density data. No wind data are contained within the model. Wind effects and the deviation of air density from the Standard Atmosphere values can be significant enough to cause a large effect on the RB performance. Because of this, air density deviation and wind effects must be included in the offset computations if system accuracy goals are to be achieved. Figure 1 shows an example of the effects that the weather data can have on the range of the RB. The effects shown are in addition to those encountered by using the U.S. Standard Atmosphere data.

In order to reduce target miss distance as much as possible, timely wind and density data should be used. The Fleet Numerical Meteorology and Oceanography

Center (FNMOC) operates an atmospheric prediction model that produces a global grid of wind and density forecast data. For each grid-point location, wind and density data, among other environmental parameters, are derived at various altitudes. The compilation of the vertical data for each location is called a profile, as seen in Figure 2.

A subset of the FNMOC grid points, called the operational grid, is defined by the Naval Surface Warfare Center, Dahlgren Division (NSWCDD) and consists of the grid point locations required to support the target data base. Depending on the number and locations of possible targets, the number of operational grid points can be quite large.

NSWCDD provides the operational grid points to FNMOC, and the forecast weather data is extracted for these points. FNMOC is responsible for transmitting these data to the SSBN fleet. This is accomplished by writing the data to a naval message and sending it to the fleet via the Task Force Commanders (CTFs). The CTFs relay the weather data to the SSBNs by submarine radio broadcast.

Broadcast time constraints restrict the length of the information sent to the SSBNs. Providing forecast profiles for the entire operational grid would consume an unacceptable amount of broadcast time. To compensate for this, the profile data for each grid point is reduced to BALPARs. These are constant values that, when applied throughout the trajectory, produce approximately the same effect on the RB as the vertical profile data. The method for deriving these BALPARs is described in the following sections. By utilizing BALPAR data, the message to the fleet (known as a BALPAR message) is of a more acceptable size and can be easily transmitted to the SSBNs.

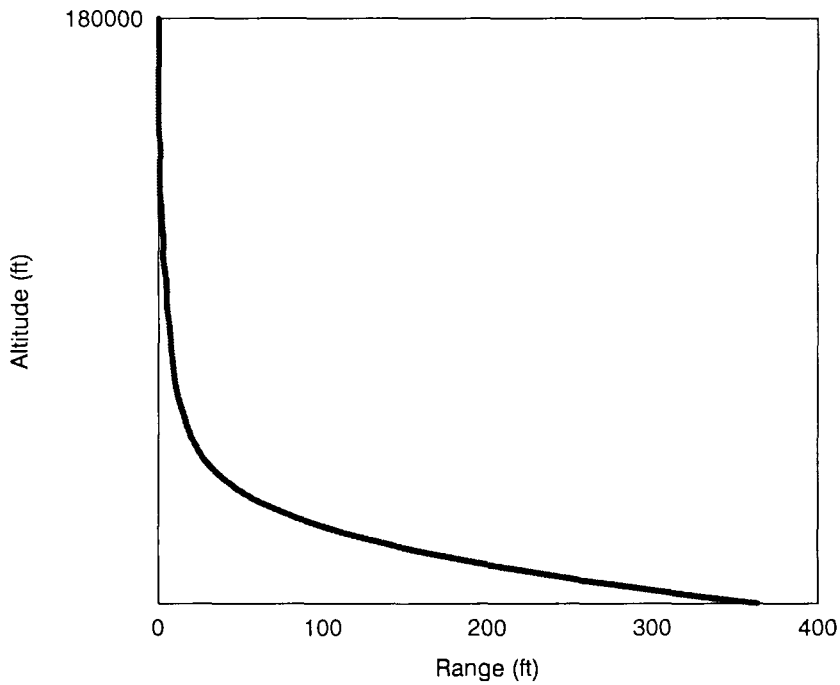

Figure 1—Weather Effects on Range

Once the message is received onboard the SSBN, the BALPAR data are validated, entered, and accessed for preflight computations. When data for a specific target are needed, an

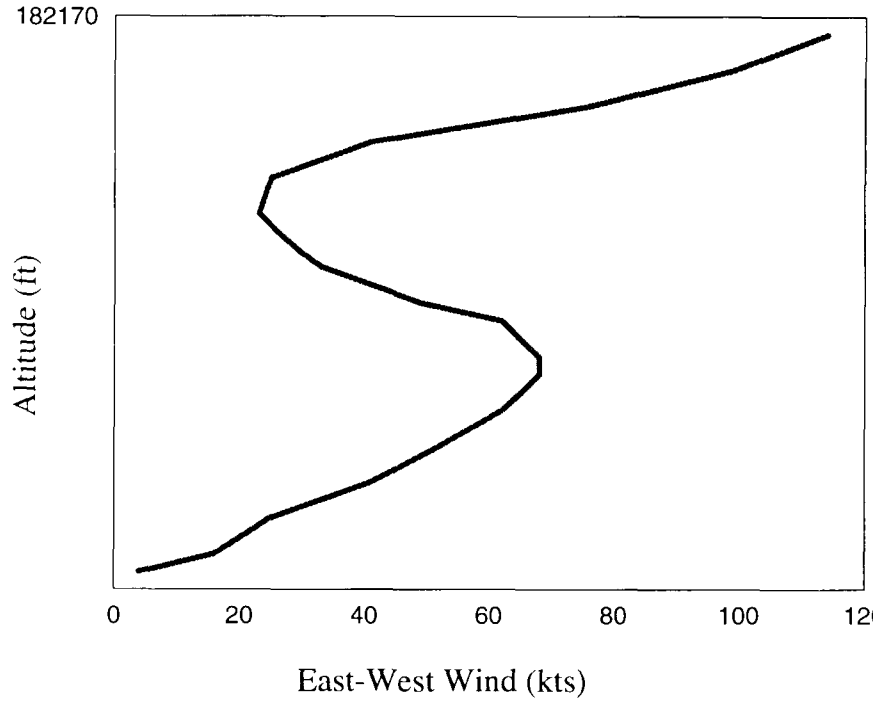

Figure 2—Profile Data

interpolation is performed between surrounding grid points in order to approximate the weather conditions at the site of the target. These data, along with the Standard Atmosphere data, are used within the fire-control reentry model to generate the target offsets.

Forecast BALPARs are generated and broadcast to the SSBN fleet every 12 hours. If forecast data are unavailable or have expired, climatology data is utilized. Climatology BALPARs are stored electronically onboard the SSBNs and consist of monthly mean weather data at each of the global grid locations. If needed, these data are automatically extracted and used in place of the forecast BALPARs in the offset calculations.

COMPUTATION OF WEIGHTING FACTORS

The first step in producing BALPAR data is to generate weighting factors.[1] These data will be used to "weight" the profile data at different heights in order to produce the constant BALPAR value. The weighting factors are dependent upon performance effects at various altitudes. These effects are further influenced by the trajectory of the RB. The envelope of possible trajectories is bounded and represented by reentry velocities (V) and flight-path angles(γ). At the time of BALPAR data generation, the RB trajectories are unknown. Therefore, the weighting factors must be designed so that the BALPARs are sufficiently accurate regardless of trajectory flown.

To produce the weighting factors for the wind effect, a six degree-of-freedom reentry simulation model is executed using a constant-valued wind profile for a variety of V-γ trajectories. The range effect of the wind at specified altitudes for each trajectory is then computed. Each altitude (i) is assigned a percentage (ΔR_i) of total wind effect by taking the range effect of wind at that altitude and dividing it by the total effect (R) measured from reentry to the surface, as illustrated in Figure 3.

The percentages at each particular altitude for the V-γ points are averaged to give one value at every altitude, regardless of trajectory. The set of these averages are the wind weighting factors. Density weighting factors are computed in a similar way. These data are generated by NSWCDD and provided to FNMOC as part of the BALPAR formulation.[2]

There are different weighting factors for the TRIDENT I and TRIDENT II systems because the values are dependent upon missile performance characteristics. This results in different effects at each altitude. Both TRIDENT systems have two ballistic wind values (an East-West ballistic wind and a North-South ballistic wind). The TRIDENT I system has one ballistic density value (density departure from the Standard density data) based on range effects, whereas the TRIDENT II system has two ballistic densities based on range and velocity effects.[3] This additional ballistic density was required in order to meet the more stringent system accuracy goals. For TRIDENT II, density is regarded as a function of altitude, with the two ballistic density values being points on a line, as opposed to the constant altitude-independent ballistic density used for TRIDENT I. Although these systems differ in their application of ballistic density, the basic methodology is the same.

When missile performance data are refined, the reentry simulation model is updated accordingly. These changes can affect the weighting factor values. Whenever new missile definition and performance data are released, the weighting factors are recomputed by NSWCDD. If the new values are significantly different, then NSWCDD provides them to FNMOC in order to generate the most accurate forecast BALPARs possible. Additionally, NSWCDD must update the onboard climatology BALPAR data if new weighting factors are adopted.

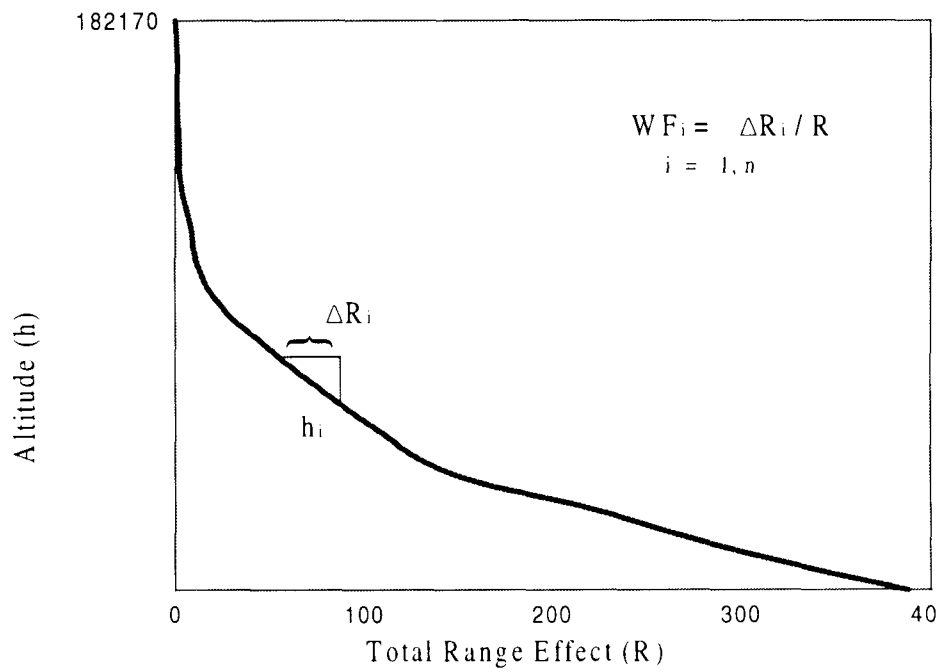

Figure 3—Generation of Weighting Factors

GENERATION OF BALPARS

The atmospheric data produced by FNMOC consist of wind and density values at various altitudes. Although heights are contained within the profile, the data are not collected by altitude, but rather by atmospheric pressure levels. Because air pressure varies from point to point, the corresponding altitudes may differ at each location. For example, an air pressure reading of 1000 mb may occur at an altitude of 250 ft for Point A, and at 400 ft for Point B.

In order to properly implement the weighting factor methodology, the profile data must have values at the weighting factor heights. The forecast profile data are converted to these heights by performing an interpolation of the data to the weighting factor altitudes. An example of this is shown in Figure 4. The interpolation is part of the BALPAR computation process at FNMOC as defined by NSWCDD. As mentioned earlier, NSWCDD provides FNMOC with a formulation containing the information (including weighting factors), guidance, and equations needed to convert the data from profiles to BALPARs.

Once the data are converted to the weighting factor altitudes, the BALPAR computations are performed. The winds at the weighting factor altitudes are given as:

$$EW_i, i = 1, n \quad where\ EW_i = f(h_i) \tag{1}$$

$$NS_i, i = 1, n \quad where\ NS_i = f(h_i) \tag{2}$$

where EW_i is the East-West wind component, NS_i is the North-South wind component, h_i is the weighting factor altitude, and n is the number of weighting factor altitudes.

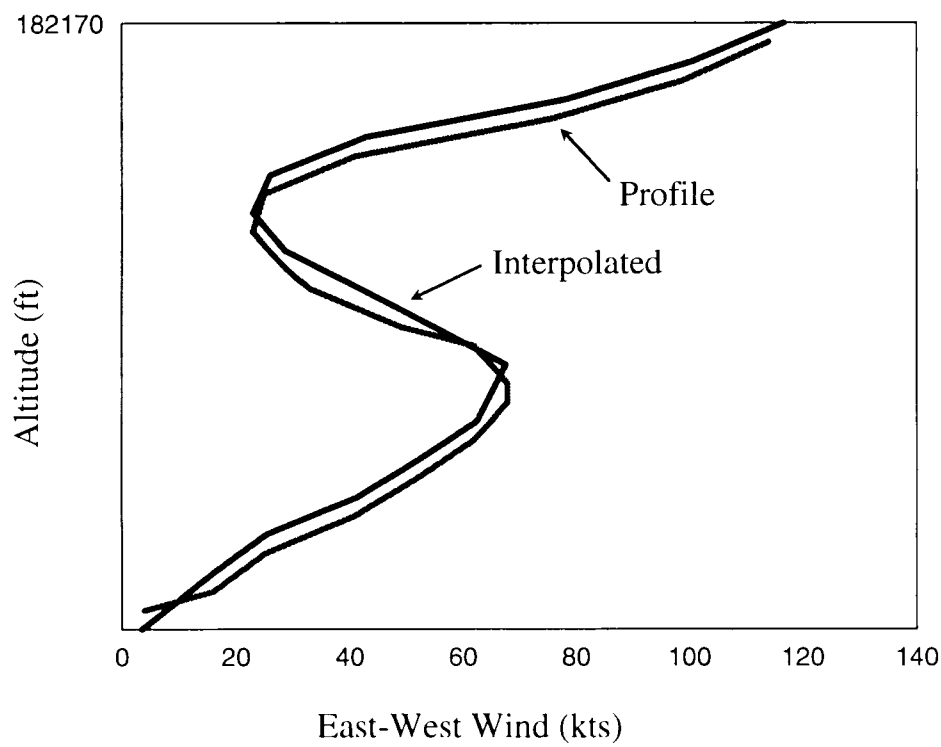

Figure 4—Interpolation of Profile Data to Weighting Factor Altitudes

The weighting factor altitude winds are then converted to BALPARs by summing the products of the wind data and the appropriate weighting factors. These computations are shown in Equations (3) and (4). BEW is the ballistic East-West wind, BNS is the ballistic North-South wind, and WFW_i are wind weighting factors for each weighting factor altitude.

$$BEW = \sum_{i=1}^{n} (WFW_i * EW_i) \qquad (3)$$

$$BNS = \sum_{i=1}^{n} (WFW_i * NS_i) \qquad (4)$$

Ballistic densities are computed in a similar manner. The density values at the weighting factor altitudes are given as

$$\rho_i, i = 1, n \qquad where\ \rho_i = f(h_i) \qquad (5)$$

where ρ_i is the density value interpolated to the weighting factor height, h_i are the weighting factor altitudes, and n is the number of weighting factor altitudes.

The first step in computing ballistic density values is to determine the density departure, KD_i. This is achieved by deriving the percentage of difference between the density at each weighting factor height ρ_i and the corresponding Standard Atmosphere density ρ_{STD_i}. Equation (6) shows this process.

$$KD_i = \left(\frac{\rho_i - \rho_{STD_i}}{\rho_{STD_i}} \right) * 100, i = 1, n \qquad (6)$$

Since the Standard Atmosphere data contains mean density values, a density departure from this mean is used to compensate for the effects of air density.

As mentioned previously, the TRIDENT I system has only one ballistic density value $\Delta\rho$. This value is produced by the following:

$$\Delta\rho = \sum_{i=1}^{n} (WFKD_i * KD_i) \qquad (7)$$

where $WFKD_i$ are the density weighting factors, and n is the number of weighting factor altitudes.

The TRIDENT II system has two ballistic density values. To find these data, the straight line used to produce density departure values from reentry to the surface must be generated. KD_0 is the 0-ft intercept of this line, and KD′ is the slope of the line. These values are produced by

$$KD_0 = \frac{\left(\sum_{i=1}^{n} WF\rho V_i h_i\right)\left(\sum_{i=1}^{n} WF\rho R_i KD_i\right) - \left(\sum_{i=1}^{n} WF\rho R_i h_i\right)\left(\sum_{i=1}^{n} WF\rho V_i KD_i\right)}{\left(\sum_{i=1}^{n} WF\rho R_i \sum_{i=1}^{n} WF\rho V_i h_i\right) - \left(\sum_{i=1}^{n} WF\rho V_i \sum_{i=1}^{n} WF\rho R_i h_i\right)} \qquad (8)$$

$$KD' = \frac{\left(\sum_{i=1}^{n} WF\rho R_i\right)\left(\sum_{i=1}^{n} WF\rho V_i KD_i\right) - \left(\sum_{i=1}^{n} WF\rho V_i\right)\left(\sum_{i=1}^{n} WF\rho R_i KD_i\right)}{\left(\sum_{i=1}^{n} WF\rho R_i \sum_{i=1}^{n} WF\rho V_i h_i\right) - \left(\sum_{i=1}^{n} WF\rho V_i \sum_{i=1}^{n} WF\rho R_i h_i\right)} \qquad (9)$$

where $WfpV_i$ are the density weighting factors associated with velocity, $WfpR_i$ are the density weighting factors associated with range, n is the number of weighting factor altitudes, and h_i are the weighting factor heights.

Once KD_0 and KD' are determined, the two ballistic densities $\Delta\rho_1$ and $\Delta\rho_2$ can be derived.

$$\Delta\rho_1 = KD_0 \tag{10}$$

$$\Delta\rho_2 = KD_0 + (KD' * 50{,}000) \tag{11}$$

$\Delta\rho_1$ is the ballistic density at 0 ft, and $\Delta\rho_2$ is the ballistic density at an altitude of 50,000 ft.

Figure 5 illustrates the BALPAR generated for a given profile. A comparison of the effects on the RB due to profile and BALPAR data is shown in Figure 6.

METHOD IMPROVEMENT

The BALPAR methodology described above has been utilized by TRIDENT systems from their beginnings. Efforts to improve this methodology or develop new techniques for compensating for environmental conditions are currently being investigated.

As stated earlier, the weighting factors at the specified heights are averaged over the extent of the V-γ map. Some trajectories are affected by the environmental conditions more than others. Adding more of these points to the weighting factor analysis, or giving these points more than an average share in the weighting factor computation, may help to reduce the error for these trajectories. Although this approach may

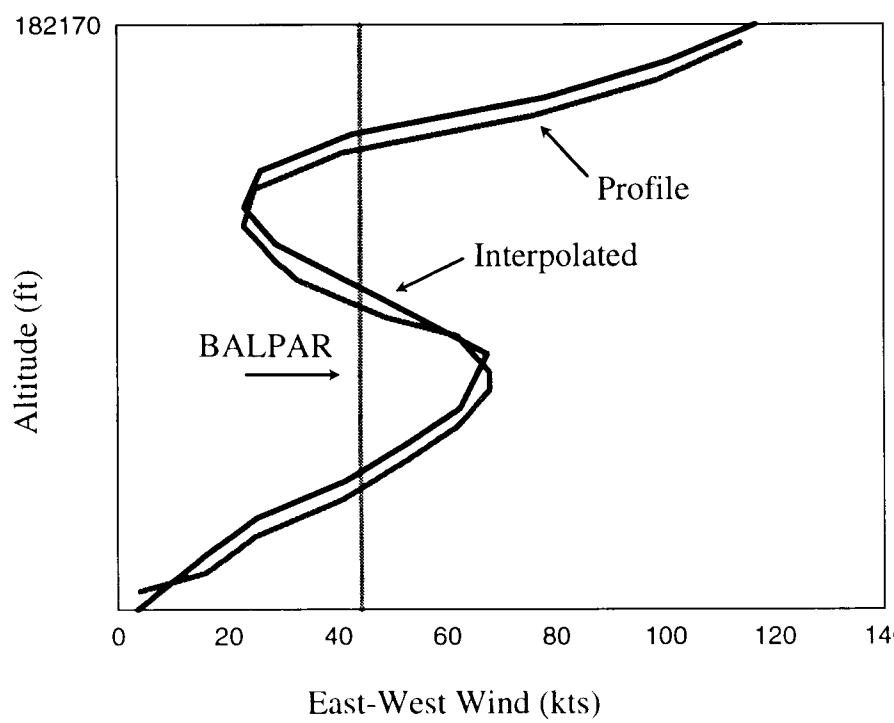

Figure 5—BALPAR Computed from Profile

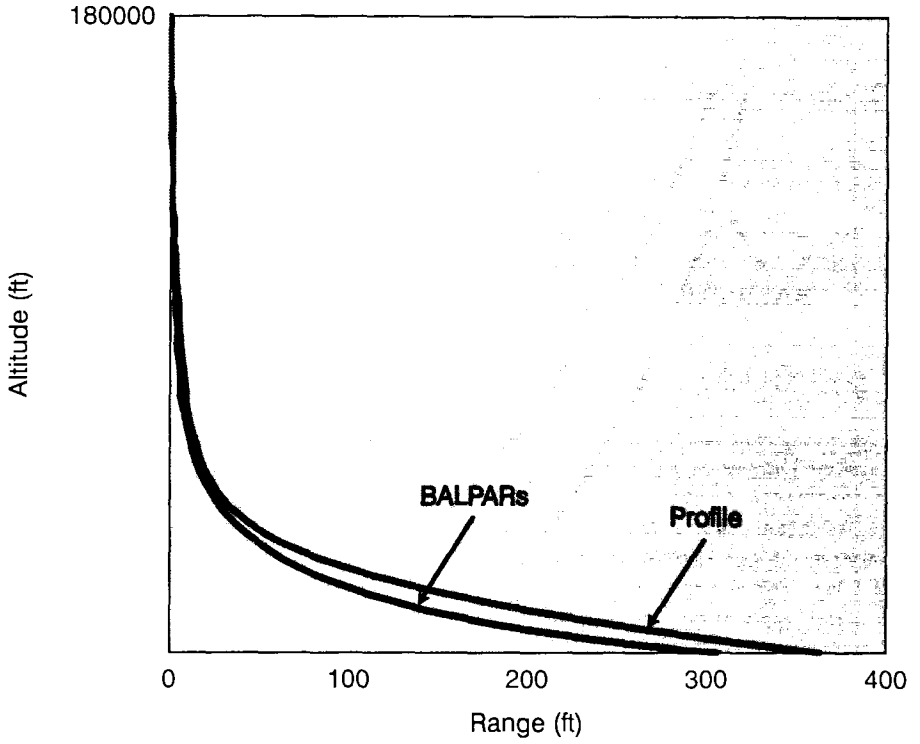

Figure 6—Weather Effects on Range for BALPAR and Profile Data

allow the error for these points to decrease, the method is unacceptable if it increases the error incurred at other points on the V-γ map.

The BALPAR process is designed so that the path of the RB using BALPARs may differ from the path produced by utilizing profile data. This results in different range distances at each altitude throughout the trajectory. However, at 0-ft altitude, this distance should be minimized. For targets at altitudes higher than 0 ft, some range errors will occur due to the difference in the trajectory path. As shown in Figure 7, a miss distance of ΔR is encountered for a target at altitude H. A possible solution to this problem would be to produce altitude-dependent BALPARs. This would complicate the BALPAR generation process because different sets of weighting factors would have to be developed for each target height. NSWCDD would need to provide these new sets of weighting factors, the associated altitudes, and guidance for implementation to FNMOC for use in producing the BALPAR messages. Because specific target altitude data are unknown to FNMOC, the best way to accomplish this task would be to produce these altitude-dependent data using grid-point altitudes. Because of the changing contours of the earth and the distance between grid points, it is not clear whether this approach would actually reduce the miss distance attributable to weather data.

The previous paragraphs described ways of reducing the error incurred by using BALPAR data. This error occurs because the set of profile data needed to cover the target data base is too large to send to the SSBNs. If the profile data could be reduced significantly and accurately while fulfilling message requirements and broadcast limits, the need to use BALPAR data for any reason would be eliminated. To pursue this possibility, data compression techniques are currently being investigated. Should a compression method prove feasible, the SSBN onboard computations could be performed

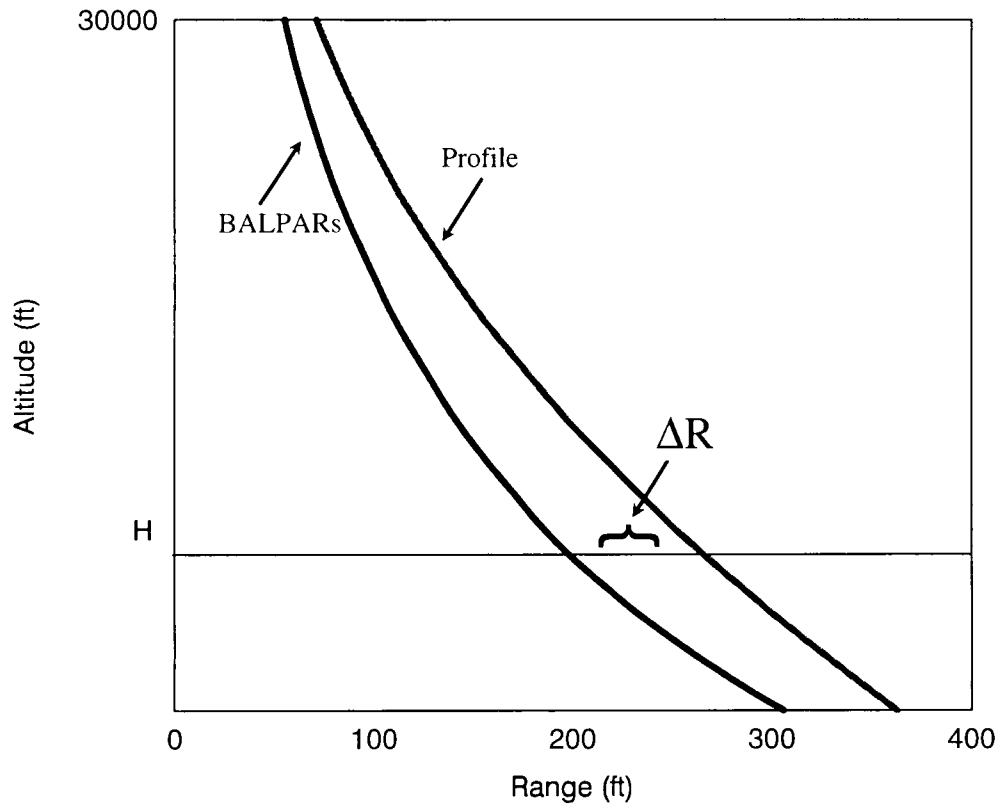

Figure 7—Miss Due to Target Elevation

using the raw profile data, not BALPAR approximations. This approach would obviously eliminate the BALPAR error and would thereby provide the most accurate method possible for the compensation of weather effects.

ACKNOWLEDGMENT

The development of the BALPAR methodology was performed by members of the Environmental Studies Group. As stated previously, BALPARs have been utilized for quite some time. The references made in this article refer to the most recent description of these processes.

REFERENCES

1. Meyerhoff, B., *TRIDENT II (D5) (Mk4) Operational Weighting Factors*, NSWCDD, Dahlgren, VA, 12 May 1989.

2. Wright, K., *NSWCDD Formulation and Guidelines for Ballistic Parameters (BALPARS)*, NSWCDD, Dahlgren, VA, 1 Dec 1994.

3. Hanks, Z., *Methodology to Produce Representative Ballistic Density For Use in the D5/Mk4 TD Function*, NSWCDD, Dahlgren, VA, 29 Jun 1987.

THE AUTHOR

MS. KIMBERLY A. WRIGHT

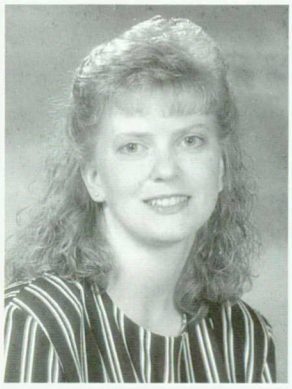

MS. KIMBERLY A. WRIGHT graduated from the Pennsylvania State University in May 1989 with a B.S. degree in mathematics. In 1990, she began her career at NSWCDD within the SLBM Systems and Environment Analysis Branch of the Strategic and Space Systems Department. Since that time, she has completed numerous weather data and performance studies. She was an active participant in the development of the SLBM Retargeting System (SRS) program by defining weather data requirements and characteristics. Her accomplishments also include authoring the SRS formulations used for atmospheric weather data support by the United States and the United Kingdom, serving as a liaison with the FNMOC, and participating in an SRS orientation briefing at the Trident Training Facility in Bangor, Washington.

Advanced Technology Demonstration of the Naval Tactical Missile System (NATACMS)

Mr. Richard A. Frazer and Mr. John E. Bibel

The Naval Surface Warfare Center conducted an Advanced Technology Demonstration (ATD) to demonstrate the effectiveness of the Army Tactical Missile System (TACMS) in the shipboard, at-sea environment. The ATD was planned and conducted in accordance with guidance and direction from OPNAV, Code N8. Specific requirements were to fire an Army TACMS missile from an Army M270 Launcher aboard an amphibious ship with no changes to missile or launcher unless necessary to accommodate the missile launch. The successful firing of the "Naval" Tactical Missile System (NATACMS) missile from USS Mount Vernon *on 12 February 1995 set the standard by which Naval Surface Fire Support (NSFS) and Surface Strike systems will be measured—in terms of range, payload, and accuracy.*

Introduction

During FY 91 and FY 92 deliberations, the Senate Armed Services Committee noted serious deficiencies in the ability of the Navy to provide fire support for U.S. expeditionary forces. Retirement of the battleships had severely reduced the capability to project power ashore during amphibious operations. The Navy was strongly encouraged to adapt the Army's Multiple Launch Rocket System (MLRS) family of munitions, which includes Army TACMS, to provide over-the-horizon firepower. TACMS was first deployed during Operation Desert Storm with great success. Thirty-two missiles were fired, destroying all targets, and there were no field failures.

OPNAV Code N8 directed that an Army TACMS missile be fired at-sea from an M270 launcher, with minimal modifications to accommodate a ship-based launch. A Navy ATD of this NATACMS was conducted during 1994 and 1995. This ATD leveraged developments from a simultaneous Army Joint Precision Strike Demonstration (JPSD) Program, in which Block I TACMS missiles were modified by reducing the payload and integrating Global Positioning System (GPS) technology into the navigation system to provide accurate, long-range, surface-to-surface, deep-strike capability. The NATACMS ATD consisted of launcher and missile design and development modifications to allow for shipboard launch, ground-based and

sea-based subsystem testing, and ground-based and at-sea missile firings. This article presents a summary of the NATACMS ATD.

WEAPON SYSTEM DESCRIPTION

NATACMS was a modified version of the Army TACMS, which consists of Army MLRS launchers and TACMS missiles. The TACMS launch vehicle is the M270 Armored Vehicle Mounted Rocket Launcher, a derivative of the Bradley Fighting Vehicle. The launcher carries the M269 Launcher Loader Module (LLM), the rocket and missile launcher module mounted on the rear of the M270, and the supporting Fire-Control System (FCS). The LLM contains all the equipment necessary to load, aim, and fire MLRS rockets and/or TACMS missiles, which may be fired over the cab or at bearings up to plus or minus 120 degrees.

The TACMS Block I missile is a surface-to-surface, inertially-guided, deep-strike missile, with a range of 150 kilometers. Loral Vought Systems (now Lockheed Martin Vought) is the prime contractor. The missile comprises four major sections: guidance, payload, rocket motor, and control sections. The guidance section houses the Missile Guidance Set (MGS) and the inertial measurement unit; and performs inertial navigation, guidance, autopilot, and warhead event functions. The payload section carries approximately 950 M74 antipersonnel-antimateriel (APAM) submunitions, which are released by splitting the warhead airframe skin open with explosive charges after the missile spins-up to four hertz. The rocket motor section contains solid rocket propellent, a nozzle, and an ignitor arm/fire assembly. The aft section of the missile is the control section, which consists of the four aerodynamic control surfaces, fin actuator assemblies, and the Control Section Electronics Unit.

New variants of the Army TACMS include the Block IA and Block II missile systems. TACMS Block IA, prototype tested during the JPSD program, is currently in Engineering Manufacturing and Development (EMD) and carries approximately 300 M74 APAM submunitions to 300-kilometers range. It is able to maintain lethality against the required target set through improved navigation, utilizing GPS aiding and updating of the inertial guidance system to account for misalignment and drift over the longer flight path. The Block II TACMS, scheduled to begin flight tests in FY 1998, will carry the Brilliant Antitank (BAT) submunition.

For the Navy ATD, the ATACMS could not be used without modification. Due to the dynamic ship motion environment, it was necessary to develop a weapon control system that could accurately find its position on the ocean surface, align the missile navigation and guidance system, and fire the missile. Also, because the NATACMS ATD was performed in conjunction with the Army JPSD program, missile upgrades, such as the addition of GPS-aided navigation, were made.

The launcher for the NATACMS ATD was a modified M270 launcher, equipped with a Launcher Reference Package (LRP), a Precision Lightweight GPS Receiver (PLGR), and Navy-unique FCS modifications. In addition, the LLM for the NATACMS ATD required a unique cable set to allow the missile Navigation and Guidance Computer (NGC) to communicate with the LRP and the PLGR, and a KYK-13 cryptographic fill device. The launcher for the NATACMS ATD is shown in Figure 1 with some of the new or modified components.

The major change required to the M270 Launcher in order to provide an at-sea missile launch capability was replacement of the Stabilization Reference Package (SRP) with the LRP inertial measurement unit. The LRP provided attitude, angular rate, and velocity for the transfer of alignment to the missile navigation and guidance systems. The LRP unit, provided by Allied Signal, comprised a triad of ring-laser gyros and accelerometers, a Trimble TANS II commercial coarse/acquisition (C/A)

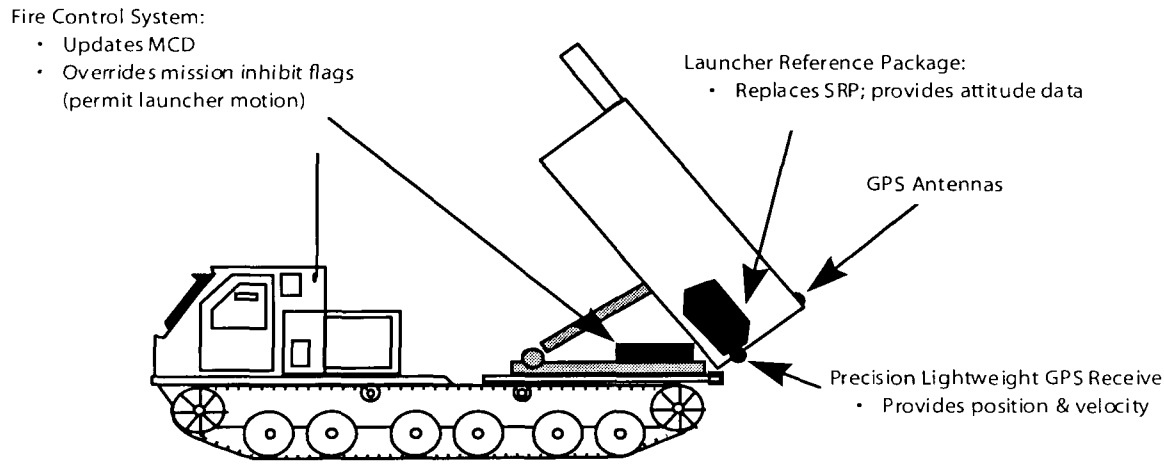

Figure 1—M270 Armored Vehicle Rocket Launcher

code GPS receiver, and supporting electronics. The LRP required 80 minutes of initialization and gyrocompass time, and transitioned from gyrocompass to free inertial mode at Launcher Lay (T-10 minutes in the countdown sequence). After gyrocompassing, the LRP accuracy was guaranteed for 30 minutes in the free inertial mode.

A Rockwell PLGR (precision lightweight GPS receiver) was also added to the launcher to provide more accurate position and velocity, and the GPS almanac and ephemeris data to the missile GPS-aided navigation system. Crypto-variable Weekly keys were loaded into the PLGR and the missile embedded GPS receiver (EGR) by a KYK-13 electronic transfer device.

The NATACMS FCS was little changed from the system used to fire Army TACMS missiles. The FCS controlled the operational functions and events of the missile and launcher up to launch. Modifications were made to incorporate the operation of the LRP and PLGR for the transfer of alignment. The known fixed target location was input by the program module as the Mission Critical Data (MCD).

Changes to the missile were incorporated to allow for the addition of onboard GPS capability. The Navigation Guidance Module (NGM) housing the GPS receiver was added to the aft-end of the warhead section, and two GPS antennas were added to the airframe skin. To make room for the NGM and antennas, the number of submunitions was reduced from 950 to 727. The MGS guidance, navigation, and inertial sensor assembly computer programs were modified to exchange the proper data with the computer in the NGM for transfer of alignment and GPS-aiding. Figure 2 shows the missile and the NATACMS modifications.

The NGM contained the NGC, the EGR, and the power distribution unit. A Rockwell Collins GEM-I P/Y code GPS receiver was utilized as the EGR to provide for accurate navigation aiding. The NGC interfaced with the LRP, MGS, PLGR, and the KYK-13 during prelaunch in order to transfer alignment, exchange data, and initialize the EGR. In flight, the NGC accepted time-tagged position data from MGS and EGR, and passed the data through a navigation Kalman filter to provide position, velocity, and attitude error corrections to the MGS to improve navigation accuracy. The NGC

hardware was common to JPSD and NATACMS, but the NGC software was Navy-unique because it controlled guidance system initialization and the transfer of alignment.

The operation of the GPS/Inertial Navigation System (INS) system during flight is summarized as follows. At 30 seconds after launch, the EGR began to acquire Global Positioning System satellites. After four satellites were acquired, GPS-aided navigation began. Pseudorange and range-rate measurements were computed once every second and passed to the GPS/INS navigation filter in the NGC, where the GPS measurements were combined with the inertial instrument measurements to form error signals. An 11-state Kalman filter estimated the navigation errors, which were used for corrections to the navigation solution. Starting at apogee, the navigation corrections were sent to the MGS for aiding the inertial navigation solution every 10 seconds.

PREFLIGHT SUBSYSTEM TESTING

Prior to ATD flight testing, ground tests were successfully conducted at Loral Vought Systems in Grand Prairie, Texas, to evaluate Navy-unique hardware and software. These were hardware-in-the-loop (HWIL), closed-loop, and open-loop tests; vibration tests; antenna performance tests; integration tests; LRP tilt-table tests; transfer alignment tests; stationary mock-fire tests; and moving launcher tests. The moving launcher road tests demonstrated that ATD software could support successful fire missions in a motion environment.

NATACMS gyrocompass tests were conducted aboard USS *Mount Vernon* on a not-to-interfere basis during 17 to 19 January 1995. These tests evaluated LRP performance in the ship motion environment and the quality of the transfer of alignment from LRP through the

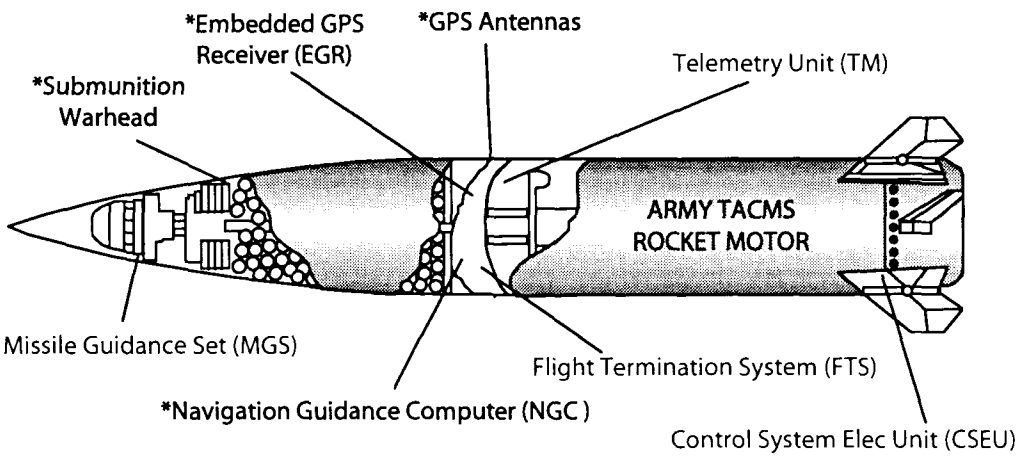

*Modified for ATD/JPSD

Figure 2—The NATACMS Missile

NGC to the MGS in a NATACMS "Iron Bird" missile mockup. Many successful mock fire missions were executed, demonstrating that the LRP functioned well in the ship motion environment, and that accurate transfer of alignment was possible at sea.

FLIGHT TEST RESULTS

Prior to the Navy ATD flight tests, the Army fired three modified Army TACMS missiles at the White Sands Missile Range (WSMR), New Mexico, for the JPSD program. The JPSD flight tests were of interest to the Navy, in that these missiles used the same NGMs with Embedded GPS Receivers and NGCs as NATACMS. Therefore, the expected missile terminal accuracy was similar to NATACMS. The final two tests proved the effectiveness of GPS-aided inertial navigation and also demonstrated that TACMS can fly to long ranges very accurately without GPS-aiding, given a precise alignment transfer between the SRP and the Inertial Measurement Movement (IMU).

Two flight tests were conducted for the NATACMS ATD. The first was a land-based flight at WSMR, and the second was fired at-sea from USS *Mount Vernon*. Postflight analyses were performed for both flight tests at NSWCDD using the NATACMS version of the Tactical Army System Simulation (TASS) six degree-of-freedom (6-DOF) simulation. The postflight reconstruction 6-DOF model was run with inputs derived from the actual test conditions, such as time of day, initial missile location, and measured winds. Both deterministic (no missile system errors) and stochastic performance were examined. For the latter, a set of 50 Monte Carlo runs were utilized to estimate the statistical properties of probable flights. Comparisons of the simulated and flight test telemetry and Best Estimated Trajectory (BET) data were examined at several important points during flight. GPS system and end-game accuracy performance were also examined.

The results from the first flight test indicated some anomalies that prevented the missile from hitting the targeted point. In addition, several relatively insignificant deviations from the expected nominal trajectory were also found. Due to the nature of the technology demonstration (i.e., short, fast-paced time schedule and quick-fix modifications to existing hardware and software to make them work versus optimally engineering new hardware and software), some of the deviations were never fully reproduced. However, the causes of the primary anomalies were identified and corrected, and the success of the second flight test demonstrated that all major problems had been adequately addressed and solved.

The first flight of the NATACMS ATD (ATD-1) was conducted on 11 January 1995, at WSMR. The test was designed to mimic hardware, software, and procedures of the at-sea flight demonstration, so as to reduce technical, operational, and safety risk. The missile was launched at approximately 1330 MST, and the duration of the flight was approximately 190 seconds.

Missile flight kinematic performance was near nominal for the majority of the ATD-1 flight. (Nominal performance is defined as the actual missile flight parameters within +/- 1 standard deviation of postflight reconstructed values.) Figure 3 shows the comparison between the nominal (postflight) and "actual" vertical plane trajectories. Both the BET and missile telemetry data are shown, and are considered as "actual". The missile velocity and flight-path angle comparisons are shown in Figures 4 and 5. All of these kinematic comparisons show a good postflight reconstruction, with the three sources of data virtually overlaying each other. These figures also illustrate that the test flight was near nominal kinematically. Some deviations from the expected postflight nominal trajectory were found. In particular, there was a position error early in flight (due to incorrect position initialization) and a crossrange position difference (approximately 75 m from nominal) at apogee. This was probably due to

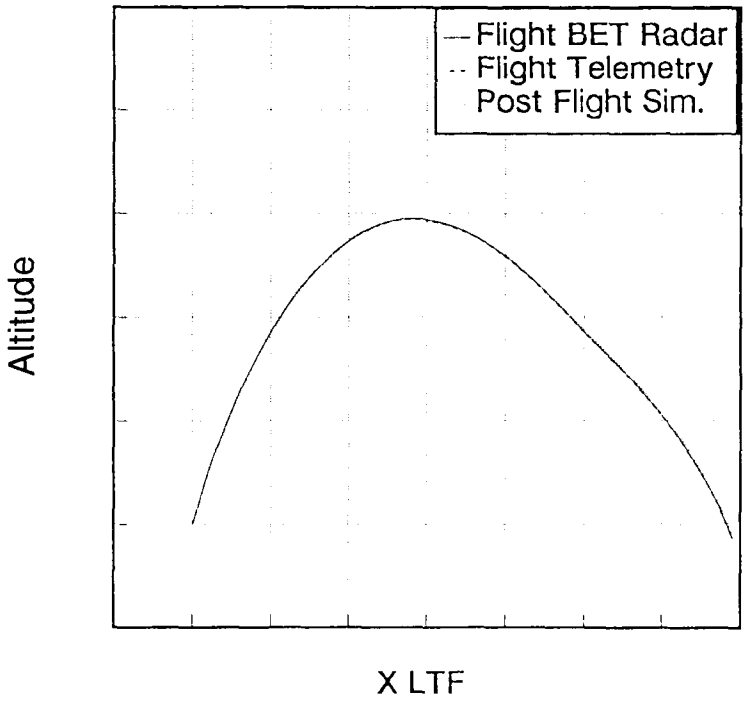

Figure 3—ATD-1 Vertical Plane Postflight Comparison

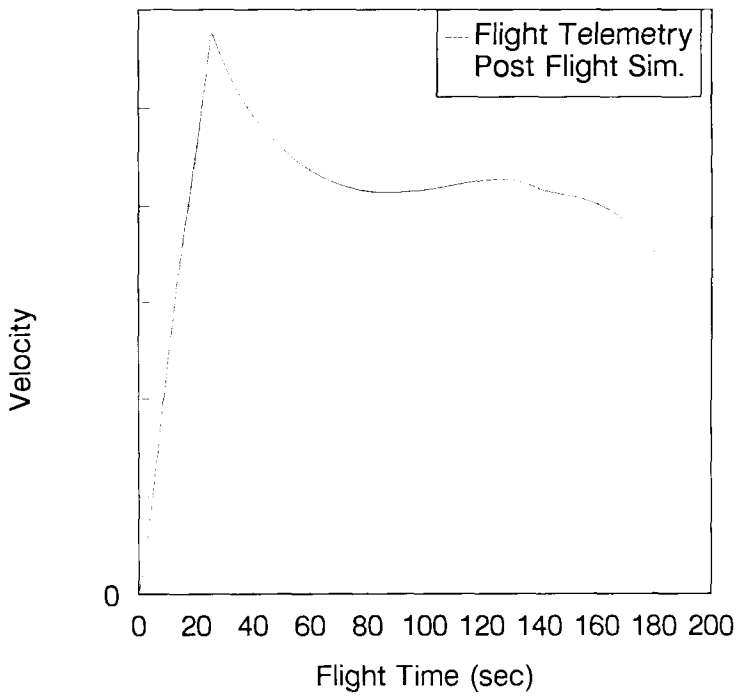

Figure 4—ATD-1 Velocity Postflight Comparison

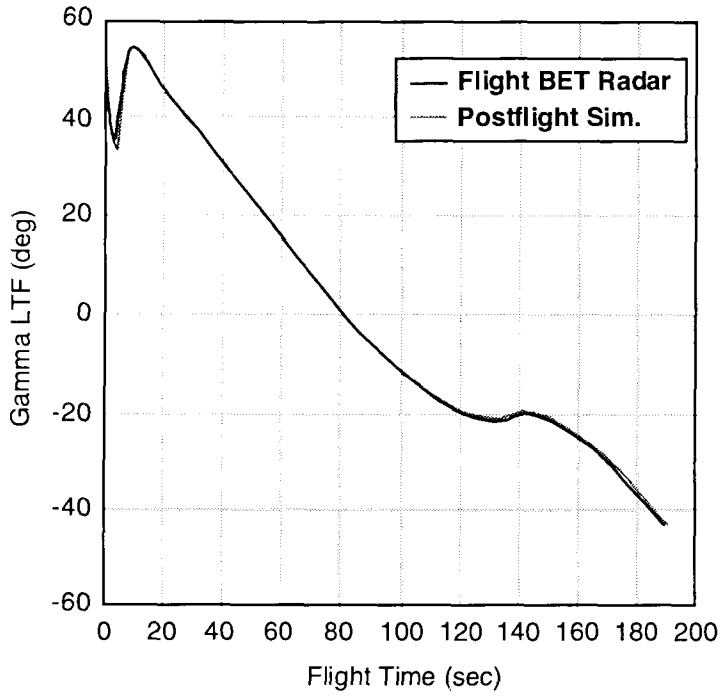

Figure 5—ATD-1 Flight-Path Angle Comparison

either a heading misalignment inaccuracy, gyro drift, or different wind conditions than provided and used in the postflight simulation.

The GPS-aided inertial navigation system was beneficial on this flight test, although it was not as effective as planned. At 30 seconds into the flight, the EGR went into navigation mode, in which the five GPS receiver channels attempt to acquire the GPS satellites necessary for navigation. By 62 seconds, four satellites were acquired and in STATE 5 track, a carrier track mode that yields the full accuracy on the pseudorange and range-rate measurements. A lower STATE track number would indicate either a search/acquisition mode or partial track mode. However, the acquisition time was greater than the requirement specification. The initial satellites tracked were Satellite Vehicle (SV) numbers 18, 22, 28, and 29. From t = 69 seconds and for the remainder of the flight, SV numbers 14, 18, 22, and 29 were tracked by the EGR. Following the satellite acquisition at 62 seconds, the GPS/INS filter ran for approximately 17 seconds prior to apogee, allowing for filter transients to settle and obtain steady-state estimates of the errors. This is shown by the filter position error estimates given in Figure 6. At apogee, approximately 80 seconds into the flight, the first correction was sent to the MGS. Only two navigation corrections were incorporated on this flight, due to a lockup of the Input/Output (I/O) message traffic between the MGS and NGC. Figure 7 shows the navigation position corrections that were utilized (only the position error estimates and corrections are shown here for the sake of brevity). Note that the first correction is relatively larger than the second correction—indicating that the missile navigation systems had corrected for the prior navigation error. Since only the first two corrections were made on the flight, the remainder of the flight was essentially flown under inertial navigation only.

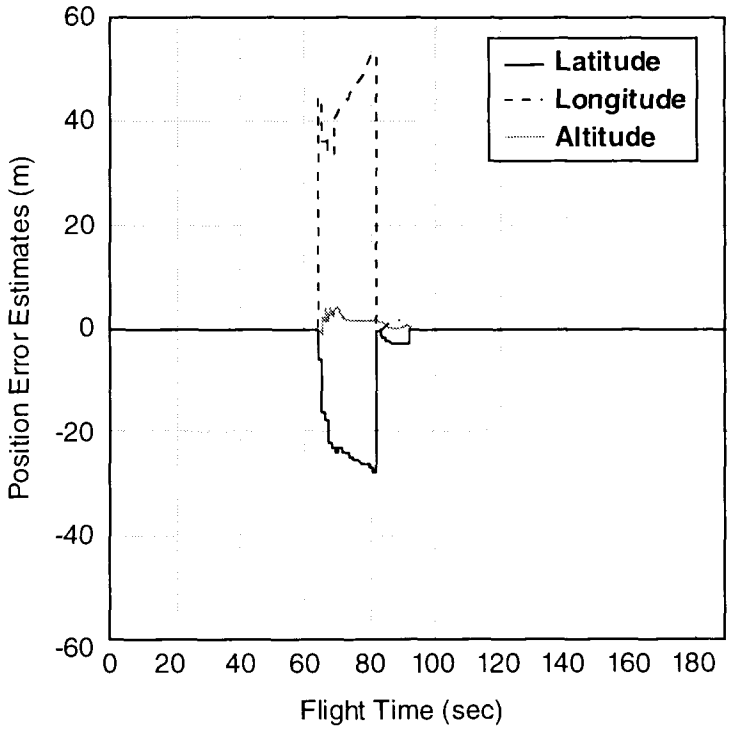

Figure 6—ATD-1 GPS/INS Filter Position Error Estimates

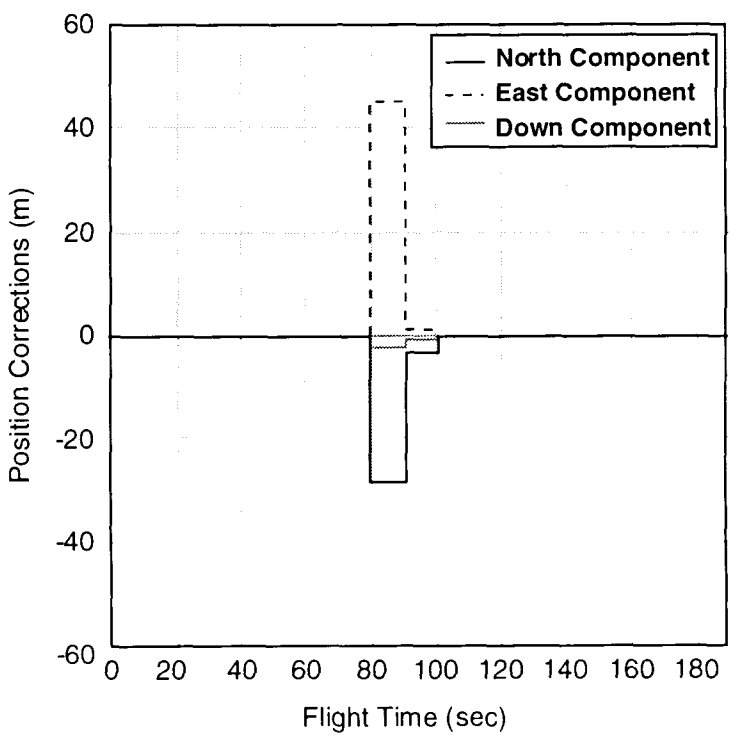

Figure 7—ATD-1 Navigation Position Corrections

Examination of the parameters at end-game (good guidance, spin up, and warhead event) revealed a major anomaly that affected the payload delivery accuracy. The onboard guidance system calculated burst point coordinates that were in error over 100 m in range and 400 m in altitude from their expected values. Further postflight analysis proved the error to be a sine/cosine (of the range angle to the target) swap in the MCD due to a programming error. Thus, the missile was, in essence, guiding to an incorrect target point. The end result was that the missile delivered its submunitions to the wrong spot, with a total radial miss of approximately a factor of two of the ATACMS Block I Circular Error Probable (CEP) performance specification for that range.

However, in guiding to what the missile thought was the correct burst point, the missile's guidance and navigation was accurate enough to yield a horizontal radial miss (relative to the desired burst point) of approximately one-third of the CEP performance requirement. In terms of the classified JPSD Spherical Error Probable (SEP) dispense specification, the total radial miss at the warhead event was about 1.5 times the SEP requirement. This result can be understood realizing:

1. that the missile did incorporate two navigation corrections near apogee

2. thus, the missile had approximately 20 seconds during the time of those corrections to correct the previous drift and misalignment errors that had accrued

3. that the remainder of the flight was essentially inertially guided.

Prior to the second ATD flight test, the anomalies that were found from ATD-1 (primarily software errors) were corrected. Preliminary flight readiness checks were performed with two live NATACMS missiles aboard USS *Mount Vernon* on 4 February 1995, resulting in two successful simulated missile firings. Successful flight readiness checks were also conducted early on 11 and 12 February 1995 aboard USS *Mount Vernon*.

The second ATD flight demonstration occurred at the Pacific test range operated by the Naval Air Weapons Center, Weapons Division (NAWC/WPNS), Point Mugu, California. USS *Mount Vernon* attempted to launch ATD-2 on 11 February 1995. However, a misfire condition was caused by a launcher indication of a weapon malfunction at half a second prior to launch after ignition of the telemetry thermal battery, but before ignition of the rocket motor. Since the primary missile was no longer able to transmit telemetry, a one-day delay was necessary in order to transfer the backup NATACMS missile to the active launcher cell. The next day, 12 February 1995, at approximately 1501 PST, the missile was successfully launched from the M270 off the flight deck of USS *Mount Vernon*, LSD-39. A photograph of the launch is displayed in Figure 8. The missile was targeted in the revetment area on San Clemente Island. Missile telemetry was relayed from an airborne P3 aircraft to a receiver on San Nicolas Island and from there transmitted to Pt. Mugu. The missile BET was obtained from FPS-16 tracking radar located on San Nicolas Island.

Comparison of the flight test telemetry and BET data to the postflight simulation values revealed that the flight was near nominal. Figures 9 through 11 show the comparisons for the vertical trajectory, the velocity, and the flight-path angles. The results in these plots show good agreement between the flight test and simulation data. The slight deviations are insignificant, and all data lie within one standard deviation of the nominal. The guidance parameter flight data also compared well to the postflight simulation data.

During the ATD-2 flight test, the GPS/INS system worked well. At 30 seconds, the EGR began to try to acquire satellites, and between 49 and 50 seconds, four satellites were locked in

STATE 5 track. In this flight test, channel 5 acquired STATE 5 track rather than channel 4. The channel 4 hardware appeared to have difficulties, so the channel 5 hardware was used to track the fourth satellite. Channel 5 and channel 4 software slots were swapped after 78 seconds. This demonstrated the benefit of having an onboard GPS receiver with an extra (fifth) channel for satellite tracking. The satellite identification numbers tracked were SV numbers 2, 7, 16, and 27. These satellites were tracked until 209 seconds, when it appears that channel 2 lost STATE 5 track of SV number 7. At 211 seconds, channel 2 went into reacquisition mode (STATE 7) and found SV number 31, but could not lock into STATE 5 track. Thus, from 209 seconds to the end of the flight (approximately 217 seconds), measurements from only three satellites were providing navigation updates to the NGC.

Figure 8—ATD-2 NATACMS Missile Launch

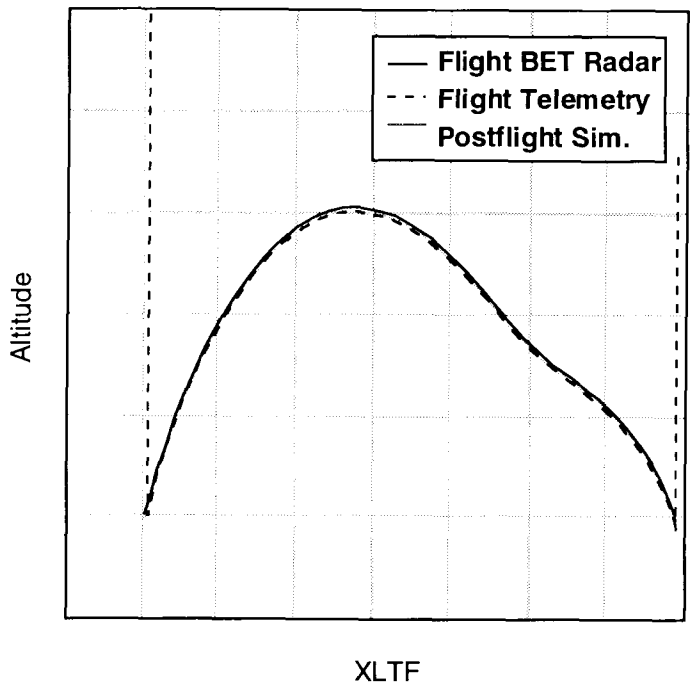

Figure 9—ATD-2 Vertical Trajectory Comparison

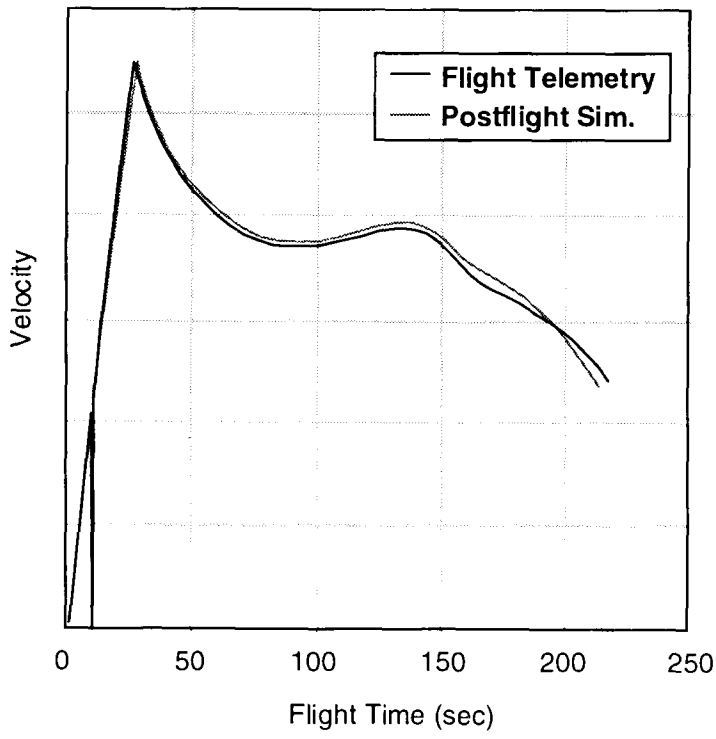

Figure 10—ATD-2 Velocity Comparison

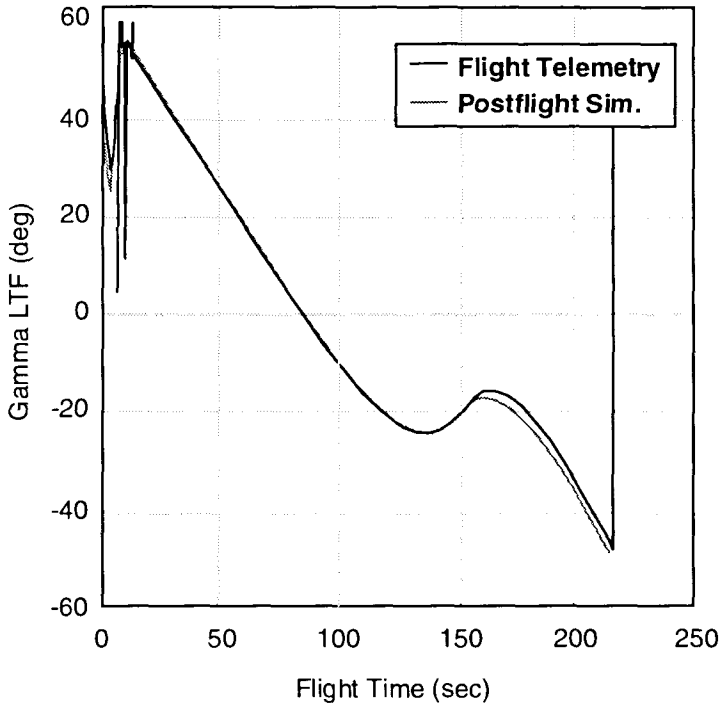

Figure 11—ATD-2 Flight-Path Angle Comparison

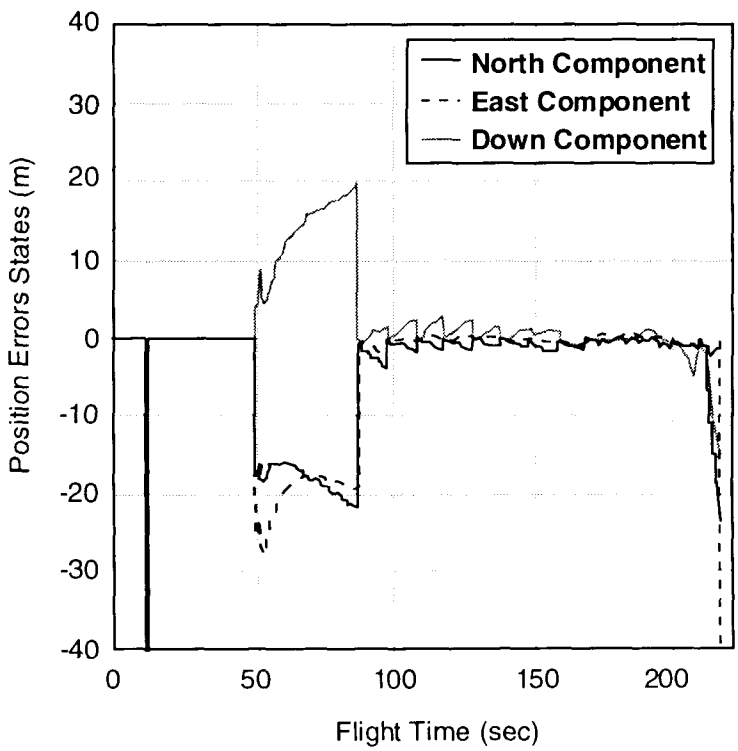

Figure 12—ATD-2 Nav Filter Position Error Estimates

The GPS/INS filter worked as designed. Figures 12 and 13 show the position-error-state estimates and the navigation corrections. The navigation filter begins at approximately 50 seconds, settles transients for about 30 seconds, and begins to provide navigation corrections to the MGS at apogee. The first correction was incorporated at 85 seconds, and subsequent corrections were incorporated every 10 seconds. As expected, the first correction is relatively larger than the subsequent corrections, approximately 20 m in the three directions. A total of 14 corrections were utilized. At the end of the flight, another relatively large correction was made. This resulted because the EGR lost one of its four satellites, and the Kalman filter had to propagate forward a solution based on three sets of satellite measurements. Thus, the accuracy of the estimates and the corrections was somewhat degraded. However, because this occurred near the end of the flight, its impact on the guidance accuracy was insignificant.

The accuracy at the end-game was well within the performance specifications. The GPS/INS navigation allowed for accurate guidance to the burst point. The horizontal radial miss at the desired burst point (based on quick-look radar data) was less than 75 percent of the ATACMS Block IA SEP requirement, and the payload delivery accuracy (as determined by the bomblet impact pattern found around the target site) was less than 20 percent of the ATACMS Block I CEP specification. The "small" bomblet pattern was of nominal size and distribution, and "on-target" as indicated by Figure 14. Thus, the results of this flight test demonstrate that the ATD was successful.

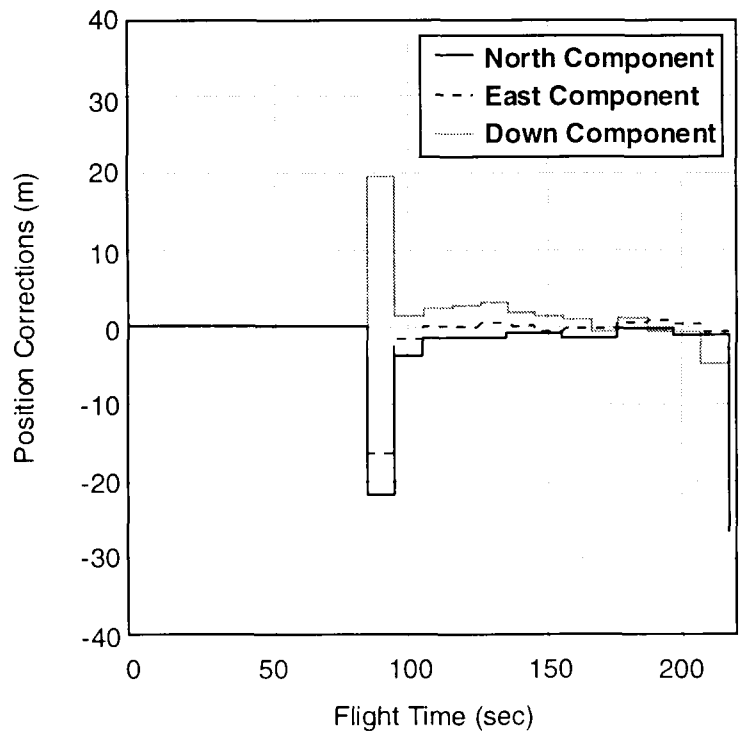

Figure 13—ATD-2 Navigation Position Corrections

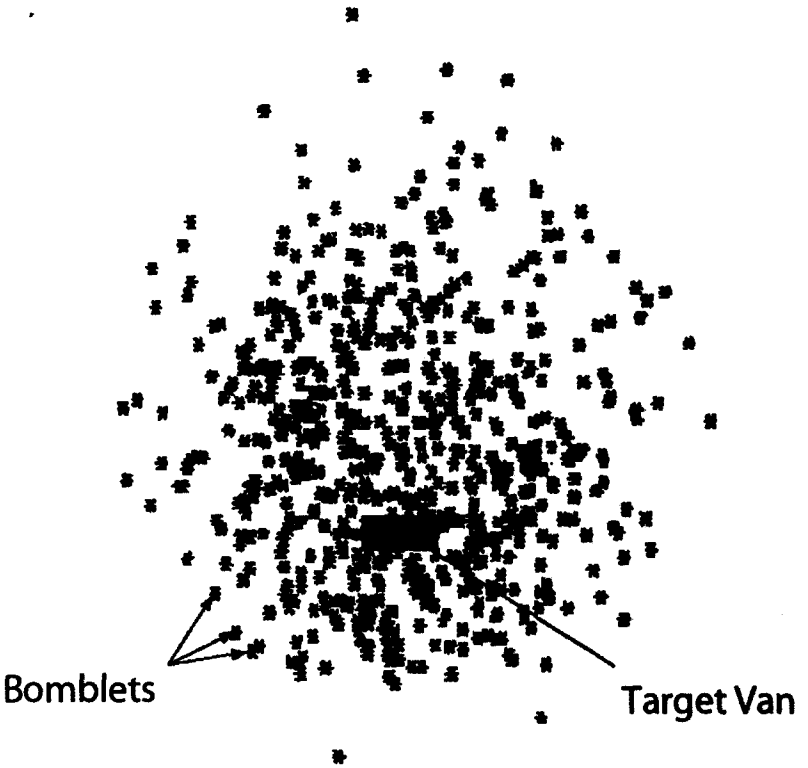

Figure 14—ATD-2 M74 Measured Bomblet Pattern

LESSONS LEARNED AND CONCLUSIONS

Several lessons were learned during this ATD that would prove valuable to any flight demonstration program. The establishment and utilization of relevant test procedures for ground-based and at-sea tests reduce the risk of error and test failure. Video and voice recording of test events on the flight deck and in the launch control van and real-time display at the pertinent control centers during the test helps to document the test events precisely and provide data should problems arise. Land-based flight testing prior to at-sea flight tests is highly recommended. For this ATD, the land test at WSMR was essential to the success of the at-sea test. Testing at land-based ranges provides a controlled test environment where performance can be carefully tested, measured, and documented for postflight analysis. Results can be used to correct deficiencies or fine-tune designs. Land-based testing also provides the opportunity to test and evaluate safety and test procedures prior to the up-tempo pace of shipboard operations and testing.

Successful launch of the NATACMS missile from USS *Mount Vernon*'s flight deck has proven that a modified Army TACMS missile can be fired effectively at sea. The Army TACMS missile was a very good performer. Missile guidance, autopilot, rocket motor, and the fire control worked together to place a huge payload on target. The success of this NATACMS ATD sets the standard by which NSFS and surface strike systems will be measured—in terms of range, payload, and accuracy. Target range was consistent with requirements for NSFS, and the payload was substantial enough to deal with a large spectrum of targets. It is concluded that

NATACMS can be launched from a ship with extreme accuracy at long standoff range. Thus, the TACMS can be a valuable weapon in the Navy inventory for NSFS and also for pre-invasion strike applications.

ACKNOWLEDGMENT

Acknowledgment is given to Mr. Mark S. Jones for his assistance in the preparation of the postflight analysis results.

GLOSSARY

6-DOF	Six Degree-of-Freedom
APAM	Antipersonnel - Antimateriel
ATD	Advanced Technology Demonstration
BAT	Brilliant Antitank
BET	Best Estimated Trajectory
C/A	Coarse/Acquisition
CEP	Circular Error Probable
EGR	Embedded GPS Receiver
EMD	Engineering Manufacturing and Development
FCS	Fire-Control System
GPS	Global Positioning System
HWIL	Hardware in the Loop
I/O	Input/Output
IMU	Inertial Measurement Unit
INS	Inertial Navigation System
JPSD	Joint Precision Strike Demonstration
LLM	Launcher Loader Module
LRP	Launcher Reference Package
MCD	Mission Critical Data
MGS	Missile Guidance Set
MLRS	Multiple Launch Rocket System
NATACMS	Naval Tactical Missile System
NAWC/WPNS	Naval Air Weapons Center, Weapons Division
NGC	Navigation and Guidance Computer
NGM	Navigation Guidance Module
NSFS	Naval Surface Fire Support
PLGR	Precision Lightweight GPS Receiver
SEP	Spherical Error Probable
SRP	Stabilization Reference Package
SV	Satellite Vehicle
TACMS	Tactical Missile System
TASS	Tactical Army System Simulation
WSMR	White Sands Missile Range

THE AUTHORS

MR. RICHARD A. FRAZER

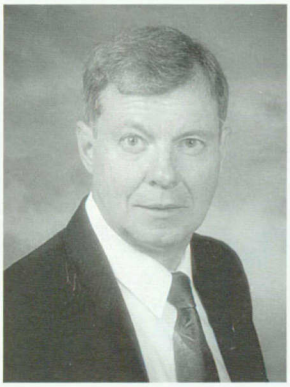

MR. RICHARD A. FRAZER is an electronics engineer in the System Engineering Branch of the Missile Systems Division. He was System Engineer for the NATACMS ATD and was the Navy Test Team Leader aboard USS *Mount Vernon* during missile system testing. In 30 years at the Naval Surface Warfare Center, Dahlgren Division (NSWCDD), he has been involved with weapon control systems, AEGIS, SMARTROC, FLIR/LASER for SEA, electro-optical systems, antisubmarine warfare, laser tracking and ranging, ship electrical systems, high-impact shock, chemical agent detection, and solid-state circuit breakers. Mr. Frazer also served as NSWCDD's NSAP Program Manager and Director of the NSWCDD Fleet Interaction Office. He holds a B.S. in electrical engineering from Duke University.

MR. JOHN E. BIBEL

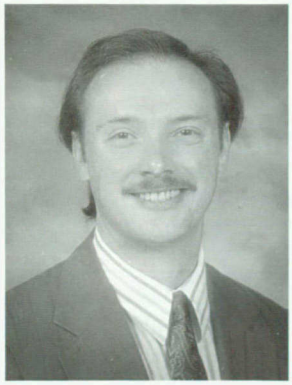

MR. JOHN E. BIBEL received a B.S. degree in aerospace engineering from the Pennsylvania State University in May 1984. Since then, he has been employed at NSWCDD, where he has worked in the areas of simulation, performance analysis, guidance, navigation, control, estimation and flight testing for tactical missile systems. Over the past couple of years, Mr. Bibel was the lead aeromechanics engineer for the NATACMS ATD, was co-chair of the marinized-ERINT concept definition team for Phase I of the Navy TBMD COEA, and has supported the AEGIS, ESSM, and SLWT programs. Mr. Bibel is currently working on completing his Master's thesis to complete requirements towards an M.S. degree in aerospace engineering from Virginia Polytechnic Institute and State University, and is a senior member of the American Institute of Aeronautics and Astronautics.

SM-2

TACMS

Tomahawk

Vertical Launching System

Strike
WARFARE WEAPONS SYSTEMS

STRATEGIC & STRIKE

SS

WARFARE WEAPONS SYSTEMS

DEPARTMENT OF THE NAVY

UNITED STATES OF AMERICA